DAMAGE DETECTION IN CONCRETE UNDER IMPACT LOAD AT VARYING TEMPERATURES USING PIEZOSENSORS

Ph.D. THESIS

by

INDRAJEET SINGH

DEPARTMENT OF CIVIL ENGINEERING
DELHI TECHNOLOGICAL UNIVERSITY
DELHI – 110042 (INDIA)
JANUARY, 2024

DAMAGE DETECTION IN CONCRETE UNDER IMPACT LOAD AT VARYING TEMPERATURES USING PIEZOSENSORS

A THESIS

Submitted in partial fulfilment of the

requirements for the award of the degree

of

DOCTOR OF PHILOSOPHY

in

CIVIL ENGINEERING

by

INDRAJEET SINGH
(En. No. 2K18/PHD/CE/14)

Under the supervision of

PROF. NIRENDRA DEV

&

DR. SHILPA PAL

DEPARTMENT OF CIVIL ENGINEERING
DELHI TECHNOLOGICAL UNIVERSITY
DELHI – 110042 (INDIA)
JANUARY, 2024

DELHI TECHNOLOGICAL UNIVERSITY
DELHI

CANDIDATE'S DECLARATION

I hereby certify that the work which is being presented in the thesis entitled **"DAMAGE DETECTION IN CONCRETE UNDER IMPACT LOAD AT VARYING TEMPERTURES USING PIEZOSENSORS"** in partial fulfilment of the requirements for the award of the Degree of Doctor of Philosophy and submitted in the Department of Civil Engineering of the Delhi Technological University, Delhi is an authentic record of my own work carried out during a period from August, 2018 to January, 2024 under the supervision of Prof. Nirendra Dev, Professor, and Dr. Shipa Pal, Associate Professor, Department of Civil Engineering, Delhi Technological University, Delhi, India.

The matter presented in this thesis has not been submitted by me for the award of any other degree or in any other Institution.

(**Indrajeet Singh)**

This is to certify that the above statement made by the candidate is correct to the best of my knowledge.

(Dr. Shilpa Pal)
Joint Supervisor

(Prof. Nirendra Dev)
Supervisor

Date: 02 January, 2024

Dedicated to my loving sister

LT. Ms. Vandana Singh

ACKNOWLEDGEMENTS

I would like to thank the people who have been most helpful to me during my research work. First and foremost, I am at a loss of words, to do justice to thank the quantum of support offered by my supervisor ***Prof. Nirendra Dev*** *throughout. Be it the critical guidance on work or the encouragement to stay strong and motivated to execute all kinds of tasks required to complete the work, he has been my strongest anchor. A heartfelt thanks to him for giving me the immense freedom to design my work plan and for always being around to help, provide feedback and valuable mentoring. Thanks to the professor for being a kind fatherly figure to me. I am deeply grateful to my research Joint supervisor****, Dr. Shilpa Pal*** *for her nonstop guidance, enduring patience, and nurturing support throughout this research, without which successful completion would not have been possible. It has been an honor to be associated with such a great supervisor and learn from her experience.*

I would like to express my sincere gratitude and appreciation to Head of the Department's Prof. V.K minocha, the Head of the civil engineering, for their unwavering support, guidance, and mentorship throughout the research process. Their expertise and commitment have been invaluable in shaping the direction of this work. I am deeply thankful for their encouragement and for fostering an environment of excellence within our department.

I extend my sincere thanks to the heads and faculty members especially Prof. A.K. Shrivastava, Prof. Anbu Kumar, Prof. Munendra Kumar, Prof. A.K Sahu and Prof Raju Sarkar for providing me sensible guidance, faultless planning, helpful advice, and kind cooperation at various stages of my PhD journey.

Special gratitude goes to the members of the SRC, Prof. Amjad Masood from the Department of Civil Engineering at Aligarh Muslim University, Aligarh, and Prof. H.K Sharma from the Department of Civil Engineering at NIT Kurukshetra, Kurukshetra. I am also thankful to Dr. Ritu Raj and Dr. N. Jayanthi from Delhi Technological University for their insightful and constructive feedback.

I owe a great debt of gratitude to Professor ***S. K. Bhalla*** *for the consistent direction and support he has provided for my research work. I thank* ***Dr. Talakula Visalakshi*** *for all the head-start she gave me in networking and pitching my work at various places and forums. I want to express my gratitude to* ***Dr. Tushar Bansal*** *for their kind assistance from the bottom of my heart and for providing the much-required assistance in all of the activities that are necessary for the completion of my research work.*

I am immensely grateful to the staff at the Earthquake Engineering Laboratory, Concrete Engineering Laboratory and Computer-Aided Design Laboratory within the Department of Civil Engineering. I extend my sincere thanks to lab technician Mr. Shashikant and lab assistants, Mr. Atul, Mr. Sanjay, Mr. Rakesh, and Mr. Mahesh for their unwavering support during the experimental and simulation phases of my research.

Thanks, ***Dr. Manvendra Varma*** *and* ***Dr. Rahul Meena*** *for all the uncountable waves of laughter at our tea sessions. I would like to give a huge token of gratitude to* ***Mr. Abhishek Prakash Paswan*** *for being the best brainstorming partner. I would always remember the time spent with you during the discussions on science and technology. Your capability of visualizing the working of the solution of any problem with the "jugad" helped me to understand my work better.*

I would like to extend my appreciation to Mr. Prateek Roshan, whose unwavering support from my PhD days to the submission of my thesis played a pivotal role in my success

I am grateful to my senior and colleagues, Harshit Jayant, Dr. Ibadur Rehman, Dr. Anju Agarawal and Dr. Parvesh Kumar, Dr. Nisha Soni, Istuti Singh, Prashant Ramteke, Uzma Wani, Rahul Kumar, Dr. Sushant Kumar, Dr. Deepak Singh, Arti Raha, Dr. Suresh Kumar Nagar, Mr. Nitin Lamba, Mr. Rajat Gautam *for providing me with critical comments and suggestions and all those who interacted and exchanged ideas with me in completing the research Special thanks are also due for Dr. Shailendra Yadav to his insightful advice.*

I am indebted to my juniors, Mr. Aniket Sharma, Mr. Wesam Al Agha, Vijay Kaushik, Mr. Rishabh Tyagi, Mr. Aditya Apurva and Ms. Arya sajith, Ms. Janhvi singh, Mr. Ashish kumar, for their constant support

My deepest thanks go to my beloved parents, Shri Dharm Raj Singh and Smt. Vidya Devi, for their blessings and unwavering support. I extend my appreciation to my wife, Mrs Chandani Patel and, my grandfather Shri Pannalal, my father-in-law Mr. Parasnath Singh and my mother-in-law Meera Devi for their moral and emotional support, Special thanks are reserved for my friends Mr. Ankit Pandey, Mr. Annand Garg, Mr. Himanshu Kandpal, Mr. Manmohan Singh, Mr. Manish Jain, Mr. Ankit Kumar Pandey, Mr. Santosh, Mr. Girish Yadav and my childhood friends, Mr. Abhinav Pal, Mr. Vidhan, who stood by me throughout this journey.

(Indrajeet Singh)

ABSTRACT

Concrete structures subjected to impact loading exhibit a rapid and severe deterioration, leading to substantial losses in both property and human lives. As temperatures rise, the destructive effects of impact loading intensify. To mitigate such damages and losses, the implementation of Structural Health Monitoring (SHM) in concrete structures becomes imperative. Concrete structures need structural health monitoring (SHM) to avoid these damage and loss. Electromechanical impedance (EMI) technique has emerged as a promising SHM technique for monitoring concrete damage. This study monitors the health of the concrete using EMI under different impact loading at varying temperature conditions. For this purpose, an experiment study has been performed on concrete cube specimens in which different piezo configurations (surface bonded, non-bonded, and jacketed) were installed to acquire the raw signature (conductance and susceptance). The initial phase of the experiment involved subjecting a concrete cube to distinct impact and temperature conditions. In the impact-loading aspect, two drop heights, 3 meters and 3.5 meters, were considered. In the temperature-loading effect, three temperature levels of 50 °C, 100 °C, and 150 °C has been examined. Additionally, the study delved into the combined effects of both impact and temperature. In this combined scenario, the concrete specimen was preheated to temperatures of 50 °C, 100 °C, and 150 °C before being subjected to an impact load. The impact was induced by releasing a free-falling iron ball from two different heights, 3 m and 3.5 m, onto the specimen's top surface. To detect damage in concrete, the initial step involved acquiring the baseline conductance signature, which represents the healthy state of the material, from the sensors. Subsequently, this baseline signature was compared with the signature obtained from the damaged state. For a more comprehensive assessment of concrete damage, the raw signature data has been further analyzed using numerical techniques such as RMSD (Root Mean Square Deviation) and MAPD (Mean Absolute Percentage Deviation). In addition, PZT-based equivalent structural parameters, including stiffness, mass, and damping, were extracted from the raw signature data. This extraction allowed for the identification of changes in the mechanical properties of the specimens, enhancing the understanding of various damage conditions in concrete cubes.

In addition to assessing the current damage condition, the study included a crucial element, estimating the remaining life of the structure. This estimation has been made possible through the utilization of equivalent-based parameters. These parameters were employed to gain a more comprehensive understanding of the extent of damage and predict how much longer the structure could be expected to serve its intended purpose. This valuable insight aids in making informed decisions regarding maintenance, repair, or replacement to ensure the continued safety and functionality of the structure. Furthermore, temperature compensation techniques were explored to mitigate a limited number of false alarms related to damage conditions arising from the PZT heightened temperature sensitivity.

Further the study has been also conducted on the structural members, specifically beams, which were subjected to the combined influence of 3 m impact and three different temperature condition of 50 ^{o}C, 100 ^{o}C and 150 ^{o}C. For better assessment of concrete damage in beam the structural parameter has been also calculated same as the concrete cube. Moreover, the research broadened to encompass boundary conditions, where the concrete cube's performance was evaluated under a fixed boundary condition. In this setup, the concrete cube underwent testing with a 3 m impact height at three distinct temperature levels of 50 °C, 100 °C, and 150 °C for jacketed sensors.

To validate the experimental findings, finite element analysis has been conducted, aligning the empirical results with analytical outcomes. The experimental results revealed that jacketed sensors proved to be more effective in health assessments for both boundary conditions. On the basis of statistical tools such as RMSD and MAPD value, both are the reliable tools for calculating the incipient and progressive damage in concrete under the effect of impact loading at varying temperature. The extracted equivalent stiffness with increasing impact number clearly indicates damage propagation in concrete sample for different sensor configuration. The stiffness loss increases with the rise in temperature from ambient to 150°C, ranging from 6.87 % for NBPS sensors to 10.42 % for JKTPS sensors. This data illustrates that the stiffness loss escalates by approximately 3 to 4% with the increase in temperature and also showed satisfactory agreement between the experimental and equivalent plot of x and y.

The extracted equivalent stiffness with increasing impact number followed a distinct decreasing pattern (stiffness loss up to 15%) that clearly indicates damage propagation in concrete beam and also showed satisfactory agreement between the experimental and equivalent plot of x and y. Notably, in terms of strain values, the analytical results closely aligned with the experimental data.

TABLE OF CONTENTS

LIST OF FIGURES

LIST OF TABLES

LIST OF ABBREVIATIONS

CVS	Concrete vibration sensors
EMI	Electromechanical Impedance Technique
ESPs	Equivalent stiffness Parameters
FFBC	Free-Free Boundary Conditions
FBC	Fixed Boundary Conditions
FEM	Finite Element analysis
JKTPS	Jacketed piezo sensors
LCR	Inductance Capacitance and Resistance
MAPD	Mean Absolute Percentage Deviation
NBPS	Non Bonded Piezo Sensors
OPC	Ordinary Portland cement
PCE	Polycarboxylic Ester
PZT	Piezoelectric-ceramic
RMSD	Root mean square deviation
SBPS	Surface bonded Piezo sensors
SHM	Structural Health Monitoring
SAs	Smart aggregates

LIST OF SYMBOLS

D_3	Electric Displacement
S_1	Strain value in direction
d_{31}	Piezoelectric strain coefficient
E_3	External electric field
T_1	Axial stress in direction
$Y^{\bar{E}}$	Complex young’s modulus of elasticity of the PZT patch
$\varepsilon_{33}^{\bar{T}}$	Complex electric permittivity
E_s	Young's modulus
μ	Poisson's ratio
V	Voltage generated across the PZT
V_p	Absolute peak voltage
S_p	Strain values at the vicinity of PZT
δ	Dielectric loss tangent
h	Thickness of PZT
ɳ	Mechanical loss factor

Chapter 1: INTRODUCTION

1.1 Research Background

In recent years, structures have become more vulnerable to severe dynamic events such as terrorist attacks, blast waves, earthquakes, industrial accidents, etc. These occurrences, linked to high loading rates, are frequently followed by fire outbreaks and spread, exposing structures to harsh conditions.

Understanding the behaviour of the structural material used is essential for reducing the effects of such events. However, there is still much discussion in the field of civil engineering over how reinforced concrete structures react to thermal exposure and consequent dynamic loading. There is a wealth of research on both thermal degradation and the effects of temperature on concrete structural components, as well as concrete subjected to high strain loading rates at room temperature. Research on the combined impact of thermal and dynamic loads on concrete structures, however, is severely lacking.

Very few studies have demonstrated the damage monitoring of concrete under the action of an impact load at different temperatures. The majority of the literature only shows the monitoring of damage in concrete when impact and temperature are applied separately. The researcher did not explore numerous domains in order to ascertain the extent of damage resulting from the combined action of impact and temperature. Further research is necessary to advance the field of Structural Health Monitoring (SHM) specifically in the context of concrete structures subjected to combined loading conditions involving impact and temperature.

Structural Health Monitoring (SHM) entails continuously measuring the loading environment and assessing the structure or its components for significant responses. SHM necessitates periodic inspections of the structure utilizing sensors to collect data. The collected sensor data is then analyzed to establish the structure's current state. Smart materials serve an important function as sensors in structure monitoring. These materials react to changes in factors such as stress, magnetic field, heat, and electric field, among others. Smart sensors identify damage that might otherwise go unnoticed by the human eye. In this research, the Electromechanical Impedance (EMI) approach with piezoelectric sensors have been used for the identification of the damage in concrete.

The EMI technique has been used in several applications, including concrete hydration monitoring explained by Shin and Oh (2009), Tawie and Lee (2010) , Negi et al. (2018) and

Zuo et al. (2013), Fatigue damage monitoring explained by Haq et al. (2020), and damage detection in RC structures under embedding and surface-bonded conditions explained by (2011), Liu et al. (2017) and Jothi Saravanan and Singh Chauhan (2022a). The electromechanical impedance (EMI) approach, with its high sensitivity, fast response time, low cost, simple installation, and intelligent real-time detection, has become more and more preferred choice as a suitable non-destructive technology for SHM.

1.2 Type of Damage in Concrete

Concrete can suffer from various types of damage over time due to factors such as environmental conditions, loading, construction defects, or material properties. Here are different types of damage that can occur in concrete structures:

1.2.1 Cracking

Shrinkage Cracks: These occur due to the natural shrinkage of concrete as it cures, leading to small, often hairline cracks.

Structural Cracks: These are caused by overloading or foundation settlement and can significantly affect the integrity of the structure.

Temperature-Related Cracks: Concrete can crack due to temperature fluctuations, especially in regions with extreme weather conditions.

1.2.2 Corrosion

Rebar Corrosion: When the steel reinforcement (rebar) inside concrete corrodes due to exposure to moisture and oxygen, it can lead to the expansion of the steel and cracking of the concrete cover.

Sulfate Attack- Sulfates in the environment can react with concrete components, leading to expansion and cracking.

Chloride Attack- Chloride ions, often from de-icing salts, can penetrate concrete and initiate corrosion of embedded reinforcement.

1.2.3 Abrasion

Surface Abrasion- Heavy traffic, equipment, or abrasive materials can erode the surface of concrete, reducing its thickness and strength over time.

Abrasion from Aggressive Chemicals- Exposure to chemicals like acids or alkalis can cause surface deterioration and reduce concrete's durability.

1.2.4 Freeze-Thaw Damage

In regions with freeze-thaw cycles, moisture can penetrate concrete, freeze, and expand, leading to cracking and spalling.

1.2.5 Alkali-Silica Reaction (ASR)

This chemical reaction occurs when certain types of reactive aggregates in concrete combine with alkalis from cement, resulting in gel formation and expansion. ASR can cause significant cracking and damage.

1.2.6 Crazing

Crazing refers to the formation of a network of fine cracks on the surface of concrete, often due to improper finishing or curing practices.

1.2.7 Erosion and Wear

In hydraulic structures like dams and spillways, erosion by flowing water can gradually wear away the concrete surface.

1.2.8 Biological Damage

Microorganisms such as bacteria and fungi can thrive in moist environments and contribute to the deterioration of concrete through processes like biogenic sulfuric acid corrosion.

1.2.9 Impact Damage

Heavy impacts, such as those from vehicular collisions or falling objects, can cause localized damage, including cracking and spalling.

1.2.10 Fire Damage

High temperatures from fires can cause concrete to lose its structural integrity and undergo spalling or explosive spalling, leading to severe damage.

1.2.11 Structural Overloading

Excessive loads, whether temporary or sustained, can cause concrete to fail in compression, shear, or tension, leading to structural damage.

1.2.12 Poor Workmanship

Deficiencies in the construction process, such as inadequate compaction, improper curing, or insufficient reinforcement placement, can result in concrete damage and reduced strength.

Understanding the various types of damage to concrete is essential for designing durable structures, implementing preventive maintenance, and undertaking timely repairs to extend the lifespan of concrete elements.

1.3 Smart Materials and Structures

There is considerable variation in the definition of smart materials or structures among researchers. In the past, terms like 'intelligent,' 'adaptive,' and 'organic' were used to describe smart systems (Rogers 1988). However, a workshop organized by the US Army Research Office reached a consensus to adopt a single term: 'smart.' The term 'smart' was defined as follows: A system or material which has built-in or intrinsic sensor(s), actuator(s) and control mechanism(s) whereby it is capable of sensing a stimulus, responding to it in a predetermined manner and extent, in a short/ appropriate time, and reverting to its original state as soon as The concept of smart structures draws inspiration from nature, where living organisms possess a distributed system of sensory neurons throughout their bodies, allowing the brain to monitor the condition of different body parts. Smart structures consist of three essential components: sensors, actuators, and a control mechanism. Additionally, the fourth qualifying term recognized by Rogers (1988) is "timely response." The combination of these components allows for the formulation of a "smart system," which can be applied at both the macroscopic (structure) and microscopic (material) levels. Smart materials exhibit adaptive properties in response to external stimuli, such as loads or environmental factors, demonstrating inherent intelligence. During a workshop conducted by the US Army Research Office, Rogers (1988) provided a definition for smart materials, describing them as materials capable of altering their physical properties in a precise manner when subjected to particular stimuli. These stimuli encompass factors such as pressure, temperature, electric and magnetic fields, chemicals, or nuclear radiation. The changes in physical properties could affect attributes such as shape, stiffness, viscosity, or damping. Piezoceramic patches, sharp memory alloys, fiber-optic sensors, electro-rheological fluids, and electro-magnetic fluids are a few examples of smart materials that allow us to design stimulus-response systems with far higher resolution than any traditional NDE techniques. In recent years, Lead Zirconate Titanate ($PbZrTiO_3$) piezoceramic (PZT) materials have emerged as leading candidates for Structural Health Monitoring (SHM) applications. PZT patches harness the widely studied piezoelectric effect initially discovered by Pierre Curie and his brother in 1880. The fundamental mechanism of this effect can be explained as follows:

Piezoelectric effect occurs by the displacement of ions, causing the electric polarization of the crystal's structural units. When an electrical field is applied, the ions are displaced by *electrostatic forces, resulting in the mechanical deformation of the whole crystal (Encarta Concise Encyclopaedia, 2012).*

PZTs, being ceramics, can be manufactured in various shapes and sizes to accommodate specific application requirements. These materials possess both actuator and sensor capabilities due to the piezoelectric effect they exhibit. For instance, when subjected to strain, PZT materials generate a voltage that can be measured, allowing for strain detection. In embedded or surface-bonded systems, PZTs can serve as sensors to detect damage. Additionally, when an electric voltage is applied across their poling axis, piezo ceramics experience strain or displacement, making them suitable for actuator applications as well. PZT patches are highly suitable for applications in Structural Health Monitoring (SHM) and active control systems. Their ability to convert mechanical energy to electrical energy and vice versa makes them well-suited for use as structural dampers. In the context of the present study, the focus lies on piezoelectric materials and their common applications, including the Electromechanical Impedance (EMI) technique, shear lag effect, and challenges related to piezoelectric power and energy. These topics are particularly relevant and will be given special consideration in this research.

1.4 SHM Techniques

Aktan et al. (2000) defined the structural health monitoring (SHM) as the systematic collection, verification, and analysis of technical data to support decision-making processes throughout the life cycle management of a structure. It involves the establishment of a reliable system capable of detecting and interpreting unfavourable "changes" in a structure, whether caused by damage or normal operations (Kessler et al. 2002). The SHM system consists of various components, including sensors, actuators, amplifiers, and signal conditioners. The emergence of smart materials and systems has significantly contributed to advancements in SHM and Non-Destructive Evaluation (NDE). Smart materials, such as piezo ceramics, shape memory alloys, and fibre optics, have found extensive application in SHM, enabling enhanced monitoring capabilities. These materials play a vital role in the detection and assessment of structural health, enabling timely and accurate decision-making processes. SHM techniques broadly divided into two parts

a) Global techniques
b) Local Techniques

1.4.1 Global Techniques

The global SHM techniques can be further categorised as either dynamic or static. Global dynamic approaches encompass subjecting the test structure to low-frequency excitation, which can be either harmonic or impulsive in nature. Subsequently, the associated vibration responses (comprising displacement, velocity, and accelerations) at specific locations on the structure are measured. The collected vibration data is then analysed to determine the initial mode shapes and natural frequencies of the structure. When these findings are compared to data from a healthy condition, useful information about the location and severity of damage can be gained. However, because these procedures are global in nature, they may not be extremely sensitive to early damage.

1.4.2 Local Techniques

In contrast to the Global SHM techniques, a large number of Local SHM techniques can be chosen from in order to identify any damage that may have been caused to the structure. Some examples of the local techniques are ultrasonic techniques, acoustic emissions, eddy currents, impact echo testing, magnetic field analysis, and penetration dye testing.

1.5 Application of Piezo Sensors in Structural Health Monitoring

Accordig to Aktan et al. (2000) SHM is described as the measurement of a structure's critical responses to its operating and loading environment as well as any anomalies or deterioration or damage indications that may compromise its operability, serviceability, or safety reliability. According to another definition given by Kessler et al. (2002), SHM refers to a dependable system with the capacity to recognise and understand negative changes in the structure as a result of damage and regular operation.

In the broadest sense, SHM refers to the gathering, verification, and analysis of technical data to support life cycle management decisions. Table 1. 1 explains the distinctions between SHM, condition assessment, and non-destructive evaluation.

Sensors used for Structural Health Monitoring (SHM) can be broadly categorized into two main groups: (a) Conventional sensors and (b) Sensors based on smart materials. Commonly utilized sensors, such as electrical strain gauges, vibrating wire strain gauges, and accelerometers, fall under the category of conventional sensors. The ability of a material to alter its physical characteristics in response to a particular kind of sensory input is known as smart material qualities. Piezoelectric materials, shape memory alloys, and electro-rheological fluids are among the commercially accessible smart materials.

Table 1. 1 Difference between SHM, condition assessment and non-destructive evaluation (Bhalla et al., 2014).

Structural Health	**Condition Assessment**	**Non-Destructive Evaluation**
Ongoing monitoring	Intermittent one-time assessment to determine the present state of the structure.	The assessment of a material, component, or system's properties as required, without continuous monitoring, and without causing any damage.
To identify the emergence of irregularities in structural behaviour and performance	To assess the suitability of the structure for a specific use or purpose.	To identify particular defects. For instance, ultrasonic testing, magnetic-particle inspection, dye penetrant testing, radiography, eddy current testing, and similar methods
Comprehensive and wide-ranging in its scope.	A component of Structural Health Monitoring (SHM)	Non-Destructive Evaluation (NDE) can contribute to Structural Health Monitoring (SHM) and condition assessment

In addition to the global and local techniques, there are hybrid approaches that serve as an interface between the two. One of the most prevalent examples of such a hybrid technique is Electromechanical Impedance (EMI). EMI falls in between the global and local techniques. This method bears resemblance to global variation techniques but operates within a high-frequency range of 50 kHz to 500 kHz. Notably, its sensitivity rivals that of ultrasonic techniques, making it a powerful intermediary approach. In the EMI method, the electrical impedance signatures are initially obtained and then transformed into structural impedance data to enhance our comprehension of structural responses. Structural impedance is a fundamental concept within structural engineering, serving as a critical tool for evaluating how structures react to dynamic forces and waves. This concept plays a pivotal role in the design, analysis, and maintenance of diverse structures to guarantee their safety, stability, and optimal performance under varying load conditions.

1.6 Basics of Emi Technique

In the EMI technique, PZT patches are fixed to the surface of the structure. These patches interact with the host structure, generating a distinctive health signature that depends on the structural impedance. For acquiring the signature, they are subjected to high-frequency excitations of electric field using impedance analyzer or LCR meter. Owing of the direct and inverse piezoelectric effects, any change in the structure's mechanical impedance as a result of damage causes the PZT transducer that is attached to it to alter in terms of electrical admittance. The technique is popularly called as the EMI technique. Typically, the electro-mechanical admittance signature, which includes the conductance (real part) and susceptance (imaginary part), is obtained while the structure is in a healthy state and serves as the reference baseline for subsequent assessments of structural integrity. The EMI technique has demonstrated a remarkable sensitivity to early-stage damages. PZT patches can be readily affixed to hard-to-reach sections of structures and aircraft. They can be activated for monitoring as needed, without the need to take the structures out of service or perform any disassembly or reassembly of critical components. All these attributes unquestionably provide the EMI technique with an advantage over other conventional passive sensor systems. Since the patch is attached directly to the structure of interest, it has been shown that the mechanical impedance of the structure correlates with the electrical impedance of the patch. Feasibility studies for damage detection using the EMI technique have been effectively carried out on a diverse range of structures, including but not limited to simple beams, plates, bridge truss structures, airplane composites, pipeline structures, and reinforced concrete (RC) structures. These investigations have effectively recognized several damage mechanisms, including cracking, bolt loosening, composite delamination, and corrosion.

1.7 Scope of the Study

The scope of the study delineates the parameters and constraints defining the research's extent. It elucidates the precise objectives, research inquiries, and key areas of focus within the study. Based on the provided information, the study focuses on the application and evaluation of various techniques, methods, and setups for monitoring and evaluating concrete properties, structural health, and damage in different types of concrete structures.

Monitoring Methods: The study explores Electromechanical Impedance (EMI) techniques, PZT-based sensors and voltage relation technique for identifying the damage in the concrete structures.

Application: The study targets applications in various types of structures, such as concrete buildings and RC structures.

Objectives: The primary objective /of the study is to investigate the effectiveness and feasibility of the proposed monitoring setups and techniques in detecting concrete damage under the combined effect of impact and temperature loading conditions.

Numerical and Experimental Analysis: The study involves both numerical simulations (using finite element analysis) and experimental evaluations to validate the effectiveness of the proposed setups and techniques.

Overall, the scope of the study is to explore the practical approaches for monitoring concrete properties, structural health, and identify the damage in concrete cube and reinforced concrete beam under the impact load at varying temperatures using advanced monitoring electromechanical impedance techniques and setups. The research aims to provide valuable insights into, detecting structural damage and improving monitoring efficiency in various real-world scenarios.

1.8 Research Objective

The current study has the following objectives:

- Performance of the different sensor configurations such as surface bonded, embedded and non-bonded under impact load using PZT at varying temperature.
- Identification of damage and its location for structures under impact loading using piezo sensors at varying temperature.
- Validation of experimental results with numerical modelling.

By addressing these objectives, the current study seeks to enhance the understanding of damage detection in concrete structures and contribute valuable insights for future design, monitoring, and maintenance practices

1.9 Thesis Organization

- This thesis has been organized into six parts. Chapter 1 consist of introduction, research background, research objective and scope and the details discussion about the SHM.
- In Chapter 2, a summary of previous research on impact loading and temperature loading conditions, as well as the electromechanical impedance (EMI) technique and its applications in a variety of fields, is presented.
- Chapter 3 describes the fabrications of several piezo sensor configurations as well as the experimental examination on a concrete cube under impact and temperature loading circumstances.
- Chapter 4 extend the experimental work on the RCC beam under impact and temperatures loading conditions.

- Chapter 5 is centered on numerical simulation to evaluate the experimental results of a concrete cube preheated by temperature and then exposed to impact loads via finite element method (FEM) analysis.
- In the last section, Chapter 6 offers conclusions and recommendations, and it is succeeded by a compilation of the author's publications and extensive reference list.
- The final section of the thesis includes a list of publications that have been published during the current research.

Chapter 2: LITERATURE REVIEW

2.1 Introduction

The literature review provides a comprehensive examination and critical analysis of existing research and scholarly works relevant to the current study. It serves as the foundation for understanding the state of knowledge, identifying research gaps, and establishing the rationale for the present investigation. In the introduction, previous studies related to the detection of damage in concrete structures under the combined and individual effects of impact and temperatures is explored. Damage detection in concrete structures is of paramount importance for ensuring their structural integrity, safety, and longevity. Over the years, numerous researchers and engineers have focused their efforts on developing techniques and methodologies to accurately identify and monitor damages that can compromise the stability and functionality of concrete structures. The literature review begins by examining the various factors that contribute to the deterioration of concrete structures under the effect of impact and temperature loading conditions individually. Furthermore, the review explores the analysis techniques employed in previous studies. Extracting signature data from sensors and analysing them in different forms, such as evaluating structural parameters like mass, damping, and stiffness, have proven useful in assessing the severity and characteristics of damages. Comparisons between experimental and equivalent plots provide valuable insights into the performance of the structures. Additionally, the review investigates the impact of boundary conditions on damage detection. Fixed boundary conditions (FBC) have been examined to evaluate the behaviour and response of damaged structures under realistic scenarios. This analysis contributes to a better understanding of how damages manifest and propagate under different constraints. Lastly, the review discusses the validation of experimental results through finite element analysis. This numerical modelling technique serves as a powerful tool to verify and complement the experimental findings, providing a deeper understanding of the structural response and behaviour. By critically analysing the existing literature, this review aims to identify gaps, inconsistencies, and areas for further exploration. It sets the stage for the current study, which aims to investigate the effectiveness of various piezo configurations in detecting damage in concrete structures under different impact and temperature loading conditions, with a particular focus on fixed boundary conditions. The findings of this study contribute to the existing body of knowledge, providing valuable insights for future design, monitoring, and maintenance practices.

2.2 Impact Loading Effect on Concrete

2.2.1 Concrete Loaded In High Loading Rates

In the realm of structural design, traditional construction relies on standardized, static actions as outlined by design standards. However, there has been a noticeable surge in recognizing the significance of dynamic actions in recent times.

Throughout their lifespan, concrete and reinforced concrete constructions experience a range of quasi-static and dynamic movements. When faced with events such as earthquakes, bullet or aircraft impacts, blast wave propagation, collisions with vehicles or ships, or encounters with missiles, these structures endure typical dynamic stresses. The rapid progress of computer technology has enabled engineers to perform numerical analyses that effectively replicate intricate structural scenarios involving impact and blast loads. By utilizing numerical simulations, it becomes feasible to anticipate the extent of structural damage or load-bearing capacity ahead of time, thereby facilitating safety inspections, assessments, and the formulation of design guidelines to ensure structural integrity and overall safety.

2.2.2 Concrete's Behaviour under Dynamic Load

In the realm of concrete and concrete-like materials, there is a distinct focus on fracture and damage phenomena, especially considering their significantly higher strain rate sensitivity compared to brittle materials. It has been observed through various theoretical, experimental, and computational investigations that the dynamic properties of these materials can deviate from their static stress counterparts. The rate at which loading is applied has been proved to influence the compressive and tensile characteristics of concrete.

Different loading conditions exert varying levels of strain rates on a structure, making it essential to define each type accordingly. Figure 2.1 provides a schematic representation of typical strain rate ranges associated with various situations. In the realm of static or quasi-static circumstances, low levels of loading rates prevail, ranging from 10^{-6} to 10^{-4} s^{-1}. As structural dynamics come into play, a middle range of strain rates emerges, where the influence of inertia becomes significant. When studying concrete structures exposed to impact and fire, both numerical and experimental methods cover a broader strain rate range from 10^{-3} to 100 s^{-1}. At very high strain rates exceeding a rate of change of 10^{0} s^{-1} ($d\varepsilon/dt > 10^{0}$ s^{-1}), the influence of inertia becomes markedly substantial and must be duly considered.

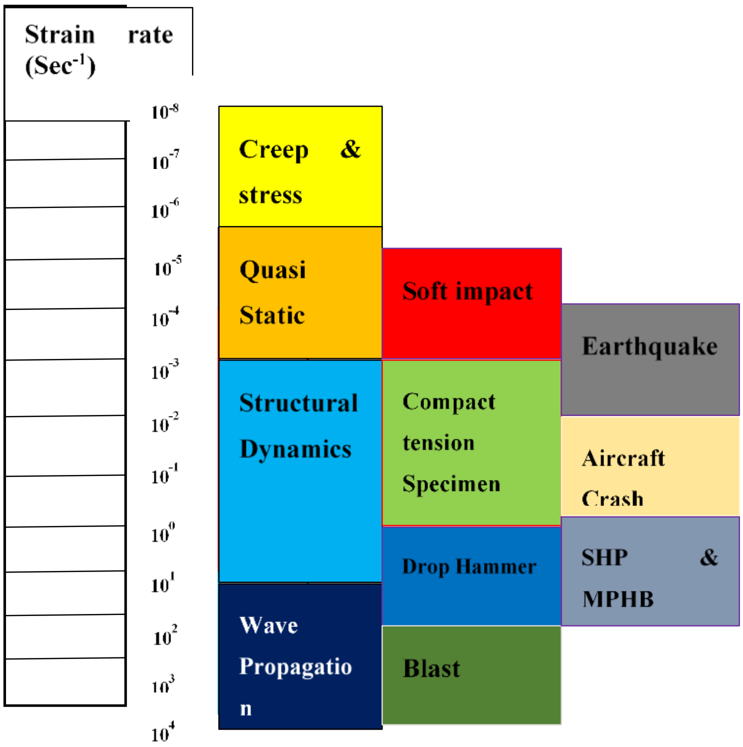

Figure 2.1 Possible strain rates for different loading cases Impact Load

When two bodies collide, the resulting phenomena can vary depending on the initial characteristics of the impacting bodies. The impact forces exchanged during the collision differ based on factors such as the material properties, initial impact velocity, type of structure being impacted, and the magnitude, extent, and severity of damage inflicted.

2.2.3 Classification of Impact Load

The classification of impacting bodies as "hard" or "soft" is determined by the relative deformability of the element compared to the target deformability, as described by Kennedy (1976). Eibl (1987) offers a definition for hard and soft impacts. The investigation at hand examines the collision between two bodies, where one is at rest and the other strikes with an initial velocity. In the analysis of the system, the collision between two masses, denoted as m_1 and m_2, is examined. To model the characteristics of the system, two variables, k_1 and k_2, are introduced. The stiffness k_1 represents the contact force between the two masses, while the stiffness k_2 is utilized to simulate deformation and the resistance force generated by the structure. This setup is illustrated in Figure 2.2.

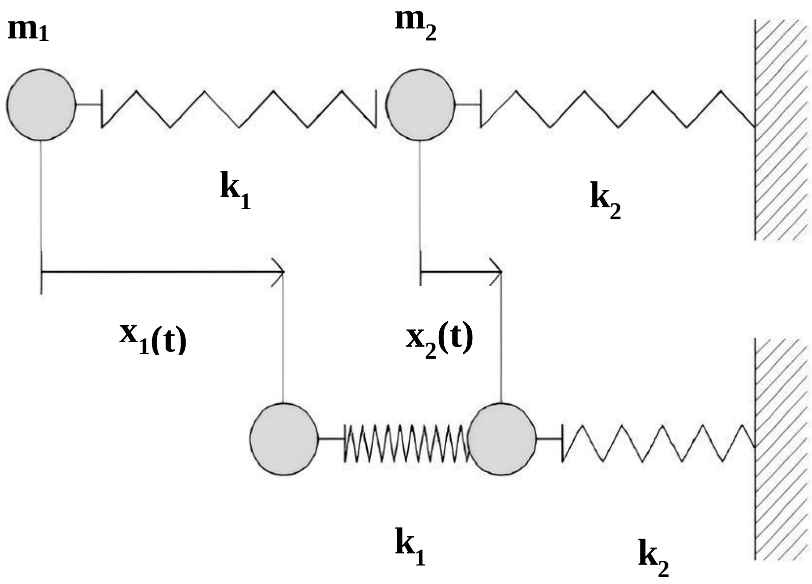

Figure 2.2 Simplified mechanical model for the impact problem proposed by Eibl (1987)

2.2.4 Phenomena of Impact

The response of a concrete structure to impact can vary based on the type of impact and the structural characteristics involved. Impact phenomena can typically be divided between the two parts which is global and local levels.

Global Level: In cases where a structure experiences uniform loading or if local failure conditions are not met during an impact event, the overall response of the entire structure is dynamic in nature as shown in Figure 2. 3. The inertial characteristics of a structure prompt an immediate response when subjected to external forces. In situations where the forces are brief, such as in explosions or minor shocks, the initial response is transient in nature. However, when the structural stress endures for a considerably extended period, surpassing its natural frequencies, as seen in earthquakes, a quasi-stationary vibration regime is established, leading to sustained global structural responses.

At the impact location, the observed strain rates surpass the strain rates achieved elsewhere in the structure. The theory of material strength offers a means to anticipate the structural behaviour through the analysis of plates and beams subjected to traction, compression, or bending. However, it is important to note that these behaviours can differ considerably from those observed under static pressure, particularly concerning failure modes and crack patterns (Jacky Mazars 2013).

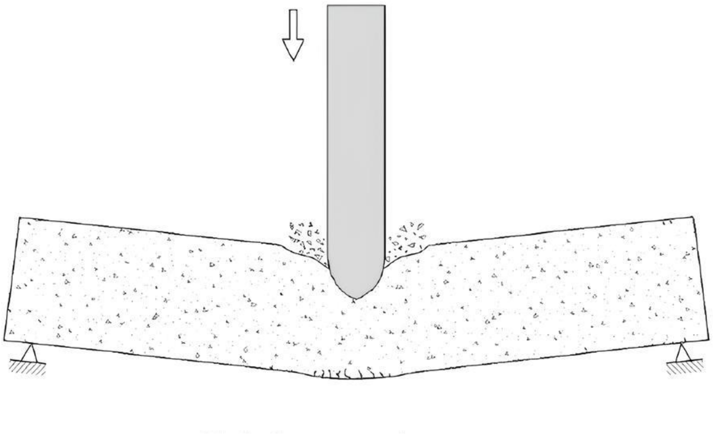

Figure 2. 3 Illustration of the global structural response to impact loading

Local Level: The region of impact undergoes notable stress and strain, particularly at very high strain rates and concurrent loading. It is crucial to take into account the effects of inertia, propagation of strain waves, and tri-axial stress states when studying local impacts. During this phase, phenomena such as scabbing and shear, accompanied by chip projections, occur when failure conditions are met.

Over time, various types of failure resulting from hard impacts have been observed and categorized (Kennedy 1976)). From Kennedy's research, six key local effects have been identified as depicted below and shown in Figure 2. 4.

1. Penetration: The impact site on the target body forms a crater, leading to material displacement.

2. Spalling: Ejection of target material occurs from the face of the impacted region.

3. Cone cracking and plugging: The projectile induces a cone-shaped crack, which may subsequently result in a punching-shear plug.

4. Radial cracking: Cracks propagate throughout the target, appearing on either the proximal or distal face of the concrete slab or even both.

5. Scabbing: Projectiles are expelled from the distal face of the target.

6. Cone cracking and plugging: The projectile causes a cone-shaped crack, which may later result in a punching-shear plug.

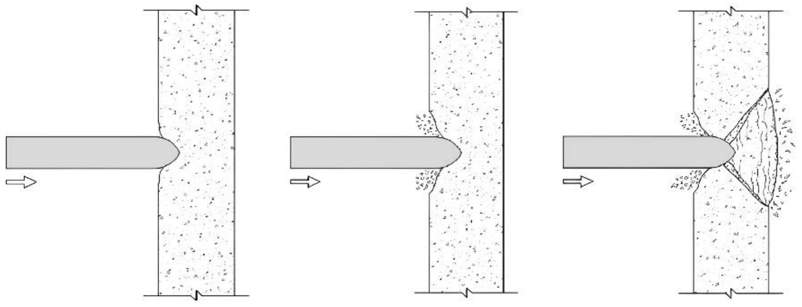

Penetration Spalling Cone Cracking

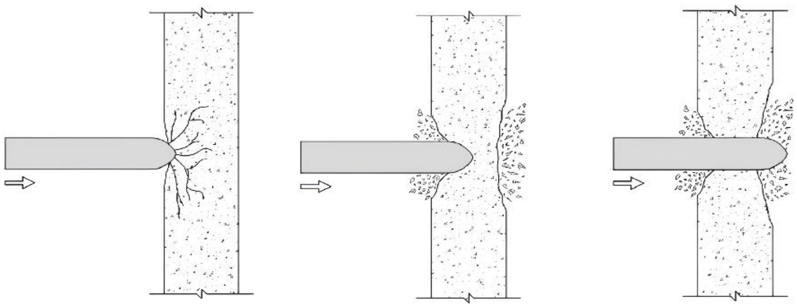

Radial Cracking Scabbing Perforation

Figure 2. 4 Effects of missile impact on a concrete target during a high-velocity impact

2.2.5 Experimental Studies on Concrete Structures under Impact Loading

Extensive research has been conducted in the past to understand the effects of impact loads on reinforced concrete members such as beams, slabs, frames, and more. These investigations have focused on examining both local and global structural failures resulting from impact events. The aim is to comprehensively understand the consequences of such loads on reinforced concrete structures at different scales, considering the specific behaviours and failure modes exhibited by these members. By studying the response of reinforced concrete elements to impact, valuable insights can be gained to enhance their design, durability, and overall safety.

2.2.6 Impact Testing on the Concrete Slab

Al et al.(2020) studied the behaviour of impact loading on the post-tensioned concrete slab with varying thicknesses. They have discussed the different behaviour of RC slabs on the basis of the different parameters of displacement, impact force crack and damage.

Yoo et al.(2020) has investigated the two-way sab under the low-velocity impact by strengthening the slab from the bottom by using four different methods. They found that the no-slump high-strength, high-ductility concrete (NSHSDC) is considered to have high impact resistance, even though it has lower resistance than the steel fibre-reinforced concrete and ultra-high-performance-concrete.

Loganaganandan et al.(2020) has performed the experimental study on two way concrete slab, strengthened with the GFRP strip with different thicknesses under the low-velocity impact and they found that the 75mm GFRP strip was more suitable than the 50 mm GFRP strip in alleviating damage volume ratio.

Mina et al. (2021) studied the behaviour of ultra-high performance fibre reinforced concrete (UHPFRC) slab under the projectile impact load. It was found that the mixture with a combination of 3 per cent steel fibres measuring 6 millimetres and 3 per cent steel fibres measuring 13 millimetres demonstrated the best resistance to projectile impact, and only the slabs with a thickness of 15 millimetres had perforation.

Bright Singh and Murugan (2021) conducted an experimental study for checking the performance of carbon fibre pervious concrete (CFRC) under impact loading and the results show that the 0.2 % carbon fibre has shown better performance under impact loading.

2.2.7 Impact Testing on Concrete Beam

The behaviour of impact load on concrete beam was studied by Bentur et al. (1986) under the 345 kg mass of drop impact at the 3 m height of impact and it is observed that the peak load of the specimens occurred within about 1 ms after contact for all the low velocity of 3 m impact.

Soleimani et al. (2007) has performed the experiment and checked the behaviour of RC beams under impact loading and revealed that the flexural load capacity of RC beams stayed constant after a specific impact velocity; subsequent increases in stress rate did not increase their load-carrying capability.

Pham and Hao (2016) investigated the effect of plastic hinge and boundary condition under the impact load on reinforced concrete beams and when compared to the peak displacement, the residual displacement is more susceptible to the boundary conditions. The impact force and displacement are not noticeably altered by changing the concrete's strength from 20 MPa to 100 MPa, however, the beam's failure mechanism is significantly impacted.

Jin et al. (2018c) performed experimental and numerical studies on steel fibres reinforced concrete beams under the impact load condition and The findings suggest that the addition of steel fibres and stirrups can enhance the impact-resistant properties of SFRC beams, including crack pattern, ductility, energy consumption capacity, and deformation recovery ability.

2.2.8 Impact Loading Effect on Cement Concrete Using PZT

Xu et al. (2017) has developed the embedded PZT-based dynamic internal normal stress sensor for the concrete under impact load testing and also determined the dynamic increase factors of concrete strength under impact loading and compare this value with the Comite´ Euro-International du Be´ton code and found a novel way of the measurement technique for finding the direct dynamic normal stress.

Fan et al. (2018) investigated the damage in a concrete column under impact loading using a piezo-based EMI technique and also developed a simulation-based model of the RMSD index and damage volume ratio and found that there was a linear relationship exists between them for the concrete for the particular simulation model.

Kumar et al. (2018) successfully experimented by analysing the behaviour of electromagnetic responses on the cement PZT composite under the effect of impact loading and results showed that the electromagnetic responses are very useful for the deformation monitoring.

Dixit and Bhalla (2018) has performed the experiment on a concrete cube for finding the damage under impact and fatigue loading using embedded PZT sensors. The results show that with the increase in the number of impacts the maximum strain values goes on increasing which indicate the damage condition.

Negi et al (2019) conducted experimental work for finding the damage in reinforced concrete slabs under the impact loading by using jacketed sensors and also developed the equivalent-based model and found that the developed equivalent-based model was more reliable than the damping-based model developed by (2018).

2.3 Temperature Loading Effect on Concrete

2.3.1 Properties of Concrete under the Effect of Temperature

During loading, as the temperature increases, the compressive strength and modulus of elasticity of concrete decrease, while the plastic deformation and ultimate strain increase. The strength of concrete is significantly influenced by its moisture content and the effectiveness of its curing process. To evaluate how temperature affects the compressive strength of concrete, CEB-FIP MC 10 offers empirical relationships. The method provided by Paul Beverly (2010) can be used to calculate the impact on the compressive strength of normal strength and normal-weight concrete when temperatures between 0 and 80 degrees Celsius are taken into account as shown in Equation 2.1.

$(T) = f_{cm} \cdot (1{,}06 - 0{,}003T)$ **(2.1)**

Where:

(T) is the compressive strength in MPa at the temperature T in °C

f_{cm} is the compressive strength in MPa at the temperature T = 20 °C

T is the temperature (Paul Beverly, 2010)

2.3.2 Concrete under the Effect of Elevated Temperature

Xia et al. (2006) has been experimentally tested the reinforcement concrete slab under the vibration condition periodically for 2 years. Their investigation revealed several noteworthy findings. Firstly, it was observed that frequencies exhibited a significant negative correlation with changes in temperature and humidity, indicating a clear sensitivity of frequency to these environmental factors. Additionally, damping ratios showed a positive correlation with variations in temperature and humidity. However, despite these correlations, no distinct link could be established between mode shapes and changes in temperature and humidity. To further understand these relationships, the researchers established linear regression models that establish connections between modal properties and environmental factors. The results of a quantification analysis highlighted that the primary factor influencing the variation in these properties is the change in the material's elastic modulus.

In a study conducted by Khan et al. (2013), the focus was on experimental investigations involving fly ash-based concrete subjected to high temperatures ranging from 100°C to 900°C.. The findings of the study revealed some significant trends. Initially, there was an increase in the compressive strength of the concrete as the temperature was raised, up to a point of 300°C. However, as the temperature continued to rise beyond this point, the compressive strength of the concrete showed a decline. Moreover, it was noted that the weight loss of the concrete increased in proportion to both the temperature and the content of fly ash.

Jiao et al. (2014) conducted a comprehensive examination of concrete's mechanical properties across a temperature range spanning from 20°C to 60°C. Their investigation encompassed an analysis of how temperature influences various factors, including cube compressive strength, splitting tensile strength, prism compressive strength, modulus of elasticity, and frequency.

In accordance with the research conducted by Wang et al. (2016), an experimental investigation was carried out to analyze the fire behavior of reinforced concrete slabs when subjected to combined uniaxial in-plane and out-of-plane loads. The findings from this study reveal that the presence of compressive uniaxial in-plane loads significantly influences both the quantity and orientation of cracks that develop on the upper surface of the concrete slabs during a fire event. Moreover, the slabs that were restrained uniaxial in-plane exhibited larger mid-span deflections and lower deflection recovery ratios compared to those without in-plane loading. Additionally, the test results highlight that increasing the reinforcement ratio proves to be an effective measure in preventing structural integrity failures in the restrained slabs.

Kodur (2018) focused on elucidating the behavior of high-strength concrete structural elements when exposed to fire conditions. The research delved into an explanation of the myriad factors that exert an influence on the fire performance of these structural members. Furthermore, the study proposed techniques aimed at enhancing the fire resistance of high-strength concrete structural elements.

2.4 Combined Effect of Impact and Temperature Loading

Researchers have recently emphasized the behaviour of concrete structures element (beam and slab) under both loading condition impact and temperatures.

Sharma et al. (2018) investigated the effect of low temperature on electromagnetic radiation from Soft PZT SP-5A under impact loading. They observed a reduction in EMR amplitude as the sample temperature decreased.

Abbas et al. (2021) developed an experimental setup was devised to detect fatigue cracks in stainless steel (304) beams utilizing the EMI approach. Furthermore, the researchers sought to evaluate the influence of temperature fluctuations on the electrical impedance of the piezoelectric sensors. A series of experiments was conducted under controlled temperature conditions, ranging from 25°C to 160°C, using a drying oven chamber (Q/TBXR20-2005). The findings of this experimental investigation indicate that the proposed methodology is suitable for real-time damage inspection in monitoring applications, even when subjected to temperature variations. Importantly, it has the capability to mitigate one of the significant causes of inaccurate fault diagnosis by compensating for the effects of elevated temperatures across an extended frequency bandwidth in structural health monitoring (SHM).

Al-ameri et al. (2021) conducted an experimental study to evaluate the effect of high temperatures on the repeated impact strength of normal strength concrete. They prepared seven identical sets of concrete patches, each containing six disc specimens. These specimens were subsequently subjected to testing using the ACI 544-2R repeated impact setup at both ambient temperature and following exposure to elevated temperatures of 100 °C, 200 °C, 300 °C, 400 °C,

Table 2. 1 Literature review of the concrete subjected to both impact and temperatures

Configuration of Impact loading and temperature	**Conclusions**	**References**
Mass of drop weight = 105 kg, Impact Velocity = 6.86m/sec, Heating Time = 0,30,60,90 min, Number of slab = 6	With an increase in heating time duration, mid-span deflection rises.	Liu et al. (2018)
Weight of hammer = 393 Kg A drop of impactor height = 1.5 m Velocity of Impact = 5.4 m/s Impact energy ($mv^2/2$) = 5730 J. Cylindrical Hammer = 200 mm Steel fibre volume fractions = 0 %, 1 % , 2 % and 3 % Different grades for the rebars = HRB400 and HPB300.	With more steel fibres, SFRC beams fail in flexure under impact loads, not shear. Steel fibre content has a minimal impact on the thermal and mechanical behaviour of damaged beams, limited to low-energy pre-impact.	Jin et al. (2018b)
Velocity of impact = 4 m/s , Three different temperature variations = 200 ^oC, 500 ^oC and 800 ^oC	80 % degradation of concrete strength with an increase in temperature	Nam and Hak-Chul Shin (2012)
Mass of iron ball = 4.54 kg (as per ACI 544 – 2R), Temperature variation = 100,200,300,400,500 and 600 ^oC, Size of disc = 150 mm diameter and 64 mm thick, Number and size of cube = 6 and 100 x100 mm Number and size of the prisms beam = 6 and 100 x 100 x 400 mm.	After exposure to 100 °C, compressive strength increased by less than 2%, but it decreased by more than 18 % when the temperature rises to 200 °C. For temperature rises to 300 °C, a partially recovered strength was then recorded. Finally, for 400 ^oC and beyond that, the compressive strength decreased continuously.	Al-ameri et al. (2021)
Weight of impactor = 0.5 kg, PZT Type = soft SP-5A Temperature variation = Low temperature under the range of 203–300 K	EMR signals exhibit a decreasing pattern as the temperature drops, and no phase change is visible in the XRD. PZT Young's modulus (E), with values ranging from 54 GPa to 69 GPa, exhibits an increasing pattern from 300 K to 203 K.	Sharma et al. (2018)
Dimensions of Steel beam = 350 x 30 x 4 mm, Frequency range = 25 kHz -175 kHz, Temperature Variation = 25 ^oC – 160 ^oC	Critical frequency shifts increase as temperature and excitation frequency rise.	Abbas et al. (2021)

and 500 °C. Additionally, six cubes and six prisms from each set were employed to assess the remaining compressive and flexural strengths under the same environmental conditions. The test results revealed that when specimens were heated to 100°C, there was only a slight reduction of 2.4% and 3.5% in the numbers of cracking and failure impacts, respectively. However, exposure to higher temperatures resulted in a more rapid deterioration of impact resistance compared to compressive and flexural strengths. The behaviour of concrete structures was studied by varying some key parameters of impact loading and temperature, such as the mass of the impactor, velocity of the impactor, geometry of the impactor, and at higher degrees of temperature. The literature review of the concrete structures subjected to both impact and temperatures is shown in Table 2. 1.

2.5 Electro-Mechanical Impedance Technique Using PZT Patches

In this section, we will begin by exploring the underlying physical principles of the EMI technique, delve into the selection of the frequency range, and also touch upon the significance of temperature. Additionally, a brief overview of the temperature compensation technique will be provided.

2.5.1 Physical Principles

In the EMI approach, a PZT patch is affixed to the surface of the monitored structure using a durable epoxy adhesive. This patch is then electrically stimulated through an inductance, capacitance and resistance using LCR meter. In this setup, the PZT patch functions as a thin plate, undergoing axial vibrations and interacting with the host structure, as illustrated in Figure 2. 5 (a and b). These interactions manifest as electrical admittance, encompassing both conductance and susceptance. Assuming one-dimensional (1D) interaction and treating the host structure as a skeletal framework, the PZT patch-host structure system can be modelled as a mechanical impedance connected to a slender bar (the patch) undergoing axial vibrations, as depicted in Figure 2. 5 (a). In this figure, the patch expands and contracts dynamically in the '1' direction when an alternating electric field E_3 (uniform across space, i.e., $\partial E_3/\partial x = \partial E_3/\partial y = 0$) is applied in the '3' direction. The patch is characterized by its half-length 'l', width 'w', and thickness 'h'. The direct and converse effects can be mathematically expressed, as described by Ikeda (1990) as shown in Equation 2.2 and 3.3.

$$D_3 = \overline{\varepsilon_{33}^{T}} E_3 + d_{31} T_1 \qquad \textbf{(2.2)}$$

$$S_1 = \frac{T_1}{\overline{Y^E}} + d_{31} E_3 \qquad \textbf{(3.3)}$$

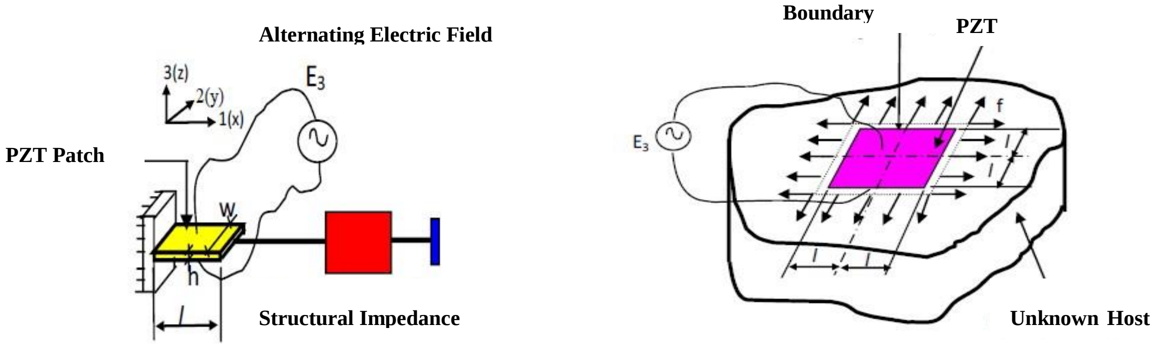

(a) Modelling of PZT-structure interaction (1D)

(b) A PZT patch bonded to the host structure (2D)

Figure 2. 5 Bonded PZT patch and its interaction (a) Modelling of PZT-structure interaction (1D) (Bhalla et al. 2003) **(b) A PZT patch bonded to the host structure (2D)**

In the given configuration, the coordinate system has axis '3' pointing along the thickness of the PZT patch, while axes '1' and '2' lie in the patch's plane, as shown in Figure 2. 5 (a). Where S_1 represents the strain value in direction ‘1’. D_3 is the electric displacement over the PZT patch, the piezoelectric strain coefficient is d31, E_3 is the external electric field and T1 is the axial stress in direction ‘1’. $\overline{Y^E}$ is the complex Young’s modulus of elasticity of the PZT patch at a constant electric field as shown in Equation 2.4

$$\overline{Y^E} = Y^E\,(1 + \eta i) \qquad \textbf{(2.4)}$$

$\overline{\varepsilon_{33}^T}$ is the complex electric permittivity in direction ‘3’ at constant stress as shown in Equation 2.5

$$\overline{\varepsilon_{33}^T} = \varepsilon_{33}^T(1 - \delta i) \text{ with } i = \sqrt{-1} \qquad \textbf{(2.5)}$$

Where η and δ represent the mechanical loss factor and the dielectric loss tangent respectively. Moreover, it is assumed that PZT loading in the '3' direction can be neglected when the frequencies involved are substantially lower than the first resonant frequency for thickness vibrations. Furthermore, the vibrating patch is considered to be exceedingly small, with minimal mass and stiffness in comparison to the host structure.

2.5.2 Frequency Range Selection

The distinctive quality of the EMI approach is that it exhibits high-sensitivity behaviour and operates at a high-frequency range of 50 to 500 kHz. Sun et al. (1995) recommended choosing the frequency range based on the inclusion of the structure's major vibration modes. Based on very sensitive behaviour to early damage that is imperceptible to the naked eye, Bhalla (2001) advised that the frequency range be kept under the range of 30 to 400 kHz. Additionally, it was advised that the frequency range beyond 500 kHz was unsuitable since PZT patches exhibit extreme sensitivity to the boundary condition.

2.5.3 Effect of Temperature

Sun et al. (1995) and Park et al. (1999) found that the impedance analyzer's electrical admittance characteristics are highly temperature-sensitive. Several researchers Park, G. (1995) and Bhalla (2001) have studied the effect of temperature on the PZT Patch and the observation revealed a consistent linear relationship between temperature and the total shift in the frequency spectrum within the constrained frequency range.

In a study conducted by Bhalla et.al (2004), an analysis was carried out to investigate the impact of temperature on PZT (Lead Zirconate Titanate). The findings revealed that the horizontal shifts observed in the acquired signature were primarily attributed to alterations in Young's modulus of the host structure. On the other hand, the vertical shift was found to be associated with changes in the parameters d_{31} and ε_{33} of the PZT patch.

2.5.4 Temperature Compensation Technique

The compensation technique for correcting the horizontal shift of the acquired signature based on the cross-correlation coefficient was investigated by Sun et al. (1995). Further (Park et al. (1999) introduced an empirical-based methodology aimed at temperature compensation. Their proposed approach demonstrated the efficacy of the EMI technique in detecting damages even in the presence of temperature fluctuations.

Sepehry et al. (2011) introduced a novel method for temperature compensation in impedance-based structural health monitoring (ISHM) using artificial neural networks (ANNs). Their study demonstrated that the proposed method, employing ANNs, effectively compensated for temperature variations, enabling reliable damage detection in various structures.

Baptista et al. (2014) conducted an experimental study to investigate the influence of temperature on a 5H PZT patch using the EMI technique. The experimental analysis involved the examination of variations in both amplitude and frequency. This was accomplished using an aluminium specimen, and impedance signatures were obtained at a range of temperatures spanning from 25°C to 102°C. The study delved into an analysis of variations in both amplitude and frequency within the acquired data due to temperature effects. The research findings revealed that changes in the amplitude of the impedance signatures were correlated with the temperature-dependent behavior of the piezoelectric sensor's capacitance. Furthermore, it was observed that the frequency shifts of resonance peaks resulting from temperature fluctuations were not consistent across the entire frequency spectrum but increased proportionally with frequency.

Baral et al (2023), implemented the temperature compensation technique for a reusable piezo configuration to monitor metallic structures. The compensation values were derived from experiments conducted on piezo sensors, both under free boundary conditions and when bonded to a metallic host structure. The researchers effectively established a relationship that allows for the detection and evaluation of potential structural damage. The findings of this study hold promise for compensating for variations in the structure's signatures caused by temperature fluctuations within the conductance signature.

2.5.5 Sensing Range and Positioning of PZT

The EMI technique typically utilizes excitation frequencies ranging from 30 to 400 kHz. This high-frequency excitation results in localized actuation and sensing zones.

Esteban (1996) conducted comprehensive theoretical modelling to determine the sensing region of the EMI technique. Based on several case studies, it was determined that the sensing zone closely correlates with the host material and its density. This zone typically ranges from about 0.6 meters in concrete to 2-3 meters in metal. Consequently, when implementing PZT patches in real-world applications, it is crucial to judiciously choose the spacing between them, considering the factors mentioned above.

Soh and Bhalla (2005) recommended that PZT patches should be strategically positioned at critical locations that are prone to shear cracks and bending failures. This optimization allows for the efficient deployment of PZT patches, reducing the overall number required to monitor the entire structure.

2.5.6 Voltage Excitation and Acquisition of Signature

Ordinarily, the PZT patch receives excitation through an LCR meter, employing an alternating voltage signal with a root mean square (r.m.s.) value of 1 volt across a frequency range defined by the user. Sun et al. (1995) observed that the conductance signature remains nearly constant even when the excitation voltage is varied from 0.5 to 15 volts.

2.5.7 Instrumentation and Other Considerations

To acquire comprehensive impedance or admittance signatures, it is essential to measure both the real and imaginary components of impedance. This can be accomplished with LCR meters such as the Agilent E4980A Precision LCR meter and the Wayne Kerr Precision Impedance Analyzer. These instruments are specifically engineered for accurate impedance measurements.

Peairs et al. (2004) were the first to investigate hardware-related issues and proposed a cost-effective version of the EMI technique using a Fast Fourier Transform (FFT) analyser, which is more affordable compared to LCR meters.

2.6 Significant Research on the Electromechanical Impedance Approach

Extensive investigations have established the capabilities and advantages of the EMI technique. Over the past two decades, numerous researchers have made significant contributions to the field. Park et al (2003) and Bhalla et al. (2004) have provided comprehensive reviews of the advancements in the EMI technique, including detailed case studies and applications since its inception in 1995.

In their study, Kim et al. (2019) conducted an examination of the concrete performance assessment in crack restoration using the PZT-based EMI (Electromechanical Impedance) approach. An experimental setup is shown in Figure 2. 6. To ensure accuracy, they carefully selected a frequency range that effectively captures the structural condition. This selection considered the trends of four damage indicators and the varying degrees of damage within each sub-frequency range. Their findings demonstrated that the proposed method successfully assesses how well the fracture-healing material recovers over time. This research highlights the effectiveness of the PZT-based EMI approach as a reliable tool for monitoring and gauging the restoration progress of cracked concrete structures.

Su et al. (2019) in their research, a PZT-based EMI method was employed to monitor the early-age properties of cementitious materials. The study aimed to validate the effectiveness of the lead zirconate titanate (PZT)-based EMI approach in accurately tracking the increase in compressive strength and elastic modulus of mortar during very early ages (4th–8th hour) and young ages (1st, 3rd, and 7th day). EMI signatures were measured for each sample throughout the study, followed by post-processing. The research findings revealed that the RMSD index outperformed the other two statistical indices in accurately tracking the strength gain of cementitious materials. This underscores the reliability and precision of the PZT-based EMI approach as a suitable method for effectively monitoring and evaluating the early age properties of mortar.

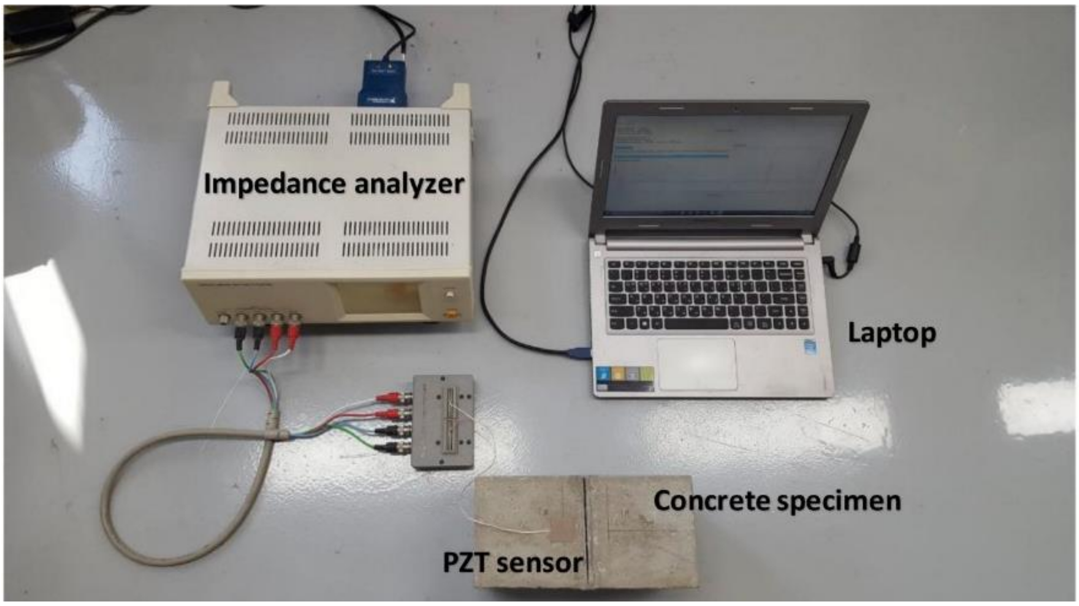

Figure 2. 6 Experimental setup (Kim et al. 2019)

Xu et al. (2019) in their study investigated the monitoring of the looseness of Bolted Spherical Joint (BSJ) connections using the Electro-Mechanical Impedance (EMI) technique and Backpropagation Neural Networks (BPNNs). For their experimental assessment, they utilized a space grid specimen featuring bolted spherical joints and tubular bars. To replicate various levels of joint connection looseness, they applied different levels of torque to the sleeve. With increasing torque levels, the degrees of joint connection looseness also increased. To facilitate monitoring, the researchers incorporated a lead zirconate titanate (PZT) patch into the tubular bar, leveraging its significant piezoelectric effect. The root-mean-square deviation (RMSD) of the conductance signatures from the PZT patch played a pivotal role as the primary monitoring index for assessing the degree of looseness. In a series of twenty repeated tests, the RMSD values from sub-frequency bands and the degrees of looseness were employed as input and output parameters, respectively, to train and evaluate the Back-Propagation Neural Networks (BPNNs). The experimental results demonstrated that the proposed approach effectively detected the formation of bolt looseness by analyzing changes in the looseness-monitoring indexes. Moreover, the trained BPNNs accurately determined the degree of bolt looseness. Overall, this research successfully showcased the feasibility of the Structural Health Monitoring (SHM) technique for effectively monitoring the looseness of bolted spherical connections in space grid structures.

Jothi and Singh (2022b) has focused on the process of diagnosing damage in a smart PZT transducer that was adhesively bonded. It considered the coupled electro-mechanical behavior of this system. To address the shear lag effect, a parametric analysis was conducted to assess variations in adhesive properties. This innovative approach was developed to enable the early detection of damage within both the PZT transducer and its adhesive bond layer as a crucial part of the Structural Health Monitoring (SHM) process. The method initially involved simulating damage to the PZT patch and bonding layer. Subsequently, the corresponding Electromechanical Impedance (EMI) signatures were determined through numerical modeling and simulations. This type of damage leads to vertical displacement without inducing any changes in the horizontal direction, thereby effectively detecting sensor damage and adhesive debonding. Subsequently, more robust continuum-based impedance equations are applied to validate the simulation outcomes for the single piezo arrangement. The investigation revealed the significance of the real part of the admittance signature in sensor diagnosis, emphasizing its reliability and critical role. As a result, it becomes possible to identify and distinguish sensor faults such as debonding and breakage effectively.

In the investigation conducted by Lan et al. (2023), Electromechanical impedance (EMI) based spherical Smart Aggregates (SSAs) were studied for their effectiveness in monitoring soil water content. The researchers conducted an experimental study using these spherical smart aggregates to assess soil water content levels. To quantify the impedance signatures detected under different soil water concentrations, three types of statistical indices were utilized: root mean square deviation, mean absolute percentage deviation, and correlation coefficient deviation. The experimental findings demonstrated that SSAs exhibited higher sensitivity and stability in monitoring soil water content compared to conventional Smart Aggregates (SAs). This investigation aimed to understand how temperature fluctuations could affect the efficacy of the monitoring system. Overall, the study by Lan et al. highlights the potential of EMI-based spherical Smart Aggregates in efficiently monitoring soil water content, providing valuable insights for future applications in the field of soil monitoring and management. The results demonstrate that temperature influences the monitoring results of the SSAs based on the EMI technique.

Maurya et al. (2023) has performed an experimental study to find the potential of fracture healing in bacterial concrete structures, evaluated using the EMI approach and a PZT patch. The experimental investigation aimed to assess the effectiveness of this concept for healing cracks in concrete. To examine the crack healing performance, statistical damage indices were employed within a pre-evaluated ideal frequency band. The researchers used the damage indicators RMSD, MAPD, and CC to assess damage severity, while Cov was found suitable for evaluating damage severity within a smaller sub-frequency range. The damage indicators RMSD, MAPD, and CC proved to be suitable for assessing the severity of damage. However, Cov was found to be more appropriate for evaluating damage severity in cases involving smaller amounts within a sub-frequency band. The evaluated damage indicators RMSD, MAPD, Cov, and CC successfully signified the crack healing by the bacterial incorporation in concrete structures.

Krishnanunni et al. (2023) explored the efficacy of singly curved thin piezo transducers for both structural health monitoring and energy harvesting in Reinforced Concrete (RC) structures. The study focused on the hitherto unexplored capability of curved piezo transducers in damage detection using the electro-mechanical impedance (EMI) technique. Experimental investigations were conducted to compare the performance of curved piezo transducers with straight configurations. A finite element (FE) analysis was conducted using a 3-D model of a full-scale reinforced concrete (RC) beam that incorporated both straight and curved piezoelectric transducers. This analysis assessed various parameters, including the bend angle, thickness, number of elements, and the placement position of the curved transducers for energy harvesting. The FE simulations disclosed an optimal range for the bend angle, highlighting that angles between 130 and 160 degrees yielded the most promising results. Additionally, an increase in transducer thickness had a substantial impact on the open-circuit voltage generated during energy harvesting. The numerical analysis also indicated that optimal placement of the piezo transducers toward the top or bottom of the beam cross-section resulted in the most favorable outcomes. The combined results from both experimental and numerical investigations carry substantial practical implications for the effective utilization of curved piezo transducers in real-world Reinforced Concrete (RC) structures. They offer valuable insights for achieving improved energy harvesting efficiency and enhancing structural health monitoring capabilities.

2.7 Non Bonded Piezo Sensors

Yang et al. (2010), in their study, introduced the use of a reusable PZT patch for monitoring cement hydration and structural health. They affixed a PZT patch, measuring 20×20×0.5 mm, to a plastic enclosure and an aluminum sheet. To secure it, they utilized two bolts tightened within drilled holes in the enclosure, as depicted in Figure 2. 7 (a). During the initial data acquisition on the concrete cube during casting, the bolts were properly unscrewed. To protect the PZT patch from water interference, which could hinder its functionality, they utilized a plastic DIP covering as depicted in Figure 2. 7 (b). Nonetheless, this protective enclosure had the drawback of reducing the sensitivity of the PZT patch. A schematic representation of the sensor setup is illustrated in Figure 2. 7 (c).

(a) (b) (c)

Figure 2. 7 Bolt with enclosure reusable PZT setups (Yang et al. 2010) (a) reusable set and (b) waterproofed reusable setup (c) schematic of the sensor setup.

The repeatability of a piezo sensor is subject to various factors, such as the quality of the PZT transducer, human errors, and the modulus of elasticity. To evaluate repeatability, the researchers carried out experiments in a frequency range spanning from 70 kHz to 120 kHz, repeating the measurements four times. They utilized both thicker (20×20×2mm) and thinner (20×20×0.5mm) piezo sensors, with the thicker PZT patch having four times the magnitude of the thinner one. The results showed that the sensitivity of the thicker patch was higher compared to the thinner PZT patch. Additionally, under similar bonding conditions, the repeatability of the thicker PZT patch was found to be superior, indicating its ability to provide more consistent and reliable measurements compared to the thinner counterpart.

Tawie and Lee (2011) proposed an innovative solution to overcome the challenges of monitoring the setting time of cement mortar. They introduced a setup where the sensor was attached to the bolt and fixed with different lengths of rods. This novel configuration proved to be highly effective and efficient in monitoring the cement mortar's setting time in real-field conditions using an impedance analyser. One of the significant advantages of this setup is its reusability, allowing for easy detachment and use in repetitive tests. In this approach, the conventional Vicat's needle equipment, used for determining setting time and moisture loss, was substituted with a reusable setup designed to monitor the hydration process of very early-age concrete. The setup exhibited outstanding capabilities in damage estimation for hardened mortar and exhibited lower sensitivity to fine localized cracks when compared to surface-bonded PZT sensors. In Figure 2. 8 (a), you can observe the setup with varying rod lengths, while Figure 2. 8 (b) displays the reusable sensor positioned over the concrete cube, underscoring its practicality and adaptability for a range of monitoring applications.

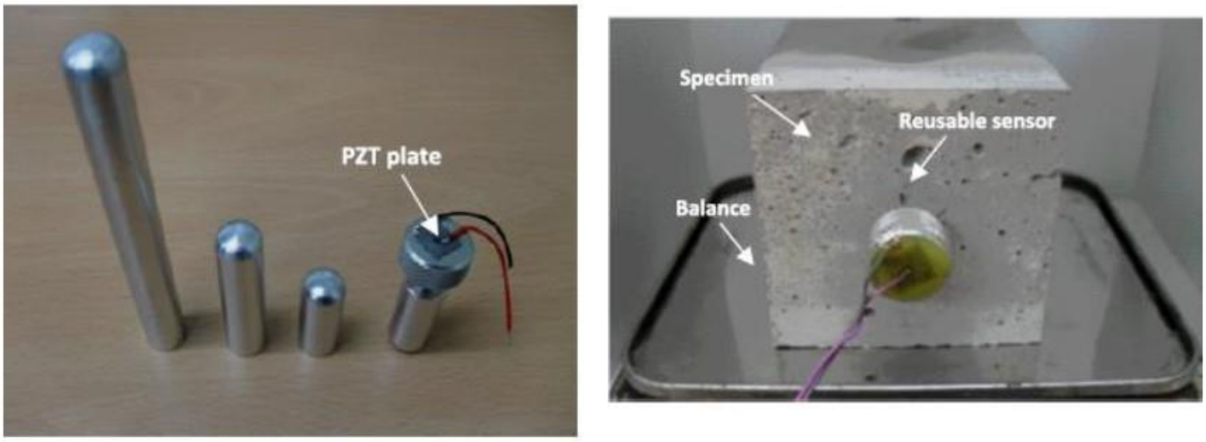

(a) (b)

Figure 2. 8 Bolt with reusable rod setup (Tawie and Lee 2011) (a) different lengths of rods (b) shows the sensor on the concrete cube.

Na et al. (2012) in their study, introduced a novel setup based on a magnet for easy installation and removal in composite or metallic structures. They utilized the Electro-Mechanical Impedance (EMI) technique to evaluate the performance of this setup with the sensor. To eliminate temperature errors, all measurements were taken at a controlled room temperature of 24±0.3 ºC. The reusable setup consisted of a commercial neodymium magnet with a tetragonal crystalline structure of Nd2Fe14B. They prepared the setup with varying thicknesses of the magnet, namely 3mm, 5mm, and 10mm. To ensure better repeatability, they performed a repeatability test by detaching and reattaching the specimen three times. For achieving improved repeatability, it was crucial to fix the position of the PZT transducer with no displacement during the test. Even small movements could lead to significant changes in the impedance signature, potentially leading to false results. Figure 2. 9 illustrates the reusable setup, highlighting its practicality and effectiveness for monitoring composite or metallic structures using the EMI technique with the magnet-based approach.

To address the challenges associated with the bonding of PZT patches in complex geometric structures due to their brittle nature, Na et al. (2013) developed an innovative coupling setup using steel wire and PZT patches. The researchers explored various combinations of steel wire lengths and diameters along with different sizes of PZT sensors. Thicker steel wire was found to produce higher amplitude in the resonance frequency range. They discovered that using different sizes of PZT sensors, such as 3×1 cm for sensing larger areas and 2×1 cm for monitoring cracks with higher frequencies, was suitable for specific monitoring purposes. This

(a) (b)

Figure 2. 9 Reusable setup (Na et al. 2012)

coupling setup proved effective in monitoring the progressive damage, debonding, and deterioration of adhesive bonding in composite layers. It provided valuable insights into the structural health of complex structures. Figure 2. 10 illustrates the proposed steel wire setup, demonstrating its applicability for monitoring complex structures and overcoming challenges related to PZT bonding in such scenarios.

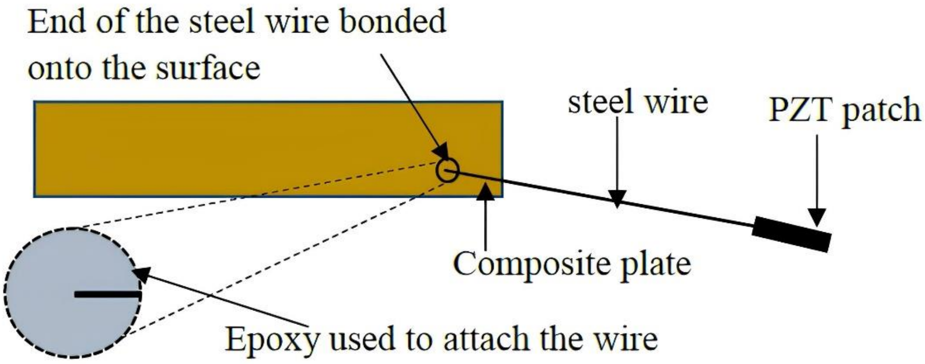

Figure 2. 10 Steel wire setup (Na and Lee 2013)

Providakis et al. (2013) introduced a Non-destructive Wireless Monitoring of Early-Age Concrete Strength Gain using an innovative Electromechanical Impedance (EMI) sensing system. They developed and tested an active wireless USB sensing device, which included a compact EMI measurement chip and a reusable piezoelectric transducer housed in a container made of Teflon. This configuration was developed for efficient monitoring of concrete strength development during its early ages and initial hydration stages. The researchers analyzed changes in the electromechanical impedance signatures obtained through the suggested sensing device across the entire early-age concrete hydration process. The results showed that the proposed EMI sensing system, when used in conjunction with a well-defined statistical index for assessing the pace of concrete strength development, demonstrated a high sensitivity to the early progression of concrete strength. This innovative system offers a reliable and non-destructive method for monitoring concrete strength development, providing valuable insights into early-age hydration processes.

Bonding PZT patches directly onto remote structures is challenging or even impossible due to their fragile nature. In response to this, Naskar and Bhalla (2016) proposed a metal foil-based Electromechanical Impedance (EMI) technique for such structures. They substituted the steel wire with a metal foil, leading to a substantial enhancement in the sensitivity of damage detection. To reduce the number of required piezo sensors for damage detection, they developed an algorithm specifically designed for field application using the metal foil-based (MFB) variant. This variant of MFB was initially simulated using the finite element method and subsequently integrated with a fundamental impedance model. To assess the algorithm, the researchers conducted a numerical simulation of a mild steel plate measuring 1200mm×3970mm×38mm, and subsequently applied it to the physical plate with multiple damage locations. Figure 2. 11 showcases the enhanced MFB variant designed for damage detection, providing a viable and efficient solution for monitoring delicate or remote structures using the improved metal foil-based EMI technique.

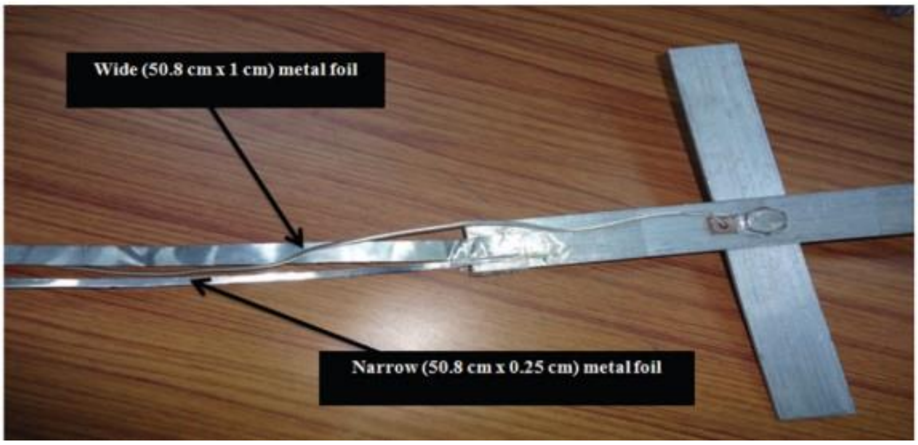

Figure 2. 11 Specimen with wide and narrow metal foil (Naskar and Bhalla 2016)

2.8 Surface Bonded Piezo Sensors

Soh and Bhalla (2005) introduced a novel approach for the non-destructive evaluation of concrete, this study addresses both strength prediction and damage assessment through the application of the electro-mechanical impedance technique. A newly developed empirical method is proposed for the non-invasive assessment of in-situ concrete strength using admittance signatures acquired from surface-bonded piezo-impedance transducers. Subsequently, the research focuses on the identification of suitable impedance parameters specific to concrete. These identified parameters demonstrate sensitivity not only to structural damages but also to the concrete's strength development during the curing process. To validate the methodology, a series of comprehensive tests were conducted on concrete specimens until failure, enabling the empirical calibration of the identified characteristics of the system with varying degrees of damage severity. Moreover, a novel empirical fuzzy probabilistic damage model is introduced to quantitatively anticipate the extent of damage in concrete. This model is based on the observed fluctuations in the identified equivalent stiffness. The integration of this model enhances the understanding of concrete behaviour under different conditions and offers a practical approach to evaluating structural integrity and potential damage in concrete structures.

Shin et al. (2008) expand the utility of the EMI (Electro-Mechanical Impedance) sensing technique for monitoring the strength gain of early-age concrete. To accomplish this, PZT (piezoelectric lead zirconate titanate) patches are employed to capture the EMI signature while the concrete cures. The effectiveness of the EMI sensing technique is rigorously examined through a series of experiments on concrete specimens. The results obtained from these experiments reveal the promising potential of the EMI sensing technique as a practical and dependable non-destructive method for monitoring the strength gain in concrete during its early stages of development. This breakthrough can significantly contribute to better understanding and managing the curing process of concrete structures, thereby enhancing their overall performance and durability.

Shin and Oh (2009) explores the viability of utilizing the EMI sensing technique to monitor the online strength gain of early-age concrete. The investigation involves an experimental study conducted on concrete specimens equipped with piezoelectric patches for sensing. Remarkably, the results demonstrated that the EMI signature exhibits high sensitivity to the strength gain occurring during the early stages of concrete development. This finding signifies the potential of the EMI sensing technique as a valuable tool for real-time monitoring and assessment of concrete's strength progression during its critical early phase.

Tawie and Lee (2010) studied the application of the EMI sensing technique for on-site monitoring of concrete through the utilization of cost-effective piezo ceramic (PZT) patches. To accomplish this, the study cantered around monitoring the resonant frequencies of these PZT patches affixed to the surface. An impedance analyzer was used with a frequency range spanning from 100 to 400 kHz for this purpose. The experimental results obtained from this study confirmed the practicality and efficacy of the EMI method for effectively monitoring the concrete strength development. In addition, a quantitative approach is presented, employing statistical metrics such as RMSD (Root Mean Square Deviation), MAPD (Mean Absolute Percentage Deviation), and CCD (Coefficient of Correlation Deviation) to compare the EMI spectra. Overall, this research offers a comprehensive framework for utilizing the EMI sensing technique with low-cost PZT patches, enabling real-time and reliable in situ monitoring of concrete strength development, which can significantly contribute to the assessment and optimization of concrete structures' performance and longevity.

Narayanan et al. (2018) investigates the dynamic response of a PZT patch subjected to an applied electrical potential at multiple frequencies. The bonded PZT patch's electrical conductivity spectra displays peaks that are tightly spaced and narrow, with their characteristics being influenced by the size of the substrate. When a PZT patch is bonded to a concrete cube, these closely-spaced peaks in the electrical conductance response correspond to the structural modes of the cube. These local peaks are observed in conjunction with the baseline electromagnetic (EM) response of the bonded PZT patch. There is a limited zone of influence for each resonant mode of the bonded PZT patch in the electrical conductance spectrum, and the outer boundary has little influence outside of this zone. This investigation provides valuable insights into the complex dynamics of PZT patch interactions with concrete substrates, offering potential applications for understanding and optimizing the behaviour of such systems.

Su et al. (2019) validating the reliability of utilizing the lead zirconate titanate (PZT) based EMI method for monitoring the compressive strength gain and elastic modulus of mortar. The study encompasses the monitoring of both very early-age (4th–8th hour) and early-age (1st, 3rd, and 7th day) concrete development. To achieve this, an extensive series of experiments and data analysis is conducted on ten different concrete mixtures, varying in water-to-cement ratio and using Type I & III cement. EMI signatures were acquired for each sample during the designated time intervals and subsequently subjected to analysis using three statistical models: RMSD, CCD, and MAPD, employed as evaluation indices. Among these three statistical indicators, the RMSD index was determined to be the most precise for monitoring the strength development of cementitious materials. Overall, the findings collectively demonstrate the feasibility of using the piezoelectric-based EMI method to effectively monitor the early-age strength development of cementitious materials, irrespective of the concrete mix design. This research contributes valuable insights into non-destructive testing methods and their potential application in early-age concrete assessment and quality control.

2.9 Embedded Piezo Sensors

Annamdas and Rizzo (2010) develop and implement a robust and embeddable sensing system capable of monitoring the curing process, stress levels, and damage in concrete structures. To achieve this objective, three concrete cylinders were cast and tested, each equipped with in-house designed sensors. Furthermore, the study utilized surface-bonded PZT patches to compare the response of conventional PZT patches with the embedded sensing system. Following the standard 28-day curing period, two cylinders were subjected to compression tests, while the third cylinder was intentionally damaged. The electromagnetic (EM) signatures collected from the sensors were subjected to analysis using a statistical index and a slope gradient analysis. The outcomes highlight the efficiency of the sensing system and the EMI method in tracking the curing process progression and identifying the initiation of stress, damage onset, and damage propagation within the concrete structures. Overall, this research provides valuable insights into the practical application of the designed sensing system, offering a promising approach for real-time monitoring and evaluation of concrete structures' health and integrity throughout their lifespan. The rugged and embeddable nature of the system makes it a valuable tool for improving the overall safety and durability of concrete infrastructure.

Annamdas et al. (2010) introduce a simple and efficient method for embedding PZT sensors in concrete to monitor both fresh and cured states. The fundamental principle involves recording EM admittance signatures resulting from PZT actuators in the presence of an electric field. Anomalies or disturbances within the concrete structure can be detected through deviations in these signatures during the monitoring period. In this context, the emphasis is on embedding PZT sensors within the host structure to enhance durability and shield them from surface-related issues such as vandalism and finishes. The study introduces a dual protection wrap technique that integrates elements of both metal and non-metal materials. The initial layer of protection involves a steel wire mesh, serving as a bonding connector between the PZT and the host structure. The second protection is offered by a layer of cement paste, forming a connection between the concrete and the wire mesh. The suggested approach was confirmed through experiments conducted on a variety of laboratory-sized concrete cubes, and the findings were thoroughly scrutinized using statistical analysis. The results demonstrate the efficacy and reliability of the double protection wrap approach for embedding PZT sensors in concrete, providing a robust and practical solution for monitoring concrete structures' health and integrity throughout their lifecycle.

Wang and Zhu (2011) introduces a waterproofing process for PZT patches using asphalt lacquer material, enabling their use as embedded transducers in concrete. The monitoring procedure involves monitoring the PZT admittance signals (inverse of impedance) and assessing the compressive strength of concrete cubes at different ages. By combining this data with the RMSD and MAPD indices, correlations are established between concrete strength gain and RMSD, as well as its correlation with MAPD. The obtained results underscore the feasibility and efficacy of this novel EMI (Electro-Mechanical Impedance) method based on embedded PZT transducers for monitoring the early-age strength development. This approach presents a promising solution for non-destructive evaluation and real-time assessment of concrete structures, contributing to improved construction practices and enhanced durability.

Kong et al. (2013) monitoring the hydration characterization of very early-age concrete using piezo ceramic-based smart aggregates (SAs). The SA transducer features a sandwich structure consisting of two marble blocks and a pre-soldered lead zirconate titanate (PZT) patch. In this design, the PZT patches serve dual functions as both actuators and sensors, leveraging the piezoelectric properties of these materials. The marble blocks serve as essential components for protecting the fragile PZT patch, making the SA a robust embedded actuator or sensor within the concrete structure. The experimental investigation conducted in this study utilizes an active-sensing approach, involving a pair of smart aggregates, one acting as an actuator and the other as a sensor. This research effectively examines three distinct states of very early-age concrete hydration: the fluid state, transition state, and hardened state. These states are characterized based on the analysis of the received electrical signal, with a particular focus on the amplitude and frequency response of this signal. This research showcases the potential of smart aggregates as effective tools for monitoring and understanding concrete hydration processes in their early stages, contributing to improved construction practices and structural durability.

Saravanan et al. (2015) evaluating the electromechanical impedance (EMI) signatures of five smart aggregates embedded in a concrete cube. The cubes were subjected to compressive loads until failure, and the EMI was monitored during the progressive strength loss. Furthermore, the effectiveness of this approach was confirmed by evaluating the performance of conventional smart aggregates on a larger concrete beam. The study included an extensive computational analysis, incorporating a three-peak admittance curve with parameter adjustments for stiffness, damping, and straightforward scaling. Various statistical metrics were examined, such as root mean square deviation (RMSD), mean absolute percentage deviation (MAPD), cross-correlation (CC), modified cross-correlation (MCC), and the rate of change of RMSD. The differences between the reference and changed states were investigated. Progressive C-S-H gel formation caused variations in frequency and amplitude peaks in the smart aggregates, which demonstrated both stiffness and mass increment.

Saravanan et al. (2017) studied the two smart aggregates embedded in concrete cubes were thoroughly examined to assess their effectiveness in evaluating strength gain during the initial curing period, using electromechanical impedance (EMI) signatures. A notable contribution of this research involves the introduction of an innovative multisensor configuration, connected both serially and in parallel, comprising a cluster of lead zirconate titanate (PZT) sensors. This configuration enhances the ability to monitor early-stage characteristics and later-stage strength development in extensive sensor deployment scenarios. The research also established a relationship between root-mean-square deviation (RMSD) and strength parameters, potentially serving as a valuable tool for characterizing strength gain. Additionally, the research conducted experimental investigations on PZT-bonded concrete shear walls to investigate variations in EMI signatures under conditions of crack opening. Furthermore, experimental investigations were carried out on PZT-bonded metal structures to assess changes in modal density characteristics and the influence of low-frequency vibrations on the resultant EMI signatures.

2.10 Dynamic Strain Measurement Using Pzt Sensors

Materials with piezoelectric properties PZT can sense changes in its environment, such as changes in geometry, mechanical or electrical properties, and respond quickly, which can be easily measured. The PZT operates under the effect of piezoelectricity, which can convert electrical responses into mechanical disturbances and mechanical disturbances into electric pulses. These effects are represented mathematically, with Equation 2.6 demonstrating the sensing behaviour of the PZT and Equation 2.7 demonstrating the actuation behaviour. One dimensional interaction between PZT Patch and the host structure is shown in Figure 2. 12.

$$D_3 = \overline{\varepsilon_{33}^{T}} E_3 + d_{31} T_1 \tag{2.6}$$

$$S_1 = \frac{T_1}{Y^E} + d_{31} E_3 \tag{2.7}$$

Where S_1 represents the strain value in direction ‘1’. D_3 is the electric displacement over the PZT patch, the piezoelectric strain coefficient is d_{31}, E_3 is the external electric field and T_1 is the axial stress in direction ‘1’. $\overline{Y^E}$ is the complex Young’s modulus of elasticity of the PZT patch at a constant electric field as shown in Equation 2.8

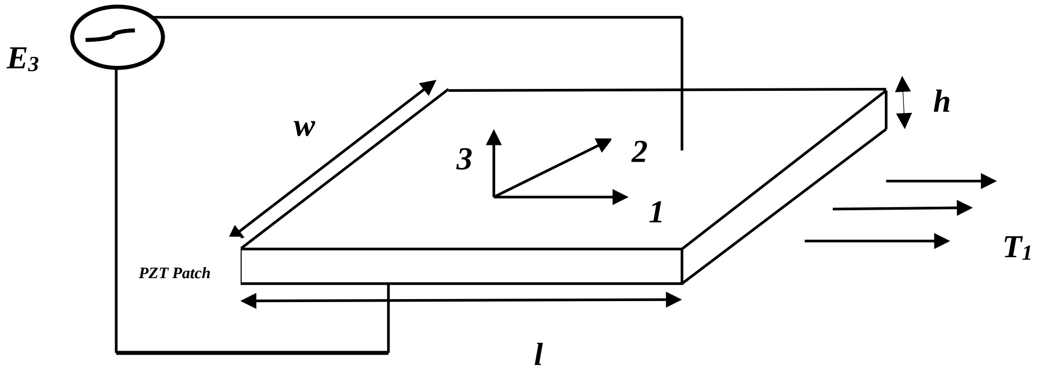

Figure 2. 12 One Dimensional interaction of PZT patch under the action of electric field and stress

$$\overline{Y^E} = Y^E\,(1 + \eta i) \qquad \textbf{(2.8)}$$

$\overline{\varepsilon_{33}^T}$ is the complex electric permittivity in direction ‘3’ at constant stress as shown in Equation 2.9

$$\overline{\varepsilon_{33}^T} = \varepsilon_{33}^T(1 - \delta i) \text{ with } i = \sqrt{-1} \qquad \textbf{(2.9)}$$

Where η and δ represent the mechanical loss factor and the dielectric loss tangent respectively. As shown in Equation 2.10, Shankar (2010) developed a relationship between the voltage across the PZT patch and strain in the host structure at the point of attachment.

$$V = \left(\frac{d_{31}\,\overline{Y^E}h}{\overline{\varepsilon_{33}^T}}\right)S_1 \qquad \textbf{(2.10)}$$

Where V represents the voltage generated across the PZT patch of the thickness h. The output voltage can be measured using the instrument oscilloscope and with the help of this measured voltage, strain induced can be calculated using this equation.

Dixit and Bhalla (2018) studied the concrete specimens of grade M-25, including 150 mm cubes and 100 × 200 mm cylinders, were examined. These specimens were fitted with embedded concrete vibration sensors (CVS). To replicate impact loading conditions, a 5 kg iron ball was released from different heights, namely 2 m, 2.5 m, and 3 m above the top surface of the test cubes. During the impact tests, researchers gathered both strain data and admittance signatures.

The outcomes from the impact tests indicated an escalation in the maximum strain levels observed in the specimens with an increasing number of impacts.

In their research Negi et al. (2019), an examination was conducted on a concrete slab subjected to impact loading, utilizing a multi-based piezo configuration. Voltage-time histories for each impact at all the sensors were accurately recorded using a digital oscilloscope with a sampling interval of 2 ms. The findings indicated that as the level of damage at the center increased, there was a decrease in the strain transferred from the impact point to the sensor location, and this decrease was more pronounced with an increasing number of impacts.

2.11 Finite Element Analysis (FEM) Of Concrete Structures under Temperature and Impact Loading

FEM analysis has emerged as a superior technique for analyzing concrete structures in recent years because of its accurate interpretation and faster results. Due to these advantages, most researchers now employ the FEM technique to analyze concrete structures subjected to impact loading, thermal loading, and the combined effect of impact and thermal.

Researchers have demonstrated that FEM analysis produces significant results when analyzing concrete under thermal loading conditions (Berg et al. 1973)(Rafi et al. 2008).

Bhuvaneshwari and Mohan (2020) investigated the strengthening effect of glass fibre and polypropylene fibre-based engineered cementitious composites (GFPPECC) on fire-damaged reinforced concrete short exterior columns. The FEM analysis performed by ANSYS, FEM results was compared with the experimental results and found that there was no deviation in both the experimental and numerical results.

Song et al. (2018) simulated the mass concrete freezing shaft lining and frozen soil wall under the influence of low temperatures. The ANSYS finite element software was used to perform the transient heat transfer analysis.

Hawileh and Naser (2012) investigated the thermal stress analysis of a reinforced RC beam with GFRP bars. The ANSYS transient thermal-stress finite element analysis was used to analyze the heat transfer and mechanical behaviour of the RC beam. It was demonstrated that the FE-predicted temperature and mid-span deflection results agree well with the measured experimental data.

Ganesan and Venkata Sai Kumar (2019) used ANSYS explicit dynamics software to perform FEM analysis of the RC and pre-stressed RC slab at low-velocity impact under two different boundary conditions, the opposite side simply supported and the adjacent side simply supported. Their analysis demonstrated that the boundary condition significantly impacted the slab's deflection.

Anil et al. (2015) performed the FEM analysis of the RC slab under the low velocity of impact for various boundary conditions, and they discovered that the FEM results provide better ideas of the slab's impact capacity for the design period.

The FEM behaviour of a concrete structure subjected to thermal loading was thoroughly discussed before being loaded by impact loading. Ožbolt et al. (2019) has been performed the three-dimensional finite element analysis of the RC slab in two steps, in the first stage, damaged by fire and then in the 2nd stage impact load was applied. Transient 3D FE thermo-mechanical analysis was used to simulate the fire effect, while explicit multi-body dynamic analysis was used to simulate the impact loading; according to the results of the study, the simulation can replicate the experimental results.

Jin et al. (2018a) investigated the effect of elevated temperature on dynamic compressive properties of heterogeneous concrete using a mesoscale numerical study. They divided the study into two steps, first simulating heat conduction behaviour and then simulating the dynamic mechanical behaviour of concrete using the first stage's output as the initial conditions.

Ožbolt et al. (2020), performed a numerical simulation on thermally pre-damaged reinforced concrete frames under impact loading in two stages. The RC frame was initially subjected to fire exposure for pre-damage, followed by the application of an impact load from the side using a steel pendulum. The simulation results indicate that pre-damaging the RC frame through fire exposure substantially reduces its resistance and alters its response.

2.12 Gaps Identified In Previous Research

The identified literature gaps are presented as follows, based on the literature review.

- Nearly all the studies have focused on the individual effect of temperature and impact so combined prediction is beneficial for structures under damage.
- The best suitable sensor configuration is still not clear under the combined effect impact and elevated temperature.
- Most of the studies have done numerical modelling on temperature or only on impact, so needs to be further focused on numerical modelling of structures and piezo sensors under the combined effect of temperature and impact.

Chapter 3: EXPERIMENTAL INVESTIGATION ON CONCRETE CUBE SPECIMEN

3.1 Introduction

Chapter 3 delves into the practical implementation and experimental investigation of the proposed monitoring technique using different sensors configuration in concrete structures. Building upon the theoretical framework and literature review presented in the previous chapters, this chapter aims to validate the effectiveness and reliability of the electromechanical impedance (EMI) based approach for monitoring concrete properties and behaviour. In this chapter, the detailed setup of the experimental tests conducted on concrete specimens, each equipped with PZT sensors have been discussed. The specimens were subjected to various impact and temperature loading conditions and environmental factors, simulating real-life scenarios to assess the performance and capabilities of the proposed monitoring system. The experimental investigation includes the detection of potential damage or structural changes of concrete under the individual effect of impact and temperature and also the combined effect of impact and temperature. By using the EMI techniques, signatures obtained from the PZT sensors were analysed in the form of conductance and susceptance parameters. These obtained signatures were further analysed by using different parameters such as statistical techniques, peak conductance and resonant frequency. Furthermore, to establish correlations between these signatures and the concrete mechanical properties are establish using the equivalent based parameters such as mass, stiffness and damping. Furthermore, the remaining life was estimated based on the stiffness value. Additionally, this chapter explores the practical challenges faced during the implementation of the monitoring technique, such as signal processing, data interpretation, and calibration procedures. The results obtained from the experiments are critically analysed, and the efficacy of the proposed approach is thoroughly evaluated. Overall, Chapter 3 serves as a crucial component in validating the proposed EMI-based monitoring method and provides valuable insights into the feasibility and potential applications of the best suitable sensor configuration in concrete structures. The outcomes of this experimental investigation will contribute significantly to the advancement of non-destructive evaluation techniques for concrete health monitoring and structural assessment.

3.2 Preparation of Concrete Cube Specimen

In this investigative study, 75 concrete cubes of grade M30 (As per IS 456: 2000), 150 x 150 x 150 mm, were cast using the mix design ratio 1:1.78:3.315 (C: FA: CA). The concrete cube specimen was cast using ordinary Portland cement (OPC) of grade 43 with the fine aggregate of the grade of Zone 1 (as per Table 4, IS 383, 1970) with the 20 mm maximum nominal size of aggregate, angular in shape and the PCE (Polycarboxylic Ester) based AURAMIX 400 admixture. The detailed composition of the concrete mix has shown in Table 3. 1. The standard size of moulds was filled in three layers with the proper compaction using a vibrating table and proper precautions were taken in pouring the concrete to avoid damage to the JKTPS type piezo sensors.

Table 3. 1 Detailed composition of concrete mix

Parameters	**Units**	**Quantity**
Cement(OPC of grade 43)	kg/m^3	372.5
Coarse aggregate	kg/m^3	1235
Fine aggregate	kg/m^3	665.7
Water cement ratio	-	0.4
Slump	mm	50
Superplasticizer	kg/m^3	7

All the prepared samples are placed in a water tank for 28 days of curing and after the curing is completed, all samples are placed in the laboratory in the ambient environment till the concrete sample is tested. Figure 3. 1 shows all the concrete cube specimens that were cast in the laboratory.

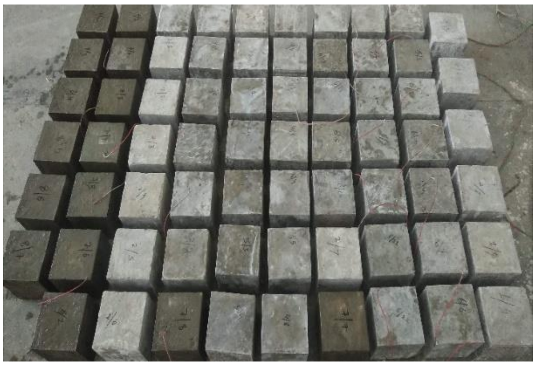

Figure 3. 1 All the concrete cube specimen cast in the laboratory

3.3 Fabrication of Sensors

In this study, three different types of piezo sensors were used name as embedded, surface bonded and non-bonded were fabricated. The PZT patch of thickness 10 X 10 X 0.2 mm was used in the fabrication of all these sensors. Table 3. 2 presents a detailed breakdown of the material parameters for the PZT patch, sourced directly from Central Electronics Limited, Ghaziabad.

Table 3. 2 Material Properties of PZT

Material parameters Piezoelectric	**Value**
Piezoelectric charge coefficient d_{33}(10^{-12} C/N)	500
Piezoelectric voltage constants (g_{33},10^{23} Vm/N)	21.2
Young’s modulus YE^{33} (10^{10} N/m)	5.0
Mechanical quality factor Q_m	76
Curie temp (^{o}C)	240
Density (10^3 kg/m^3)	7400
Dielectric constant	2500
Poisson’s ratio	0.35
Dissipation factor at 1KHz	0.02

3.3.1 Embedded Sensors

The embedded sensors in the form of jacketed piezo sensors (JKTPS) is shown in Figure 3. 2. The JKTPS of diameter of 25 mm and height 20 mm was fabricated by using rectangular PZT patches of size 10 × 10 × 0.2 mm which is placed at the centre and the epoxy resin provided at the top and bottom portion for covering the PZT to protect them from the impacts of water and ambient conditions during the construction stages.

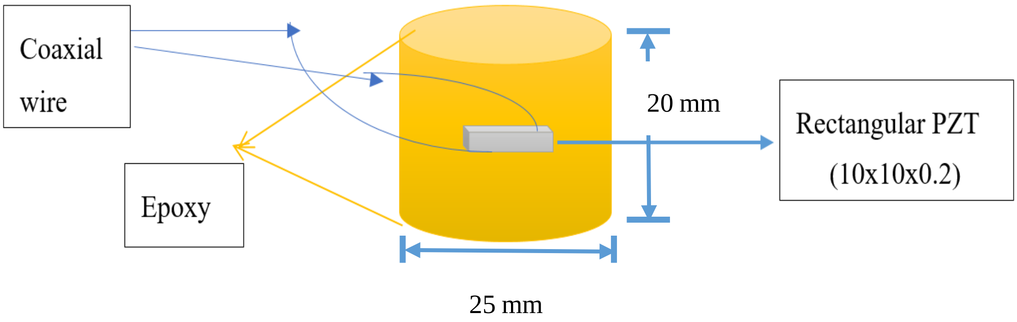

Figure 3. 2 Jacketed piezo sensors (JKTPS) with PZT patch of size 10 x 10 x 0.2

JKTPS are made in a step-by-step process as shown in Figure 3. 3, in which a cap is first half-filled with epoxy, then the PZT is placed, and the cap is filled with epoxy and left out for 24 h for the epoxy to set.

3.3.2 Surface Bonded Sensors

Surface bonded (SBPS) sensors, as shown in Figure 3. 4 were directly bonded on the concrete using epoxy at the center on the side face of the concrete adjacent to the impactor face, and the upper face of the bonded PZT was again covered with epoxy to protect it from the environment.

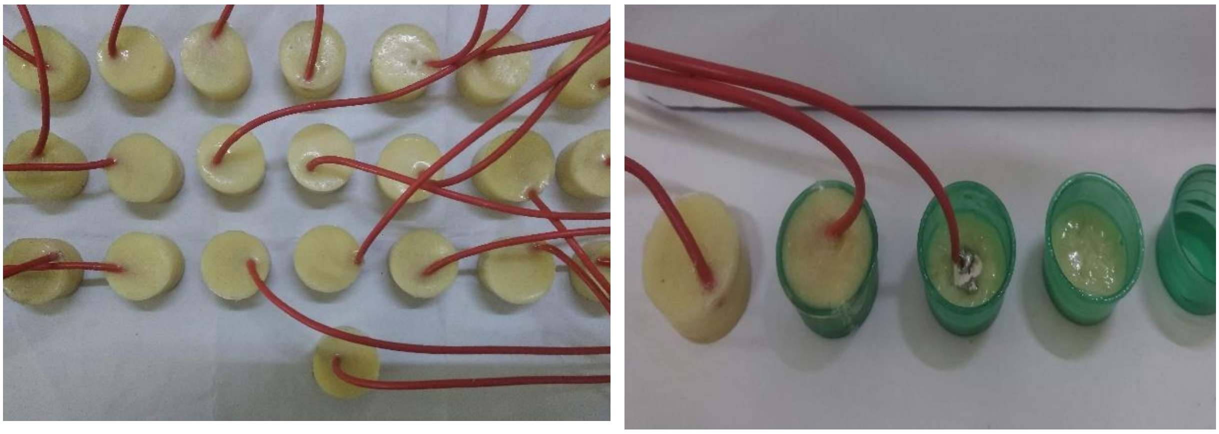

(a) (b)

Figure 3. 3 JKTPS sensors a) all fabricated sensors in the laboratory (b) step-by-step fabrication process of JKTPS sensors

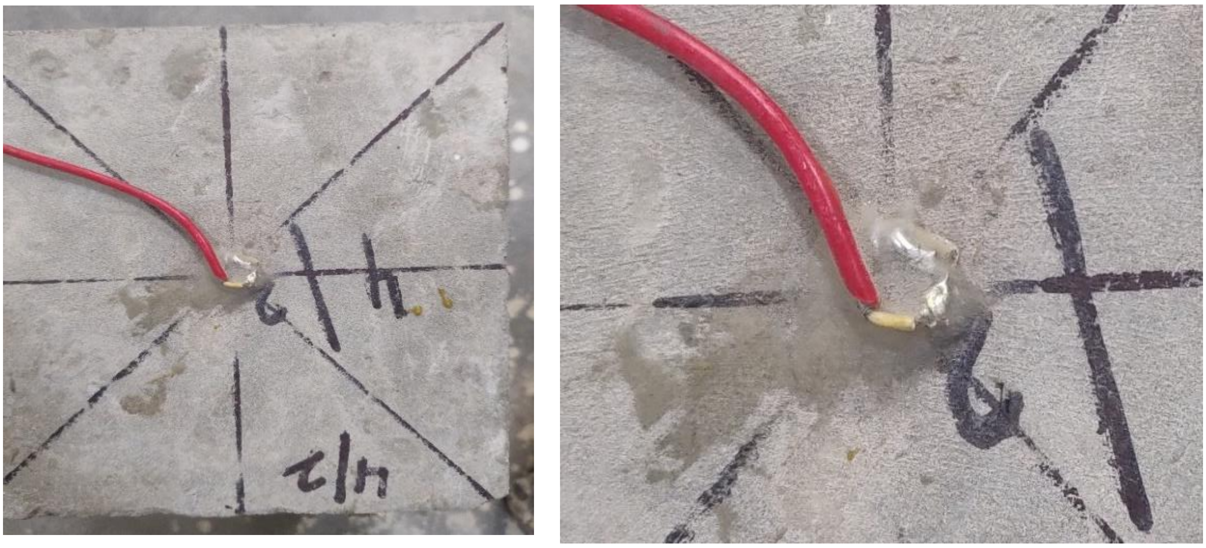

Figure 3. 4 Surface bonded sensors bonded on concrete

3.3.3 Non Bonded Sensors

The fabrication of the non-bonded piezo sensors (NBPS) was accomplished by using an aluminium strip (100 x 10 x 1 mm) that had been surface cleaned and a PZT patch (10 mm x 10 mm x 0.2 mm) was fixed in the middle of the aluminium strip as shown in Figure 3. 5. For the bonding of the aluminium sheet and PZT, Epoxy was used as a binding material, and special care was taken to ensure that they were properly bonded. If the bond layer is not adequately accounted for in the EMI approach, it can have a considerable impact on the signal transmission from the PZT material. The PZT sensor generates a permanent finite-thickness interfacial layer between the structure and the patch when it is glued to it with an adhesive mix (such as epoxy).

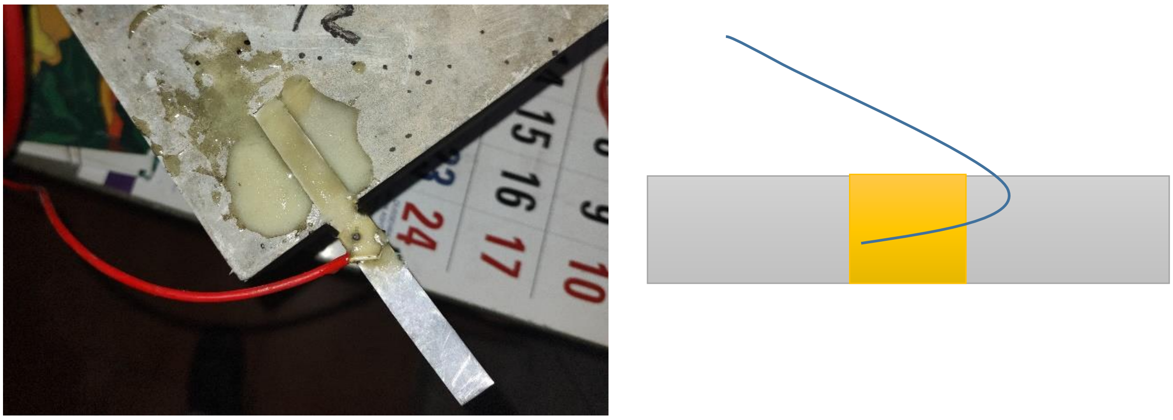

Figure 3. 5 Fabrication of NBPS sensors using the aluminium strip

3.4 Installation of Different Sensors Configuration

As described in the preceding section, three different piezo sensors configurations were made and concrete cubes are attached with these three distinct piezo sensor configurations, embedded (JKTPS), Surface bonded (SBPS) and non-bonded (NBPS) as shown in Figure 3. 6. JKTPS are placed at the centre of the concrete cubes at the time of casting considering equal distance from the top and bottom. SBPS is directly attached to the concrete with the help of epoxy and NBPS is indirectly attached to the concrete, first PZT patch was placed at the centre of the aluminium sheet and the aluminium sheet was bonded with the concrete cube using the epoxy.

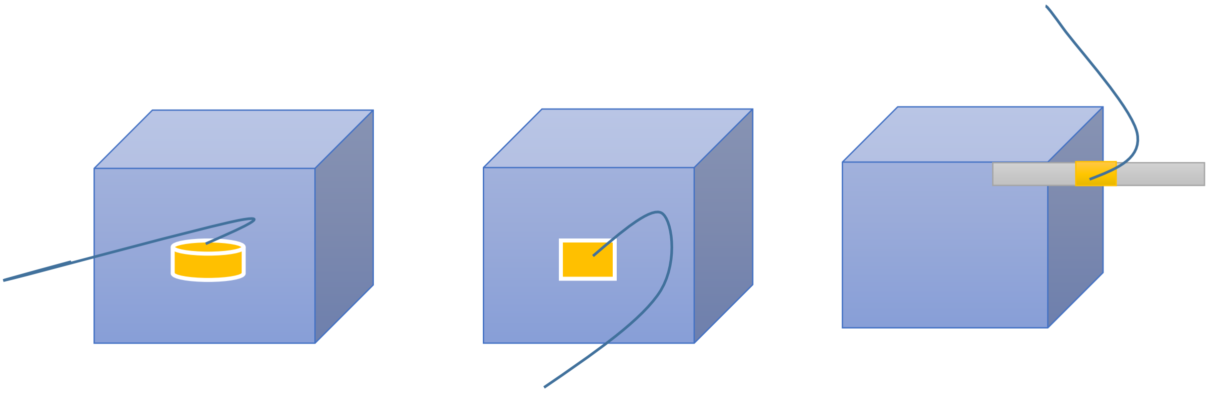

Figure 3. 6 placing of different sensors through host structure a) JKTPS b) SBPS c) NBPS

3.5 Experimental Setup

The whole experimental setup with the guided tube for impact tests is shown in Figure 3. 7. A 5.45 kg cast iron ball, as depicted in Figure 3. 8, was released from heights of 3 and 3.5 meters onto the concrete cubes positioned on the cemented floor, as illustrated in Figure 3. 9. To provide guidance, a 4 mm thick PVC (Polyvinyl chloride) pipe with a 150 mm internal diameter, as shown in Figure 3. 10, was securely attached to the roof parapet wall. The purpose of the guided tube is only that, at each impact, the steel ball was able to hit precisely at the top of the cube. The rectangular oven of W 610 x D 610 x H 1016 mm as shown in Figure 3. 11 were used for heating the concrete cube provided by WIDSONS Instruments Pvt. Ltd. having a maximum heating temperature limit is up to 1200^{o}C.

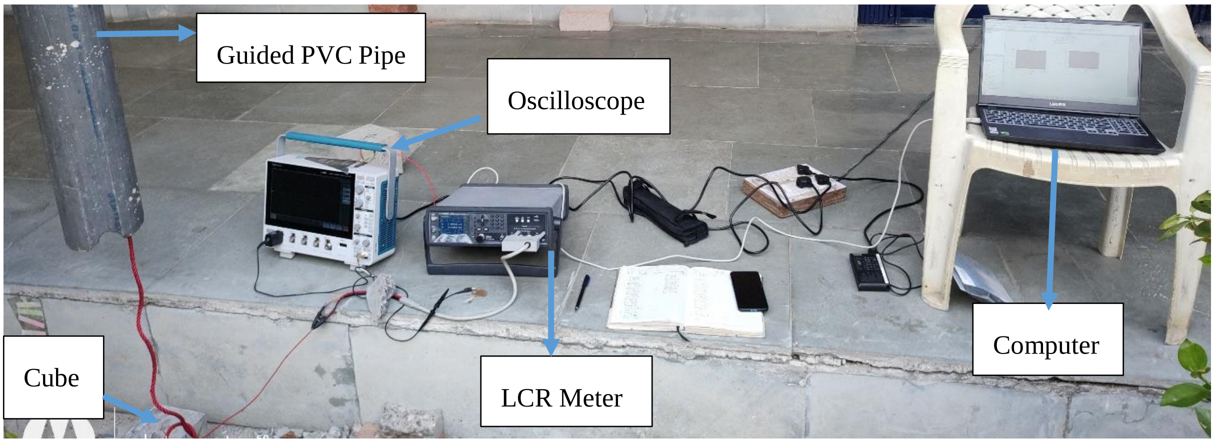

Figure 3. 7 Complete Experimental Setup for impact loading

Figure 3. 8 Ball Impactor

Figure 3. 9 Specimen placed on the surface

Figure 3. 10 Guided pipe

Figure 3. 11 Rectangular Furnace

3.6 Experimental Details and Procedure

In the experimental study, the damage was detected in the reference of baseline data, before testing the cube, baseline data were collected from the different sensors configuration from each cube in the form of *G vs F* and *S vs F*. First, admittance signatures for the cubes were obtained as a baseline signature from all of the different sensors and then cube was then subjected to three different temperatures, ranging from 50 °C, 100 °C and 150 °C. Cubes were heated in the oven for 120 minutes and then cooled for 60 minutes at room temperature. The complete methodology used in this study is shown in Figure 3. 12. It begins with the fabrication of the three different sensors, their installation on the concrete cube under the application of temperature and impact loading, and subsequent analysis and monitoring of the analysis of the raw signature data using various parameters to determine the best sensor configuration for the remaining study.

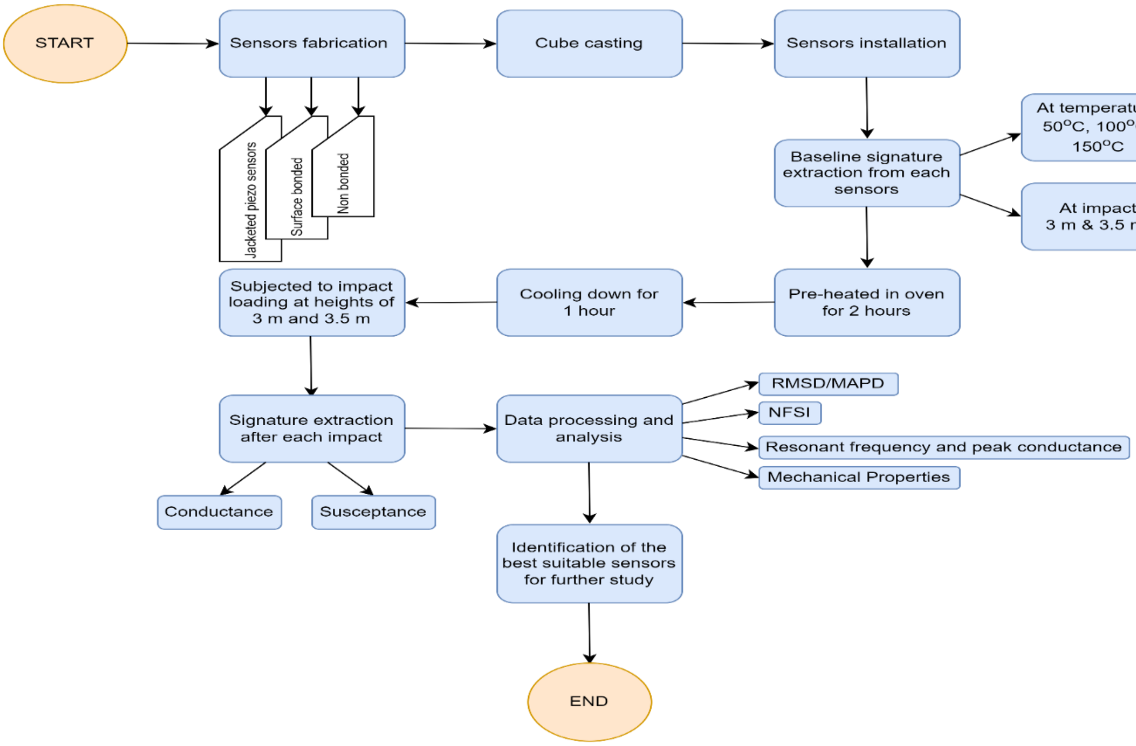

Figure 3. 12 Methodology adopted in the study

To begin, baseline data were collected for all three different sensor configurations in the form of conductance *(G)* in the function of frequency *(F)* and susceptance *(S)* in the function of frequency *(F)* plots in the 50 kHz to 600 kHz frequency ranges. PZT typically has an exciting range of 30 to 600 kHz as recommended by (Park et al. 2003)(Sun et al. 1995), as the frequencies higher than the 500 kHz are found to be unfavourable because they make the sensing region of the PZT patch too small. The *G* and *B* signatures are acquired using Keysight precision LCR meter E49800A, which has a frequency range of 20 Hz to 2 MHz (Keysight (Agilent) Technologies 2014). Keysight's VEE Pro software was used to control the frequency step. By applying 1 V of voltage across the terminals of the PZT patch, all signatures were recorded at the 100 Hz frequency step after that, the cube was subjected to three different temperatures, ranging from 50 °C, 100 °C and 150 °C. Cubes were heated at a rate of 2 °/s for 120 minutes and then cooled at room temperature for 60 minutes. Signatures are taken for both conditions, i.e. immediately after heating and after 60 minutes cooling down at room temperature. Furthermore, cooled cube samples were tested at two different impact heights, 3 and 3.5 m, and signatures were recorded after each impact up to failure. The impactor's velocity and energy absorption were calculated using Equations 3.1 and 3.2 based on the height of the fall, number of impacts, and mass of the ball.

$$v=\sqrt{2gh} \qquad \textbf{(3.1)}$$

$$E=n*m*g*h \qquad \textbf{(3.2)}$$

Where n is the number of impacts, m is the mass of the ball, h is the height of the ball, and g is the gravity acceleration. The features of the specimens, under the height of 3 m falls, velocity and energy absorption for different numbers of impacts are summarized in Table 3. 3. Figure 3. 14 shows the block diagram of the concrete cube with the impactor.

Table 3. 3 Features of the specimen under the 3 m height of impact, velocity and energy absorption

No. of Impacts	1	2	3	4	5	6	7	8	9	10	11
Height of Fall *(m)*	3	3	3	3	3	3	3	3	3	3	3
Velocity*(m/s)*	7.6	7.6	7.6	7.6	7.6	7.6	7.6	7.6	7.6	7.6	7.6
Energy absorption*(J)*	160.3	320.7	481.1	641.5	801.9	962.3	1122.7	1283.1	1443.5	1603.9	1764.3

The variation of the height of fall and velocity of the impactor with energy absorption. Form Figure 3. 13, clearly shows that the energy absorption capacity of a concrete cube increases with the increase in height of fall and velocity of the impactor.

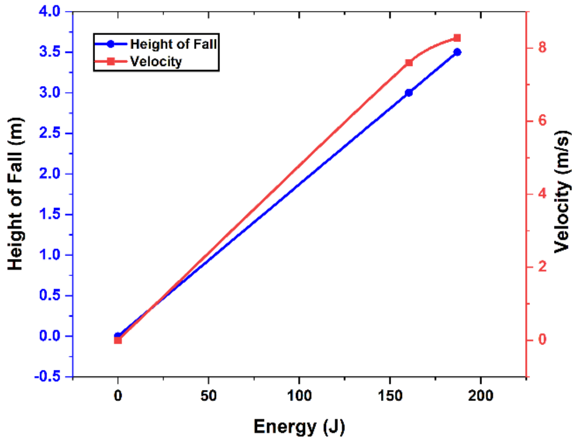

Figure 3. 13 Variation of the height of fall and velocity vs energy consumption

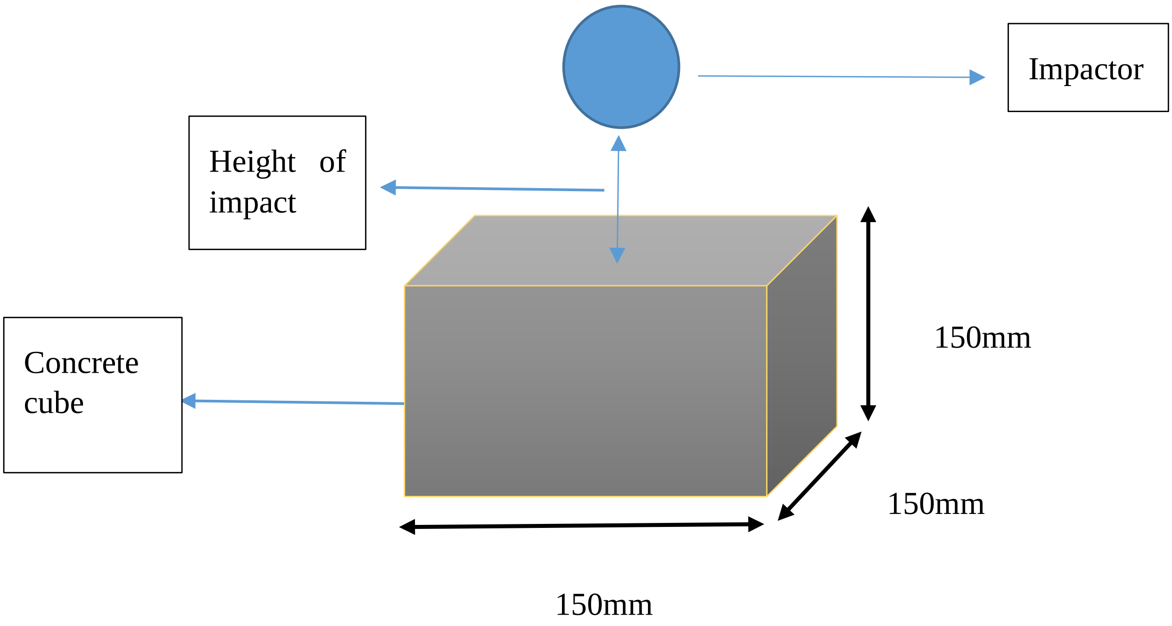

Figure 3. 14 Concrete cube with the steel ball impactor

3.7 Quantification of Impact Load Using Voltage-Time History

In general, the time histories of impact loads exhibit very small variations, making it challenging to discern distinct loading characteristics. A high acquisition rate digital oscilloscope was used to solve this problem (model Tektronix TBS 2104B series), which captured the impact value for intervals as short as 1 µs. The voltage generated by the PZT patch attached to the host structure was essentially captured by the oscilloscope. Voltage measurements were taken at a high acquisition rate, with acquisition times ranging from 500 ms to 2 s. The voltage-time histories were meticulously analysed to establish a correlation between accumulating damage and strain.

A total of 24 sensors were used to determine the effect of voltage with the impact loading under temperature variation for different sensors configuration. Absolute peak voltage (V_p) was identified for each impact loading. Furthermore, this obtained V_p were used to calculate the accumulated value of strain for each sensor in further studies. Figure 3. 15 shows a typical variation of the voltage vs time graph for four different cube conditions. Figure 3. 15 (a) depicts the voltage variation for cube S1a following the second impact, in which the voltage value first increases to 0.104 V and then decreases to 0.080 V. The graph in Figure 3. 15 (b) shows the same pattern as the previous one, which depicts the voltage vs time graph for cube no. J1a after the second impact. Figure 3. 15 (c) and (d) depict the voltage variation for cube no. J4d and J4 after the 3rd and 2nd impact respectively for JKTPS sensors at the temperature variation of 150 ^{o}C, in both of them the voltage value first decreased then increased.

Quantification of impact force is represented with the help of obtained peak voltage from each sensor at the time of impact and it was found that the peak voltage follows a continuously decreasing trend for the surface bonded and non-bonded sensors with the increase in the number of impact loads on each cube. This decreasing trend of peak voltage is due to the increase in damping of the cube. Peak voltage has followed the opposite trend for the JKTPS because they have been placed in the line of impact loading as a result strain development is more in this case. Table 3. 4 displays all of the typical 24 cubes, which include the representation number, number of impacts up to failure and *Vp* value. Furthermore, strain values were calculated using Equation 3.3 with the help of PZT parameters and *Vp* value.

$$\mathrm{S_p} = \frac{\varepsilon_{33}^{\mathrm{T}}}{\mathrm{d_{33} h Y^E}} \mathrm{V_p} \qquad \textbf{(3.3)}$$

Table 3.4 depicts the Vp value for each cube, which is the maximum voltage recorded against the impact loading. The maximum absolute voltage value (Vp) recorded for the JKTPS sensors was 17.11 V, and this occurred under an impact height of 3 m at 100°C. This observation can be attributed to the positioning of JKTPS sensors in the direct path of the impact. Furthermore, after the first impact, the peak voltage and strain value of each PZT installed in the cube were calculated as shown in Table 3. 5. The maximum voltage under the JKTPA sensors for cube number J2b was found to be 13.398 V under the first impact.

Due to an inconsistent record of the voltage data, the study of voltage-time history for the cube numbers N1a, N2b, S1a and J3c was not analyzed; therefore, the total remaining 20 typical samples were analyzed for the strain value against the first impact.

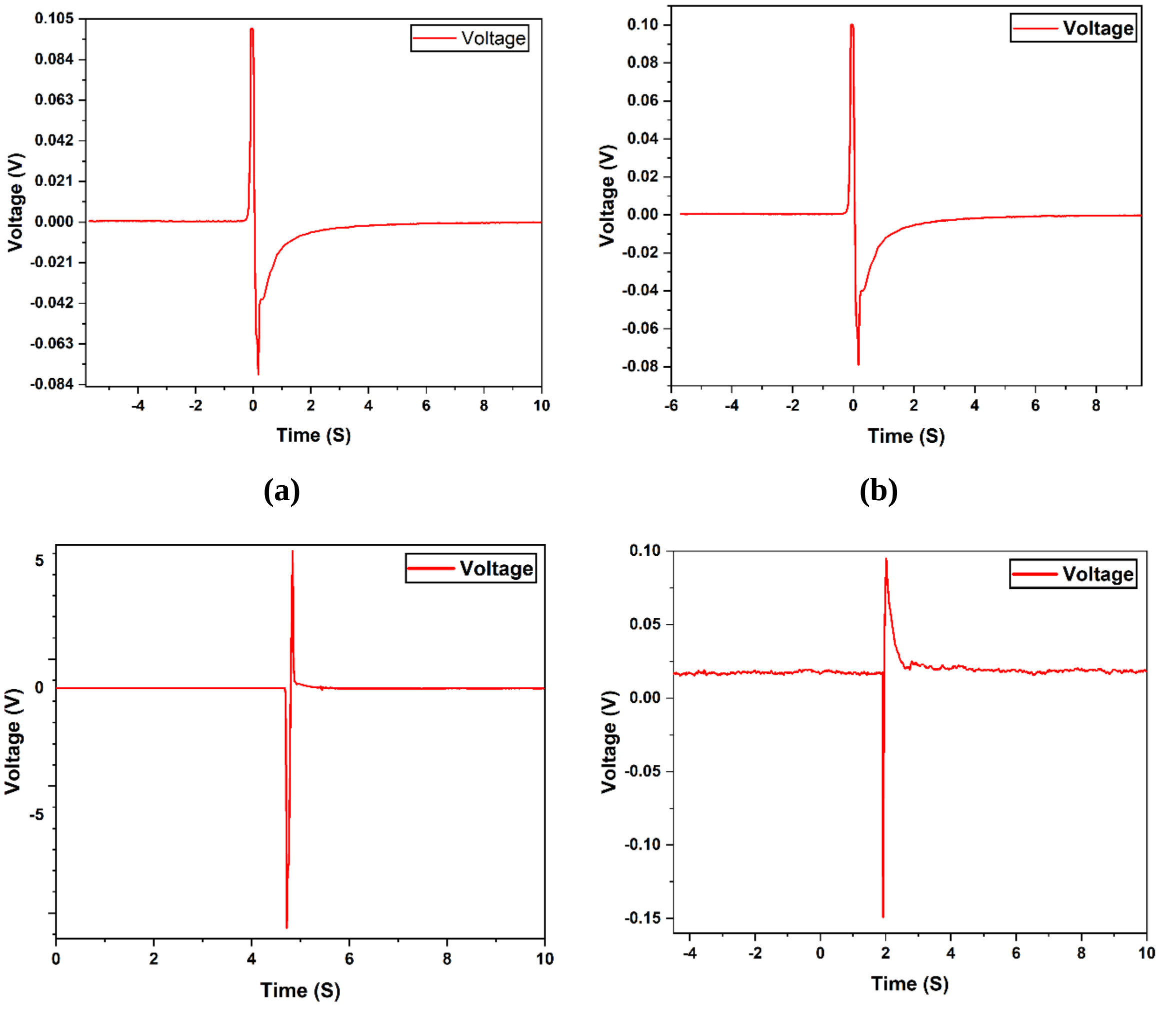

(a) (b)

(c) (d)

Figure 3. 15 Typical voltage time history for sensors a) height of 3m at ambient temperature for SBPS b) height of 3m at ambient temperature for JKTPS c) height of 3.5 m at 150 ºC temperature for JKTPS sensors d) height of 3 m at 150 ºC temperature for JKTPS

Table 3. 4 Representation of cube number, Absolute peak voltage (Vp) value and strain value for all different sensors with varying impact and temperature condition

S.No.	Type of Sensors	Impact Height	Temperature	Cube representation Number.	Total number of impact	Absolute Peak Voltage (V_p)
1	Non-Bonded PZT (NBPS)	3m	Ambient	N1	11	0.78
			50ºC	N2	11	0.33
			100ºC	N3	9	2.42
			150ºC	N4	7	10.58
		3.5m	Ambient	N1a	8	---
			50ºC	N2b	7	----

			100°C	N3c	5	2.41
			150°C	N4d	3	3.75
2	Embedded (JKTPS)	3m	Ambient	J1	7	0.10
			50°C	J2	6	3.01
			100°C	J3	7	17.11
			150°C	J4	10	2.50
		3.5m	Ambient	J1a	7	0.100
			50°C	J2b	6	13.39
			100°C	J3c	6	---
			150°C	J4d	5	3.97
3	Surface Bonded (SBPS)	3m	Ambient	S1	8	0.100
			50°C	S2	8	10.58
			100°C	S3	7	11.71
			150°C	S4	12	6.41
		3.5m	Ambient	S1a	6	-
			50°C	S2b	6	5.48
			100°C	S3c	5	11.58
			150°C	S4d	6	0.72

Table 3. 5 Peak voltage and strain value after the first impact

S.No.	Cube representation no.	Peak voltage after 1st impact	Strain value against 1st impact x (10^{-6})
1	N1	0.24	1.14
2	N2	0.27	1.29
3	N3	1.46	6.86
4	N4	3.32	15.61
5	N3c	0.62	2.94
6	N4d	0.38	1.80
7	J1	0.10	0.473
8	J2	1.46	6.86
9	J3	4.02	18.90
10	J4	0.69	3.27
11	J1a	0.10	0.470
12	J2b	13.39	63.01
13	J4d	3.97	18.67
14	S1	0.100	0.47
15	S2	6.41	30.18
16	S3	3.13	14.75
17	S4	6.34	29.81
18	S2b	1.40	6.62
19	S3c	9.07	42.67
20	S4d	0.51	2.43

3.8 Data Acquisition and Damage Assessment Using Emi Technique

The data acquisition has been acquired using an LCR meter. The Keysight E4980A Precision LCR meter, 20 Hz to 2 MHz (Keysight (Agilent) Technologies 2014) was used to acquire the conductance (G) and susceptance (B) data from the PZT. The frequency step used for data acquisition was 100 Hz, with a voltage of 1 V applied across the PZT patch's terminals. Each of the sensors is connected with a coaxial wire through soldering, and the other side of the coaxial wire is directly attached to the LCR meter. The V.Pro software provided by Keysight, i.e., already compatible with the LCR meter, was used for collecting the data of G in the function of f and B in the function of f. This section discusses the assessment of damage in concrete under impact loading for various temperature conditions using the EMI technique, as well as the effect of temperature on concrete in detail.

3.8.1 Extraction of Baseline Data

Baseline data were collected for all three different sensor configurations in the form of conductance (G) in the function of frequency (F) and susceptance (S) in the function of frequency (F) plots in the 50 kHz to 600 kHz frequency ranges. Figure 3. 16 shows a baseline conductance signature of different sensors configuration JKTPS, SBPS, and NBPS for 3m height of impact at ambient temperature.

Because of their different sensing capabilities, each sensor has a unique conductance signature. SBPS sensors have achieved their first peak between 300 kHz and 375 kHz. JKTPS obtained its first peak between 150 and 225 kHz. The first peak of the NBPS was obtained in the frequency range of 100-150 kHz, but the optimum sharp peak with a high amplitude was obtained in the frequency range of 175-275 kHz. All of this is due to the sensors' varying sensing behaviour. Figure 3. 17 depicts a baseline susceptance signature of the various sensor configurations at ambient temperature for a 3 m height impact loading. All of the sensors recorded flat signatures in comparison to conductance signatures because they are less sensitive to mechanical and environmental changes. They are only sensitive to PZT sensors, as well as PZT debonding from the host structure and loose connections.

3.8.2 Damage Assessment of Concrete under Impact Load Only for Different Sensors

The admittance signatures of cubes were obtained in their pristine state from all the different sensors as a baseline signature and compared to the damage state signatures. The variation in the conductance signature versus frequency with increasing damage under the impact loading at ambient temperature is plotted in Figure 3. 18 to Figure 3. 20 for various sensor configurations of JKTPS, SBPS and NBPS respectively.

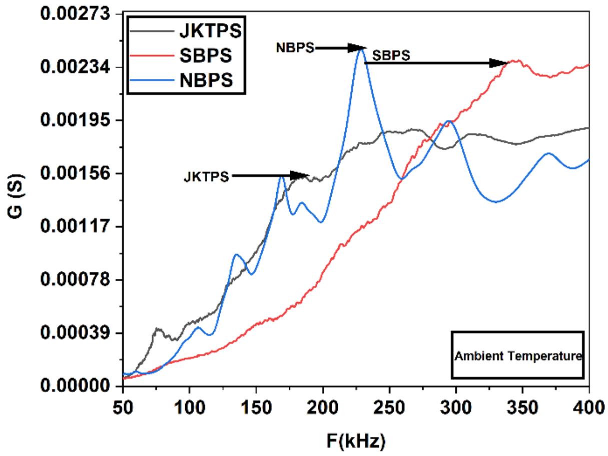

Figure 3. 16 Conductance signature of baseline data for different sensors configuration

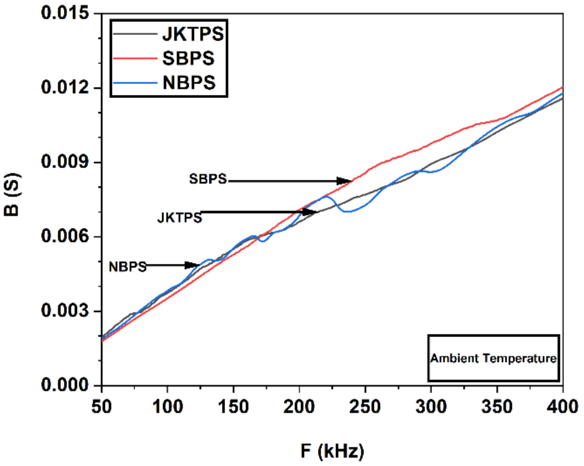

Figure 3. 17 Baseline suseptance signature for different sensors configuration

Signatures are plotted under the frequency range of 50 kHz to 600 kHz. When compared to the baseline signature and the damage state signature, the conductance signature plays an important role in assessing structural damage. Changes in mass, damping, and stiffness due to the development of cracks, damage, corrosion, and other factors were calculated using the conductance signature. Susceptance signatures are used to assess the state of the PZT patch. If the PZT patch was attached to the host structure and had to be broken down or detached from the host surface throughout the experiment, the variation of the susceptance signature with increasing frequency was shown to be a downward or uneven variation. Figure 3. 19 shows a baseline conductance signature of different sensors configuration JKTPS, SBPS, and NBPS for 3m height of impact at ambient temperature.

3.8.3 Damage Assessment of Concrete under Temperature Effect Only for Different Sensors

After acquiring the signature of various sensor configurations at ambient temperature, concrete cubes are subjected to different temperature conditions of 50, 100, and 150 ^{o}C for 2 hours, then cooled for one hour, and then subjected to impact loading at a height of 3m. Figure 3. 21–Figure 3. 23 depict the temperature variation of the conductance signature for JKTPS, SBPS, and NBPS, respectively. All of the signatures were recorded after heating the cube in the oven for three distinct temperature conditions ranging from 50 to 150 ^{o}C and cooling it for one hour in an open atmosphere.

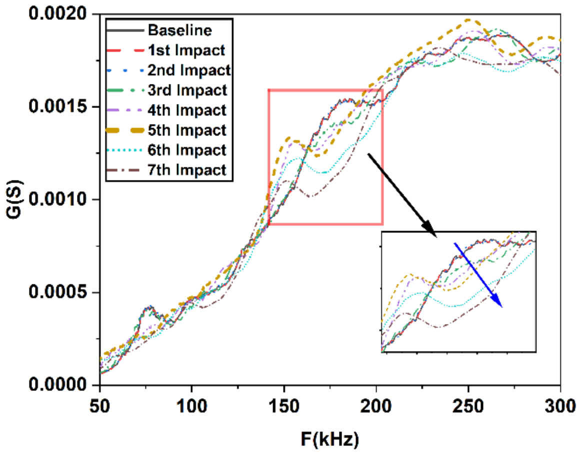

Figure 3. 18 conductance signature for JKTPS at ambient temperature

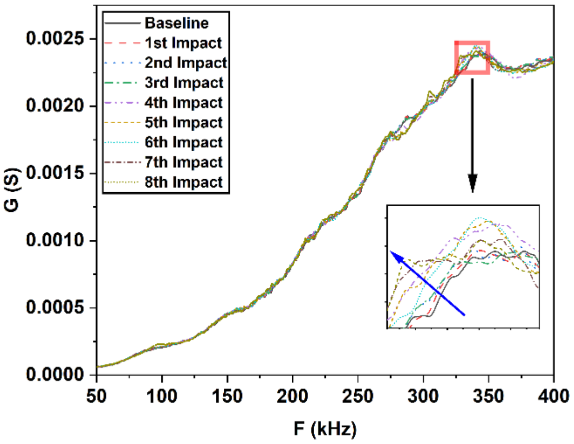

Figure 3. 19 conductance signature for SBPS at ambient ambient temperature

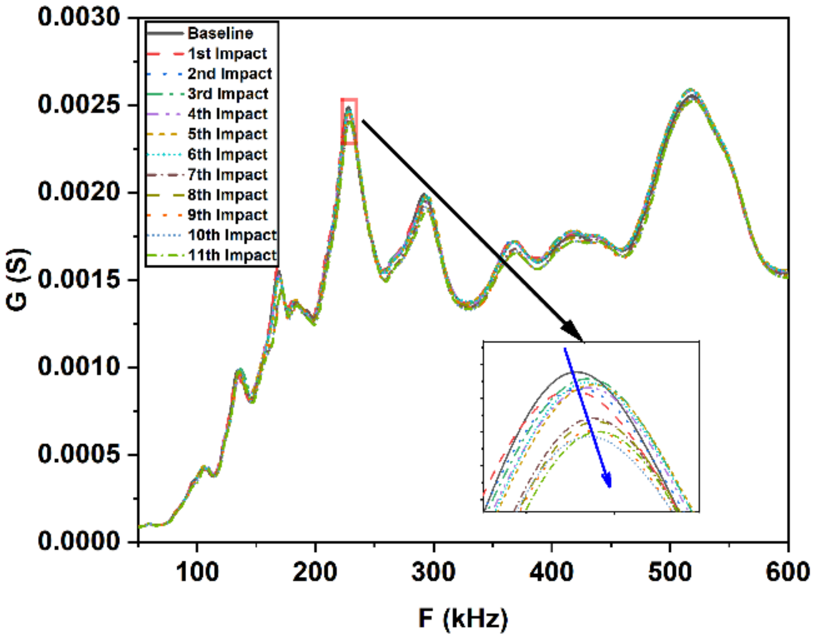

Figure 3. 20 Conductance signature for NBPS at ambient temperature

All three different sensors configuration have shown higher amplitudes of conductance as the temperatures rise. This is due to the PZT's greater sensitivity to temperature conditions. Susceptance signature graphs of all the different sensor configurations with varying temperatures from 50 ^{o}C to 150 ^{o}C are shown in Figure 3. 24 to Figure 3. 26 and all these susceptance signatures were showing similar variations against the frequency for each sensor configuration.

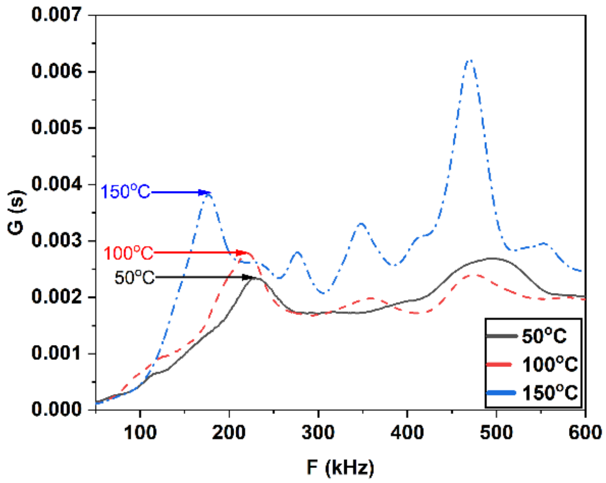

Figure 3. 21 Temperature variation of conductance signature for JKTPS sensors from 50ºC to 150ºC

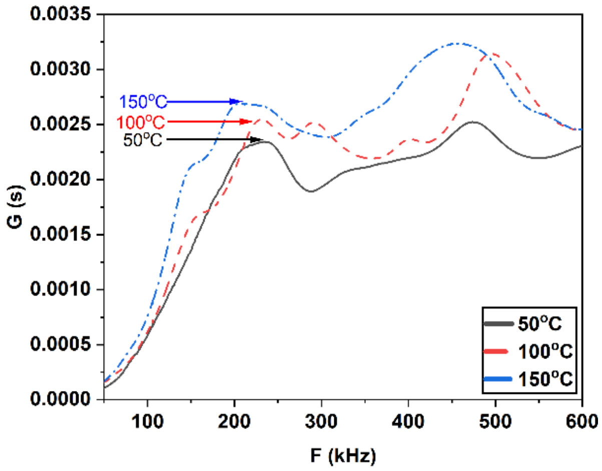

Figure 3. 22 Temperature variation of conductance signature for SBPS sensors from 50ºC to 150ºC

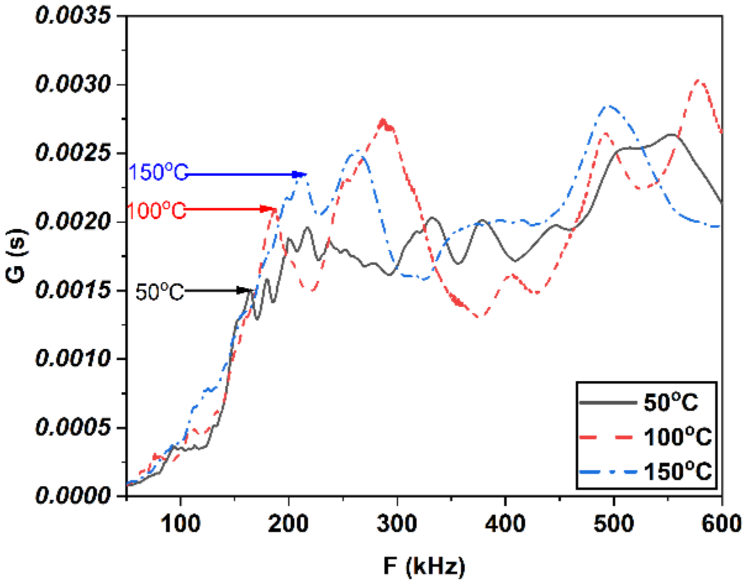

Figure 3. 23 Temperature variation of conductance signature for NBPS sensors from 50 ºC to 150 ºC

3.8.4 Damage Assessment of Concrete under the Impact Loading at Varying Temperatures Using JKTPS Sensors.

Figure 3. 27 to Figure 3. 29 depicts the graph between *G* in the function of *f* for JKTPS sensors at 3 m height of impact loading up to the failure under the three different temperature variations of 50 ºC, 100 ºC and 150 ºC. As compared to the baseline signature, for the first impact, the signature shifts upward due to temperature, and for subsequent impact loads, the signature shifts downward up to the failure as shown in Figure 3. 27, and this pattern of shifting signature is the

same for the 100 ºC and 150 ºC temperatures as shown in Figure 3. 28 and Figure 3. 29` respectively.

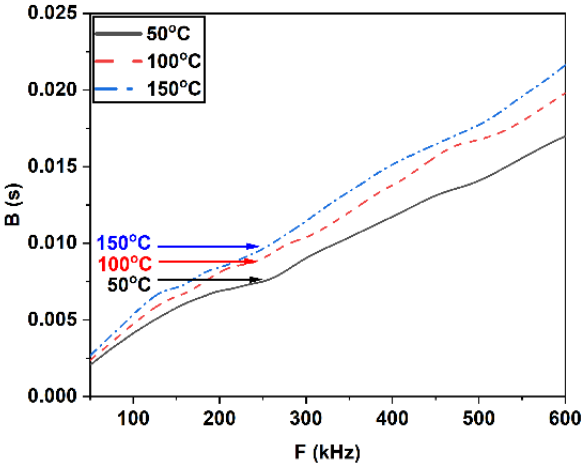

Figure 3. 24 Temperature variation of susceptance signature for JKTPS sensors from 50 ºC to 150 ºC

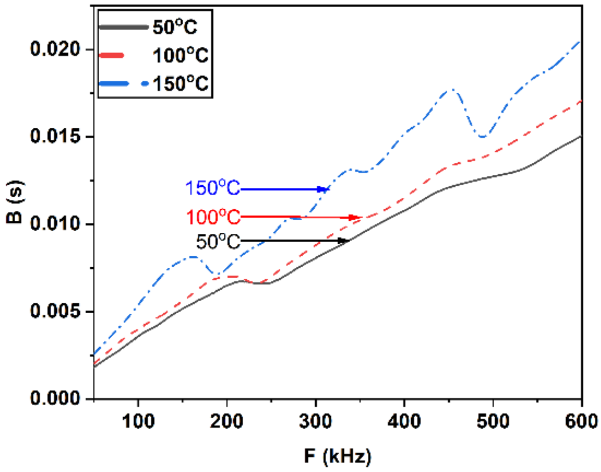

Figure 3. 25 Temperature variation of susceptance signature for SBPS sensors from 50 ºC to 150 ºC

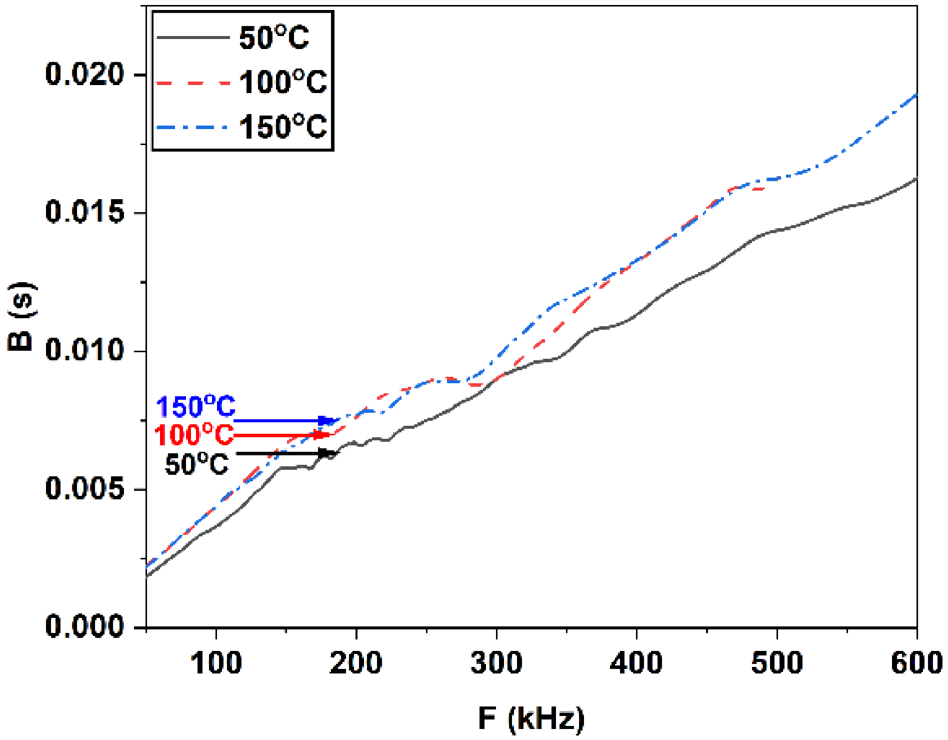

Figure 3. 26 Temperature variation of susceptance signature for NBPS sensors from 50 ºC to 150 ºC

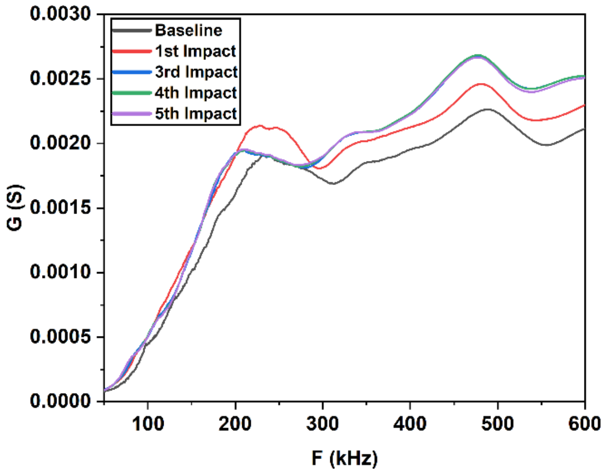

Figure 3. 27 Conductance signature for JKTPS at 50 ºC

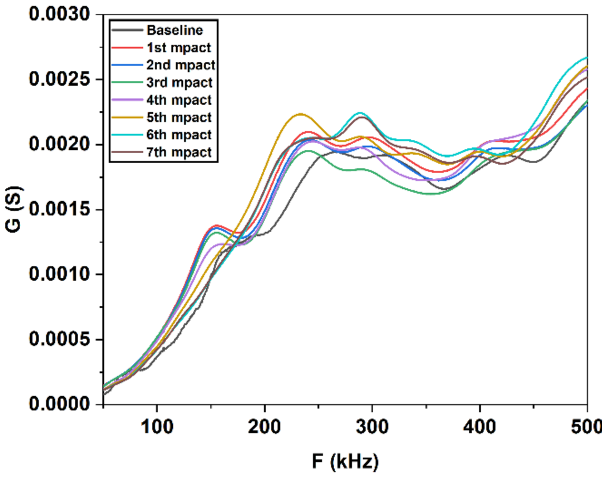

Figure 3. 28 Conductance signature for JKTPS at 100 ºC

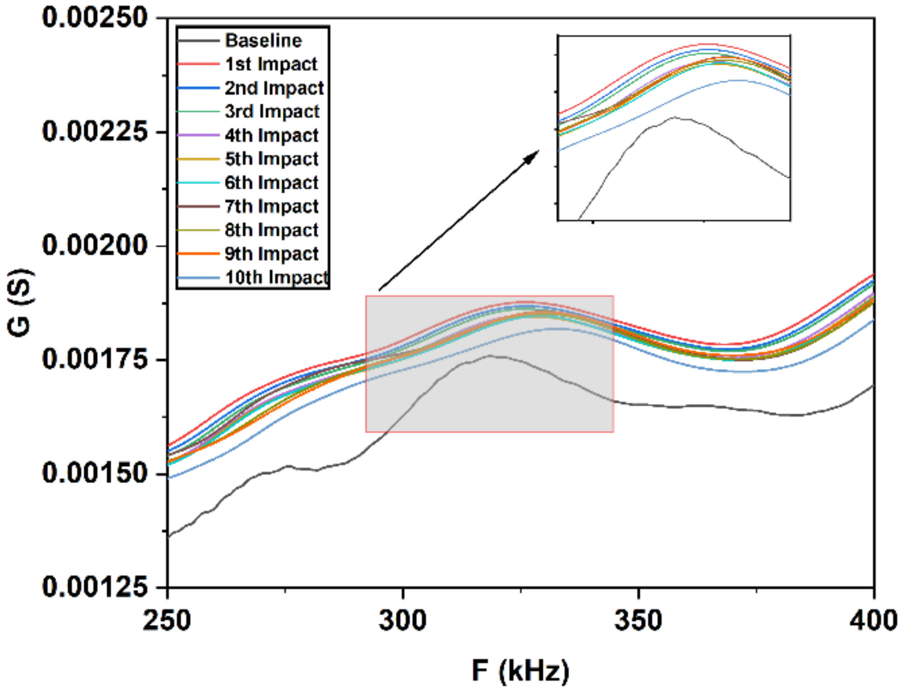

Figure 3. 29 Conductance signature for JKTPS at 150 ºC

3.8.5 Damage Assessment of Concrete under the Impact Loading at Varying Temperatures Using SBPS Sensors.

Figure 3. 30 to Figure 3. 32 depicts the graph between *G* in function of *f* for SBPS sensors at 3 m height of impact loading up to the failure under the three different temperature variations of 50 ºC, 100 ºC and 150 ºC. For an increase in temperature from 50 to 150 ºC, SBPS follow the same pattern As the JKTPS i.e. the shifting of the conductance signature were first in an upward

direction from the pristine stage to the first impact after that the conductance signature shifted downwards until failure**.**

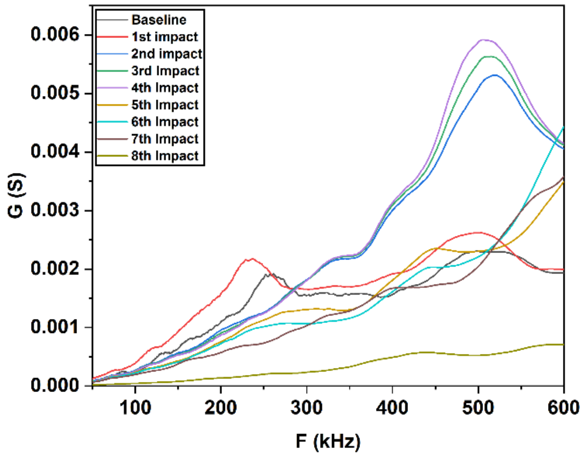

Figure 3. 30 conductance signature of SBPS at 50°C

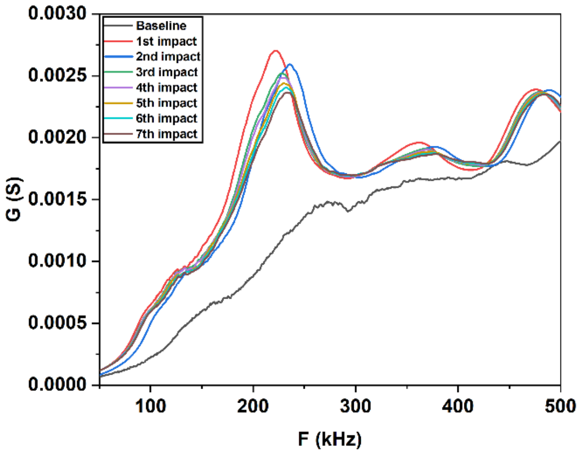

Figure 3. 31 conductance signature of SBPS at 100°C

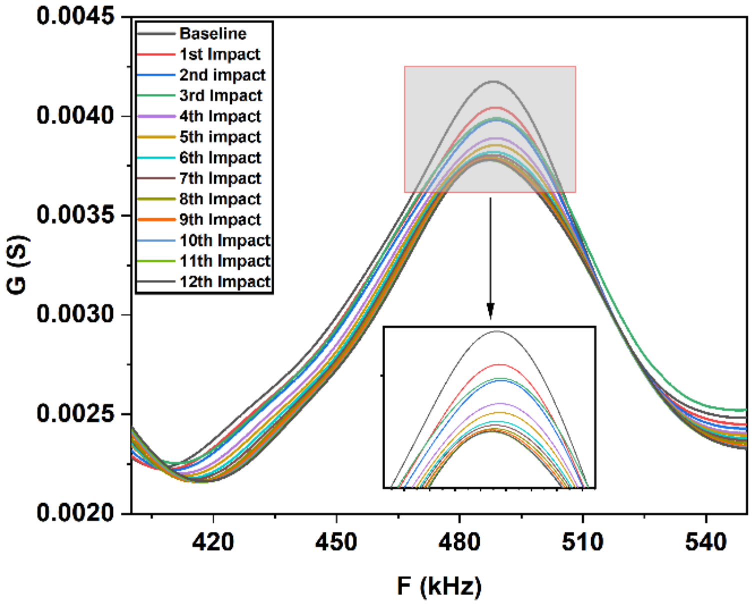

Figure 3. 32 Conductance signature of SBPS at 150°C

3.8.6 Damage Assessment of Concrete under the Impact Loading at Varying Temperatures Using NBPS Sensors.

Figure 3. 33 to Figure 3. 35 depicts the graph between *G* in the function of *f* for NBPS sensors at 3 m height of impact loading up to the failure under the three different temperature variations of 50 °C, 100 °C and 150 °C and they were follows the same pattern as the two previous sensors JKTPS and SBPS.

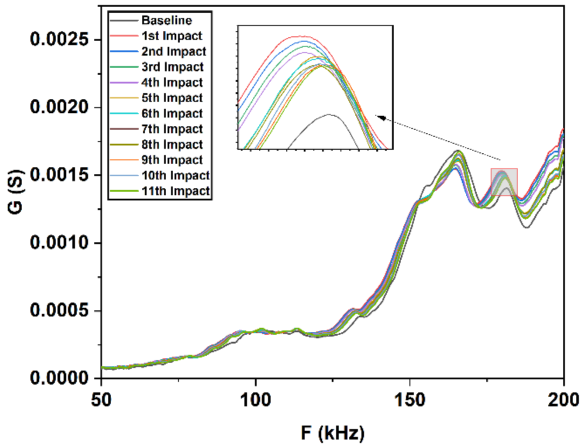

Figure 3. 33 Conductance signature for NBPS at 50ºC

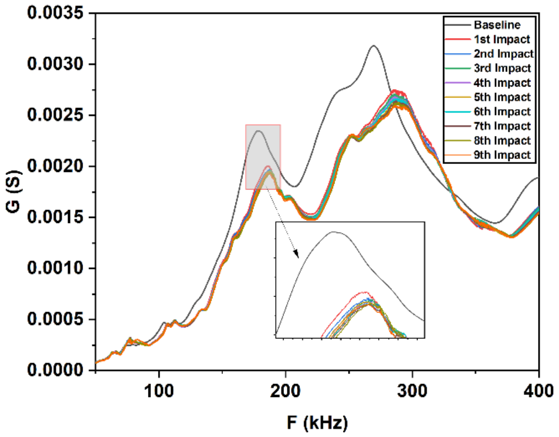

Figure 3. 34 Conductance signature for NBPS at 100ºC

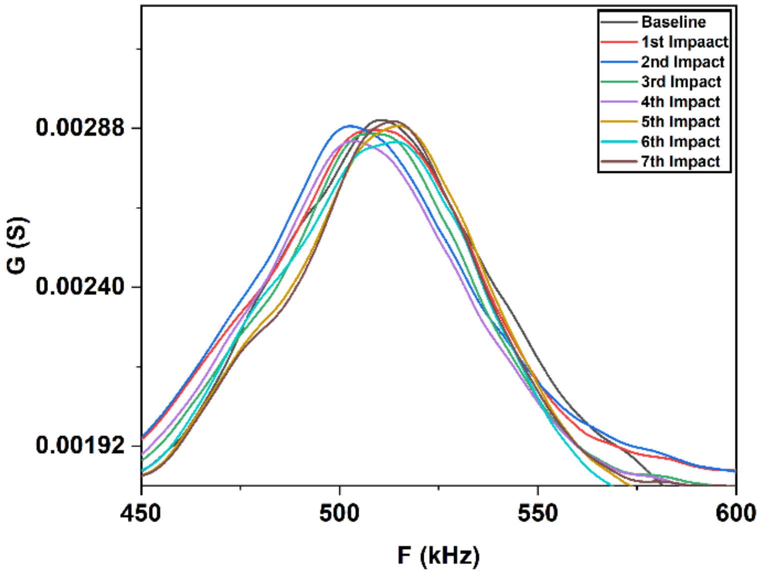

Figure 3. 35 Conductance signature for NBPS at 150 ºC

3.9 Analysis Based On Statistical Technique

Signature evaluation was done by two different types of numerical indices equations**.** These are the root mean square deviation (RMSD) and mean absolute percentage deviation (MAPD) as Equation (3.4)-(3.5). The RMSD and MAPD indices were used to quantify how much of the conductance signature of all three JKTPS, NBPS and SBPS has been altered due to impact damage at varying temperatures, as defined by,

$$\boldsymbol{RMSD} = \left(\frac{\sum_{k=1}^{N} \left[Re(Z_k)_j - Re(Z_k)_i \right]^2}{\sum_{k=1}^{N} [Re(Z_k)_i]^2} \right)^{\frac{1}{2}} \qquad \textbf{3.4}$$

$$MAPD = \frac{1}{N}\sum_{k=1}^{N}\left|\left[Re(Z_k)_j - Re(Z_k)_i\right]/Re(Z_k)_i\right| \tag{3.5}$$

Here, $Re\ (Z_k)_i$ is the reference impedance signature and $Re(Z_k)_j$ is the corresponding signature number of impedance signatures represented by N. The RMSD and MAPD variations for each various sensor configuration are calculated independently under the 3 m height of impact loading at four different temperatures of ambient, 50,100, and 150 °C while keeping the pristine state as a baseline structure. Figure 3. 36 - Figure 3. 41 depicts the RMSD and MAPD variation due to the combined effect of impact and temperature for each sensor configuration separately. Figure 3. 36 depicts the fluctuation of the RMSD value for the JKTPS sensors from ambient to 150 °C temperatures. The RMAD value for JKTPS at ambient temperature follows an increasing pattern ranging from 2.17 to 10.37 % for complete failure up to the seven impacts. These variation goes increasing for the temperature of 50 to 150 °C. For 50 °C RMSD variation varies from 11.479 to 15.182 %. However, the variation for 100 °C temperature was inconsistent. For 150 °C temperature variations were shown the downward pattern i.e. 12.38 to 7.86 %.

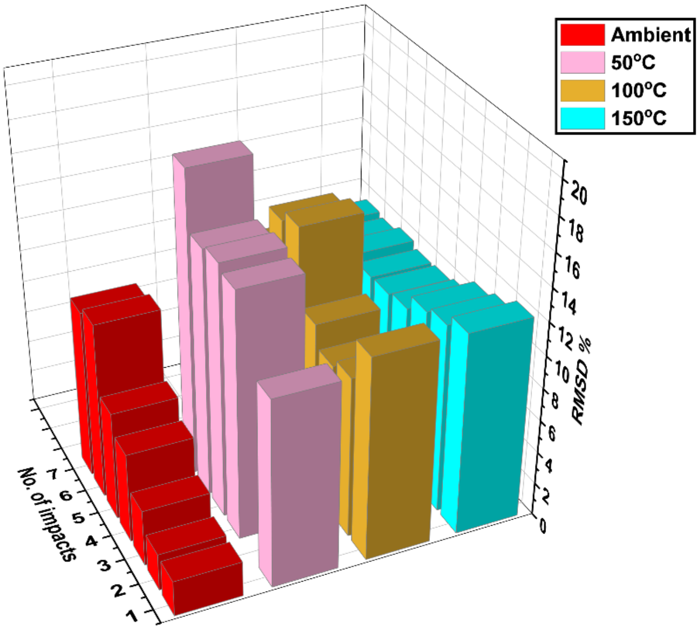

Figure 3. 36 RMSD value for JKTPS with increasing impact number for different temperatures a) ambient b) 50 °C C) 100 °C d) 150 °C

Figure 3. 37 depicts the fluctuation of the RMSD value for the SBPS sensors from ambient to 150 °C temperatures. For the pristine state they were follow an increasing pattern varied from 0.656 to 2.174 % as per the same trend as JKTPS sensors. However, the variation for the 50 °C

was inconsistent. For 100 and 150 °C they follow the decreasing pattern from 46.98 to 36.78 % and 78.01 to 67.77 % respectively.

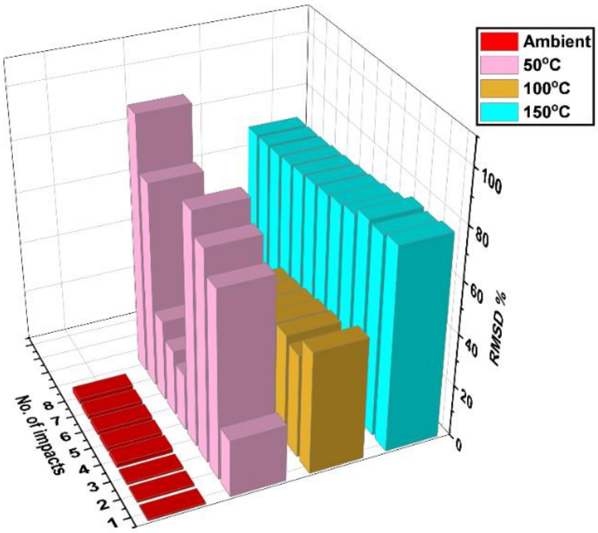

Figure 3. 37 RMSD Value for SBPS at increasing impact for different temperature conditions ambient, 50 °C, 100 °C and 150 °C

Figure 3. 38 depicts the fluctuation of the RMSD value for the NBPS sensors from ambient to 150 °C temperatures. The RMSD value variation for the ambient temperature was 3.16 to 2.82 %, they followed a decreasing pattern from 9.4 % to 3.62 % at 50 °C and an increasing pattern from 18.5 to 20.84 % at 100 °C. Figure 3. 39 depicts the fluctuation of the MAPD value for the JKTPS sensors from ambient to 150 °C temperatures.

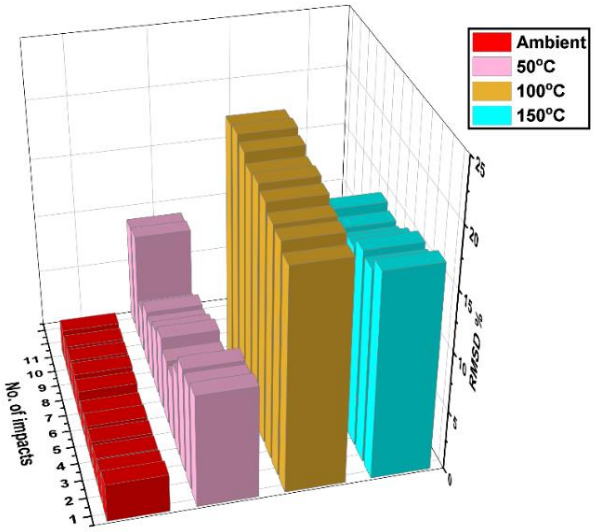

Figure 3. 38 RMSD Value for NBPS at increasing impact for different temperature conditions ambient, 50 °C, 100 °C and 150 °C

The MAPD value for ambient temperature varied from 0.4738 to 14.21 % in an increasing pattern, and the same pattern was followed for 50 °C from 13.74 to 16.89 %. MAPD variations at 100 °C are inconsistent, but at 150 °C they follow a decreasing pattern, decreasing from 17.98 to 12.28 %.

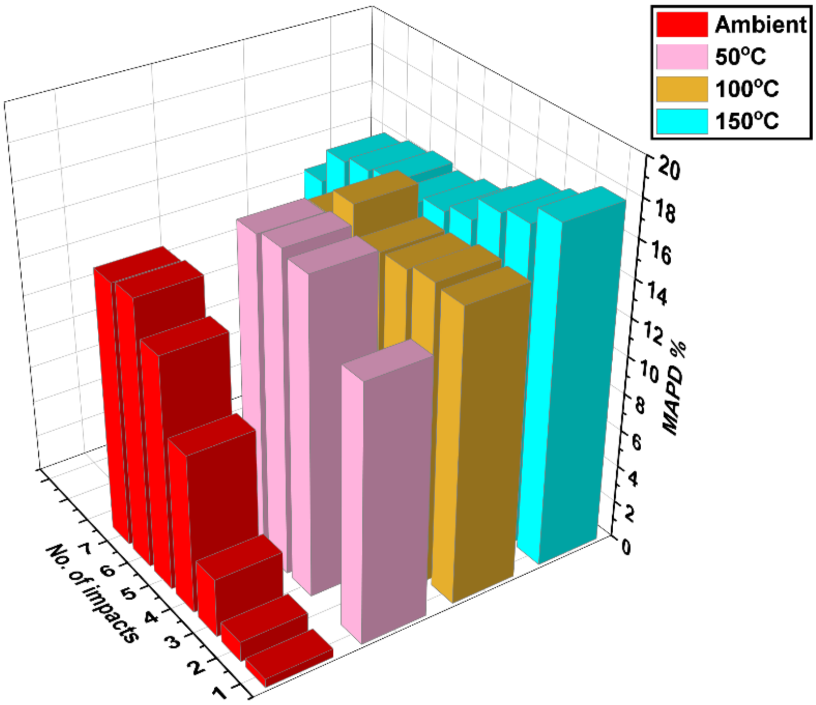

Figure 3. 39 MAPD Value for JKTPS at increasing impact for different temperature conditions ambient, 50 °C, 100 °C and 150 °C

Figure 3. 40 depicts the fluctuation of the MAPD value for the SBPS sensors from ambient to 150 °C temperatures. The MAPD value for SBPS sensors ranges from 0.966 to 2.81 % at ambient temperature. They did not follow any pattern at 50 °C, but at 100 and 150 °C, they followed a decreasing trend from 65.24 to 53.56 % and 95.49 to 81.93 %, respectively.

Figure 3. 41 depicts the fluctuation of the MAPD value for the NBPS sensors from ambient to 150 °C temperatures. The MAPD value followed an increasing pattern from 1.396 to 3.22 % at ambient temperature and the same increasing pattern followed for the 100 °C temperature from 14.63 to 16.31%. They followed a decreasing pattern from 10.34 to 4.22 % and 12.95 to 11.22 % for 50 and 150 °C, respectively.

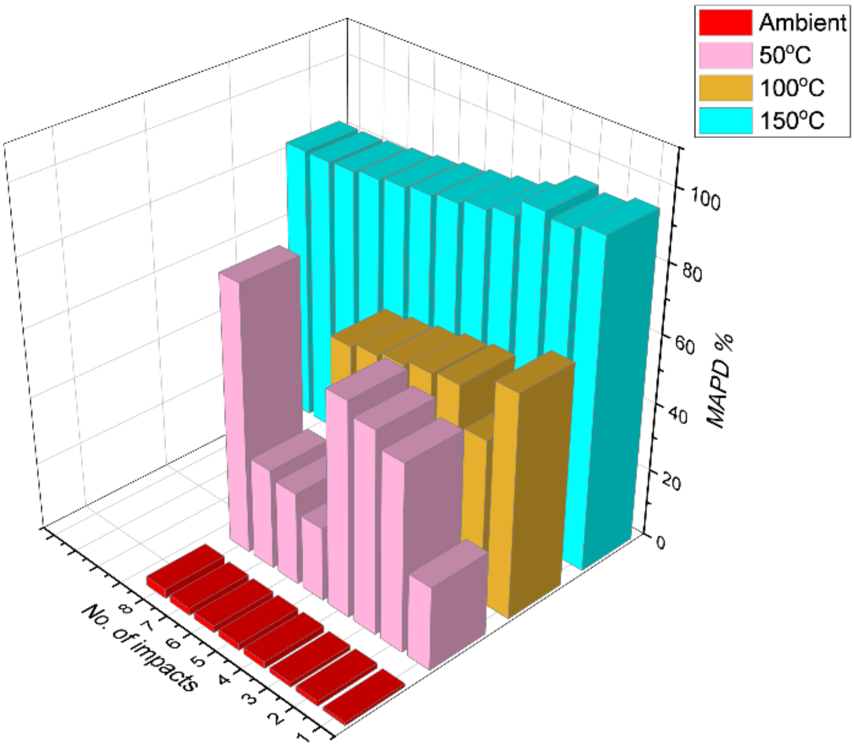

Figure 3. 40 MAPD Value for SBPS at increasing impact for different temperature conditions ambient, 50 °C, 100 °C and 150 °C

3.10 Peak Conductance and Resonant Frequency

The variation in the peak conductance and resonant frequency value was also analyzed with the increase in the number of impacts. Figure 3. 42 shows the variation of peak conductance and resonant frequency in the function of incremental impact load for SBPS sensors at varying temperatures. It was observed that both the resonant frequency and peak conductance has follow the same pattern for 50 °C, 100 °C and 150 °C. For every increase in temperature from 50 to 150 °C, the resonant frequency decreased from the pristine state to the first impact and then increased after the first impact, whereas the peak conductance increased from the pristine state to the first impact and then decreased after the first impact. The highly sensing behaviour of PZT sensors against temperature causes the increasing or decreasing value of peak conductance and resonant frequency from pristine to first impact. The decreasing behaviour of the peak conductance after the first impact was caused by an increase in crack width and depth as the number of impacts increased. The loss of stiffness causes an increase in crack depth and width. The loss of damping in the cube caused the resonance peak to rise in nature after the first impact as well as the same as Negi et al. (2019).

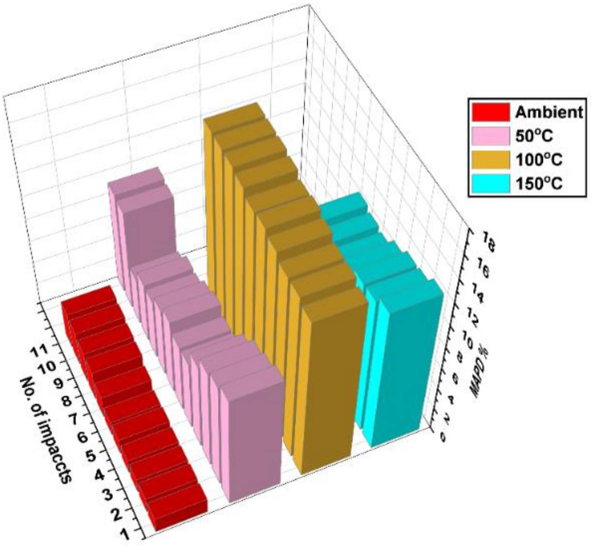

Figure 3. 41 MAPD Value for NBPS at increasing impact for different temperature conditions ambient, 50 ºC, 100 ºC and 150 ºC

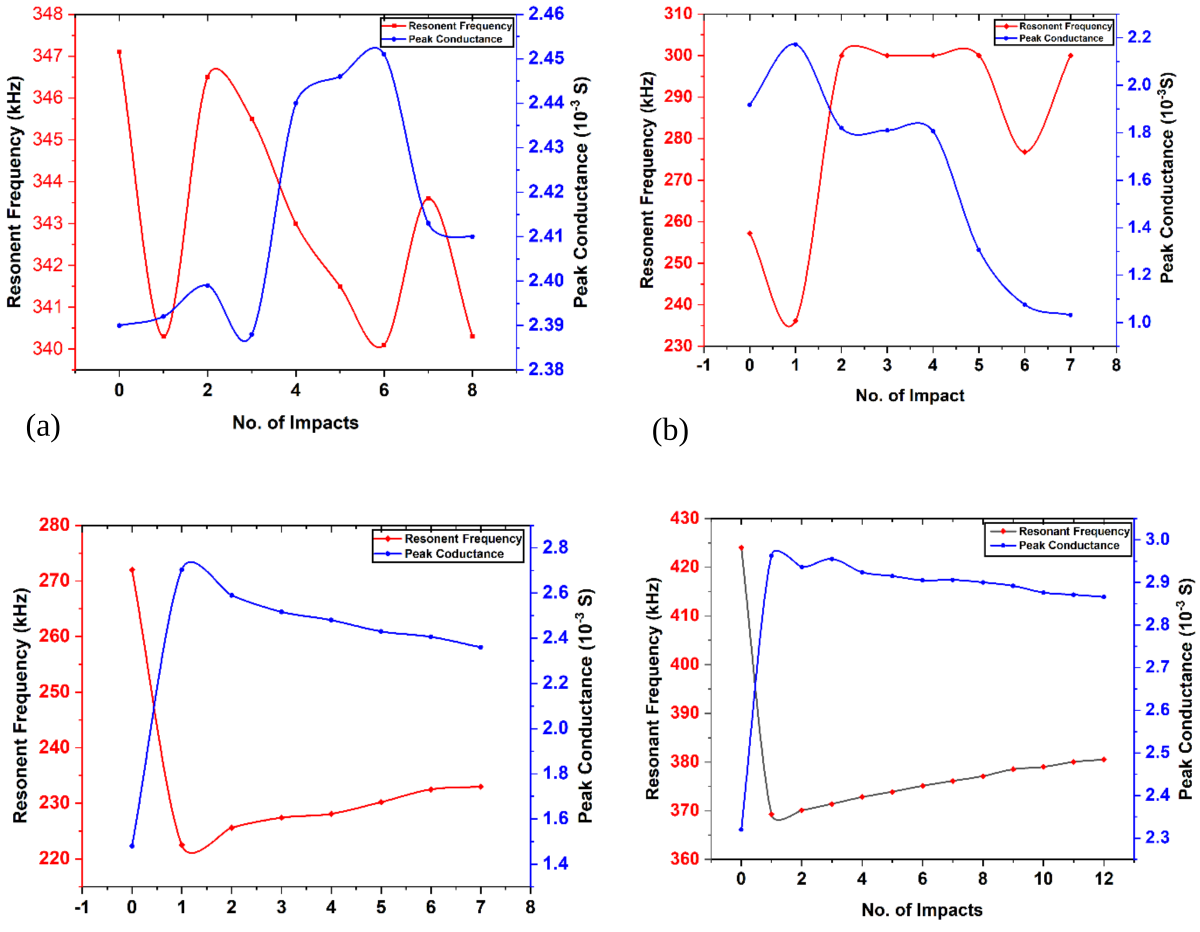

(a)

(b)

(c)

(d)

Figure 3. 42 Variation of Resonant frequency and peak conductance with the increase in impact for SBPS at varying temperature a) ambient b) 50 ºC c) 100 ºC d) 150 ºC

3.11 Analysis Based On Equivalent Based Parameter

Impedance-based discovery has become more useful in detecting damage in recent years. In the field of EMI technique, this is now a well-established concept that has proven to be more accurate than simply observing the change in conductance signature proof by Bhalla et.al (2017). A well establish relation was derived based on the identified equivalent system in between the changes in conductance signature that occur during the damage in concrete and a corresponding change in equivalent stiffness parameters (ESPs) such as stiffness, mass, and damping. Soh and Bhalla (2005) derive the mechanical impedance ($Z_{s,eff}=x+yj$) for the monitored structure at a specific frequency ($\omega=2\pi f$). In this analysis for all cases of impact loading under temperature variation, signatures consisting of G and B plots are retrieved in the frequency range of 50 kHz-500 kHz, plot the graph of experimental plots in between x in the function of f and y in the function of f. Again, the experimental plots of x and y were compared to the Hixon equivalent system model. Figure 3. 43 and Figure 3. 44 represents the experimental plot of x and y with the frequency respectively at incremental damage state under the 3 m height of impact for SBPS at 150 ^{o}C temperature. After examining the graphs of x in function of f and y in function of f through the equivalent plot, a dashpot*(c)*, spring *(k)*, and mass *(m)* equivalent system in series as depicted in Figure 3. 45 (b) were found to be similar. Figure 3. 45 depicts the usual variation of x and y with the frequency for the identified series *m-c-k* system. The ESPs values were obtained using experimental x and y values within the frequency range, which were then entered into the Equation (3.6), (3.7) and (3.8) to calculate the m-c-k values. These absolute values of *m-c-k* are derived by rearranging the Equations (3.9) and (3.10) with some boundary conditions.

$$\boldsymbol{m = \frac{(\omega_o{}^2-\omega^2)(x^2+y^2)}{\omega\omega_o{}^2 y}} \qquad \textbf{3.6}$$

$$\boldsymbol{k = \frac{(\omega_o{}^2-\omega^2)(x^2+y^2)}{\omega y}} \qquad \textbf{3.7}$$

$$\boldsymbol{c = \frac{(x^2+y^2)}{x}} \qquad \textbf{3.8}$$

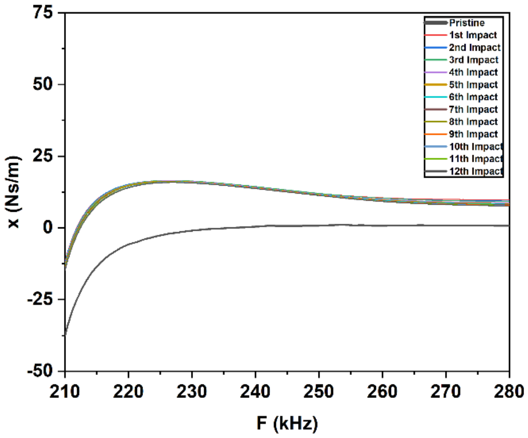

Figure 3. 43 mechanical impedance variation of x vs f

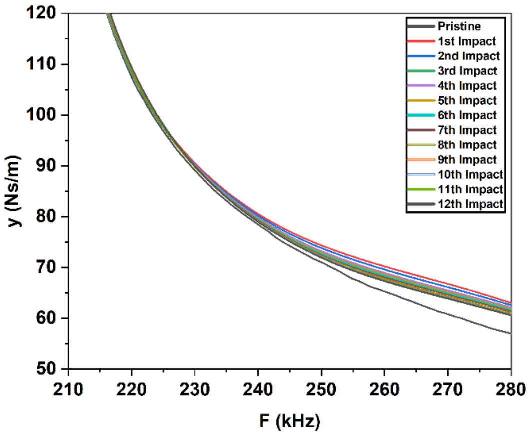

Figure 3. 44 mechanical impedance variation of y vs f

Where $\omega = \omega_o$ at $y = 0$. This Solution is valid for $y>0$ and $|\omega| < \omega_o$ or $y<0$ and $|\omega| > \omega_o$.After determining the average values of the m-c-k, the equivalent values of x and y are calculated using Equations 3.9 and 3.10.

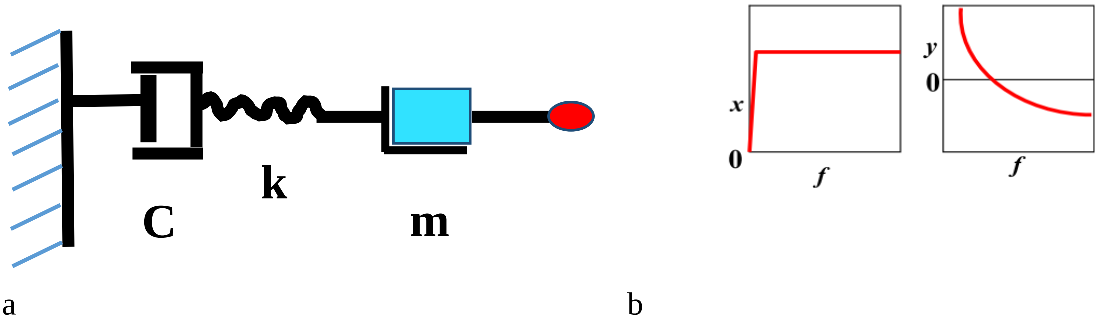

Figure 3. 45 (a) Equivalent mechanical system consist of spring, mass and damper in series (b) variation of x and y for the identified series m-c-k system

$$x = \frac{c^{-1}}{c^{-2}+\left(\frac{\omega}{k}-\frac{1}{\omega m}\right)^2} \qquad 3.9$$

$$y = \frac{-\left(\frac{\omega}{k}-\frac{1}{\omega m}\right)^2}{c^{-2}+\left(\frac{\omega}{k}-\frac{1}{\omega m}\right)^2} \qquad 3.10$$

Table 3. 6 shows the average value of mass, damping, and stiffness for three sensor configurations JKTPS, SBPS, and NBPS under both impact heights of 3 and 3.5 m at 150 ^{o}C for a typical sample of concrete cube. To calculate the ESPs value, first compare the plots of experimental and numerical impedances. Based on this, a series combination of spring mass and damping was chosen in the definite frequency range of 210-280 kHz that was found to be most similar, as shown in Figure 3. 45 (b). The typical variation of x vs f and y vs f, as shown in Figure 3. 46, shows good agreement between the experimental and equivalent plots at a range of 210 – 280 kHz between the experimental and equivalent plots, a series system was chosen for the analysis of ESPs (damping and stiffness) parameter .ESPs value were calculated for all the different sensors configuration under the two different impact loading at varying temperature, where as in the results, ESPs value were shown for the typical concrete cube sample of JKTPS sensors for 150 ^{o}C temperature under the 3 and 3.5 m impact loading. Figure 3. 47 (a) and Figure 3. 47 (c) show that the equivalent damping (c) for 3 and 3.5 m impact heights at 150 ^{o}C decreases first for the first impact when compared to the baseline. This is due to the extremely high sensitivity of the Piezo sensors to temperature, but it increases further as the impact increases due to the loss of concrete strength; this followed the opposite pattern as explained by the (Bansal et al. 2022), which states that the value of dampness decreases as the strength of the concrete increases.

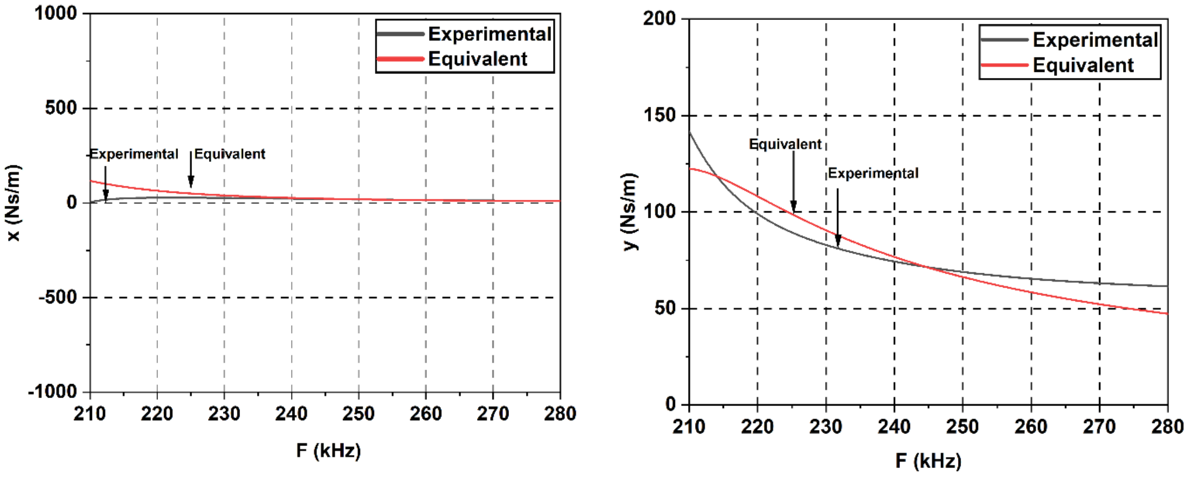

Figure 3. 46 Comparison of experimental and equivalent plots of x vs f and y vs f

Figure 3. 47 (b) and Figure 3. 47 (d) show that the equivalent stiffness (k) at 150 ^{o}C for 3 and 3.5 m impact heights increases first for the first impact and decreases further as the increase in number of impacts. The increase in the k value for the first impact is because of the high

temperature sensitivity of piezo sensors, and the subsequent decrease in the k value is due to the increase in concrete damage.

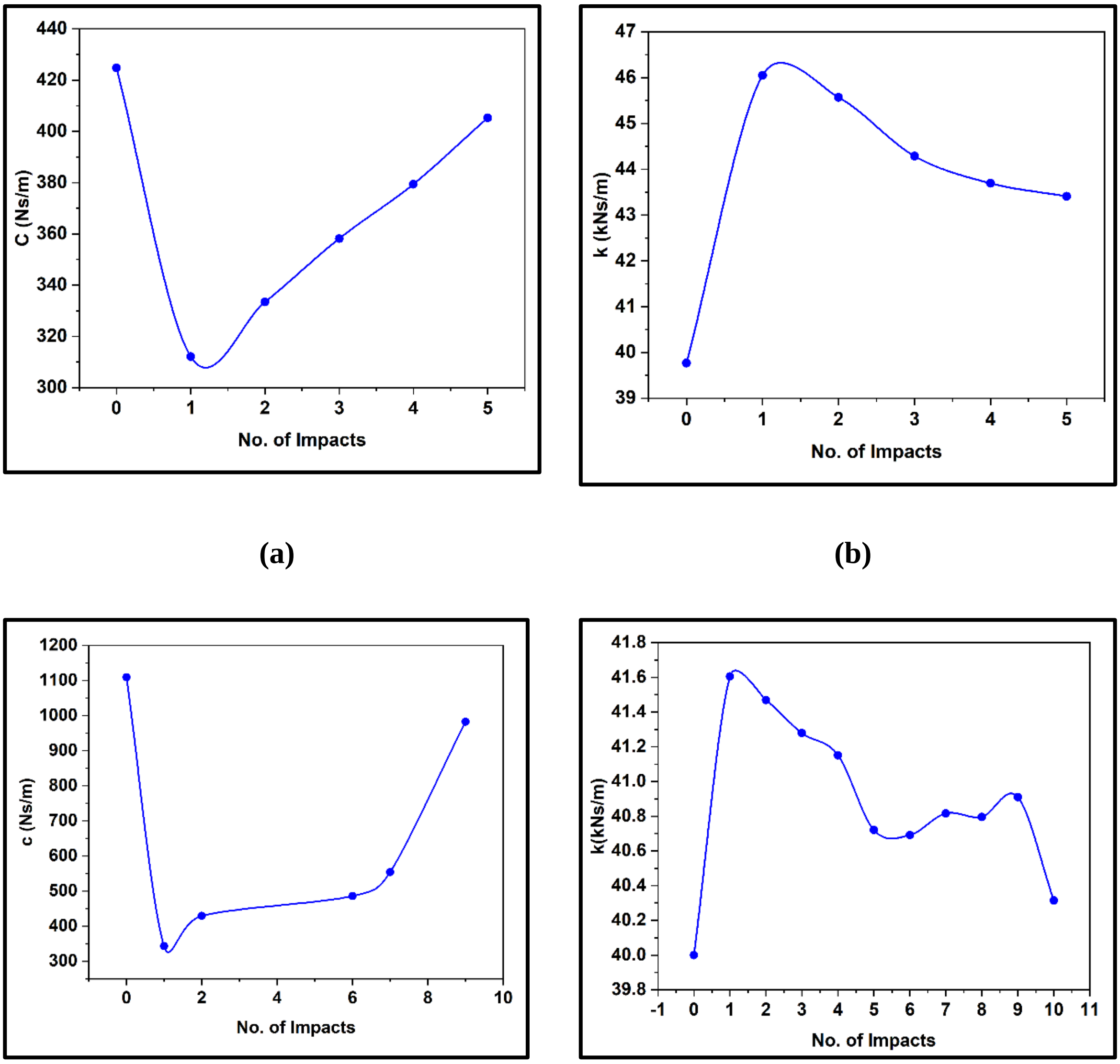

(a) **(b)**

(c) **(d)**

Figure 3. 47 Equivalent structural parameter of concrete cube for JKTPS at 150 ^{o}C temperatures under 3 and 3.5 m height of impact a) Damping for J4d cube number under 3.5 m impact b) Stiffness under 3.5 m impact c) Damping for J4 cube number under 3 m impact d) Stiffness for J4 cube number under 3 m impact

Figure 3. 48 depicts the variation of the Equivalent stiffness value with the number of impacts for various sensor configurations under 150 ^{o}C temperature. Equivalent stiffness values follow the same pattern for all sensor configurations as the number of impacts increases. Except for pristine to first impact, the equivalent stiffness value decreased as the number of impacts increased up to failure, the decrease of the equivalent stiffness value with the increasing impacts

Table 3. 6 Average values of m-c-k for different sensors configuration at 3 m impact height under 150 °C

Sensors type	Height (m)	Temperature (°C)	Mass (kg)	Damping (Ns/m)	Stiffness (N/m)
JKTPS	3	150	$2.69x10^{-2}$	$8.516x10^{3}$	$4.08x10^{4}$
SBPS			$2.75x10^{-2}$	$6.28x10^{-2}$	$4.23x10^{4}$
NBPS			$2.77x10^{-2}$	$9.26x10^{-2}$	$4.23x10^{4}$
JKTPS	3.5	150	$2.83x10^{-2}$	$7.059x10^{3}$	$4.89x10^{4}$
SBPS			$2.91x10^{-2}$	$6.10x10^{-2}$	$5.01x10^{4}$
NBPS			$2.99x10^{-2}$	$8.35x10^{-2}$	$5.11x10^{4}$

indicates the increase in damage in the sample. The value of the increasing damage was due to the loss of its strength and the value of increasing stiffness for the first impact was due to the PZT high-temperature sensitivity.

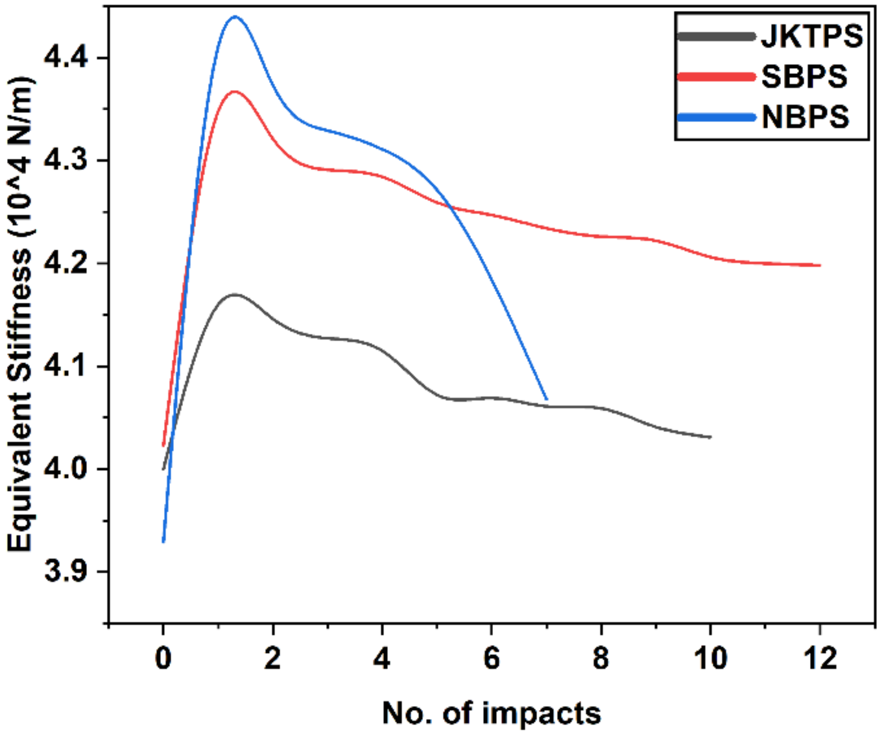

Figure 3. 48 Variation of Equivalent Stiffness at 150 °C for a) JKTPS b) SBPS c) NBPS

To gain a better insight into the extent of damage, the equivalent stiffness values are presented in tabular form. Table 3. **7** displays the variations in equivalent stiffness for different sensor configurations when subjected to a 3 m impact at ambient temperature. It reveals a stiffness loss of 6.68% for JKTPS sensors, 5.742% for SBPS sensors, and 4.21% for NBPS sensors. In Table 3. 8, the equivalent stiffness variations for different sensor configurations under a 3 m impact at 150 °C are outlined. Notably, the stiffness loss increases with the rise in temperature from ambient to 150 °C, ranging from 6.87% for NBPS sensors to 10.42% for JKTPS sensors. This data illustrates that the stiffness loss escalates by approximately 3 to 4% with the increase in temperature.

Table 3. 7 Equivalent stiffness variation for different sensors configuration under 3 m height of impact at ambient temperature

Number of Impact	Equivalent stiffness for JKTPS (10^4 N/m)	Equivalent stiffness for SBPS (10^4 N/m)	Equivalent stiffness for NBPS (10^4 N/m)
Healthy State	4.50	4.51	4.51
1st	4.481	4.487	4.50
2nd	4.475	4.478	4.48
3rd	4.451	4.461	4.47
4th	4.322	4.387	4.40
5th	4.291	4.352	4.37
6th	4.280	4.310	4.35
7th	4.272	4.291	4.32
8th	4.250	4.280	
9th	4.221	4.289	
10th	4.199	4.251	
% Variation	**6.68 % Loss of Stiffness**	**5.742 % Loss of Stiffness**	**4.21 % Loss of Stiffness**

Table 3. 8 Equivalent stiffness variation for different sensors configuration under 3 m height of impact at 150 °C

Number of Impact	Equivalent stiffness for JKTPS (10^4 N/m)	Equivalent stiffness for SBPS (10^4 N/m)	Equivalent stiffness for NBPS (10^4 N/m)
Healthy State	4.50	4.51	4.51
1st	4.16	4.34	4.41
2nd	4.146	4.32	4.37
3rd	4.127	4.29	4.32
4th	4.115	4.28	4.31
5th	4.027	4.24	4.27
6th	4.069	4.23	4.25
7th	4.061	4.21	4.20
8th	4.059	4.20	
9th	4.041	4.18	
10th	4.031	4.17	
% Variation	**10.42 % Loss of Stiffness**	**7.53 % Loss of Stiffness**	**6.87 % Loss of Stiffness**

3.12 Estimation of Remaining Life Using Equivalent Structural Parameter

For establishing remaining life model, further use the equivalent stiffness parameter i.e. already calculated in the previous section. A non-dimensional stiffness loss parameter Δs was used to quantify the changes in the stiffness caused by incremental damage. Δs was defined as given below

$$\mathbf{\Delta s}=\left|\frac{\boldsymbol{\Delta k}}{\boldsymbol{k}}\right| \qquad \mathbf{3.11}$$

Where, Δk change in equivalent stiffness compared to k and k is the original equivalent stiffness in pristine stage. As indicated below, another non-dimensional parameter, L, was included to denote the structure's remaining life.

$$\boldsymbol{L}=\mathbf{1}-\frac{\boldsymbol{N}}{\boldsymbol{N_0}} \qquad \mathbf{3.12}$$

Where N_0 signifies the total number of impacts applied till failure and N denotes the number of impacts applied until a specific stage. Figure 3. 49 shows the variation of the L in function of Δs for the JKTPS, NBPS and SBPS. Each sensors has shown the similar pattern of the L in function of Δs graph i.e with the increase in the value of Δs, remaining life of structure get reduce.

$$\mathbf{L = 440.96978\ (\Delta s)^{2} - 47.24186\ (\Delta s) + 1.22576} \qquad \mathbf{3.13}$$

$$\mathbf{L = 517.18207\ (\Delta s)^{2} - 90.72141\ (\Delta s) + 3.96587} \qquad \mathbf{3.14}$$

$$\mathbf{L = -72.63299\ (\Delta s)^{2} + 4.51\ (\Delta s) + 0.52883} \qquad \mathbf{3.15}$$

A empirical equation was also develop based on the L in function of Δs graph for predicting the remaining life of structure under this experiment in terms of Δs using best fit curve (Bhalla et al. 2012; Dixit and Bhalla 2018). Empirical equation for each sensors for JKTPS, SBPS and NBPS are mentioned from Equation 3.13 to 3.15 respectively.

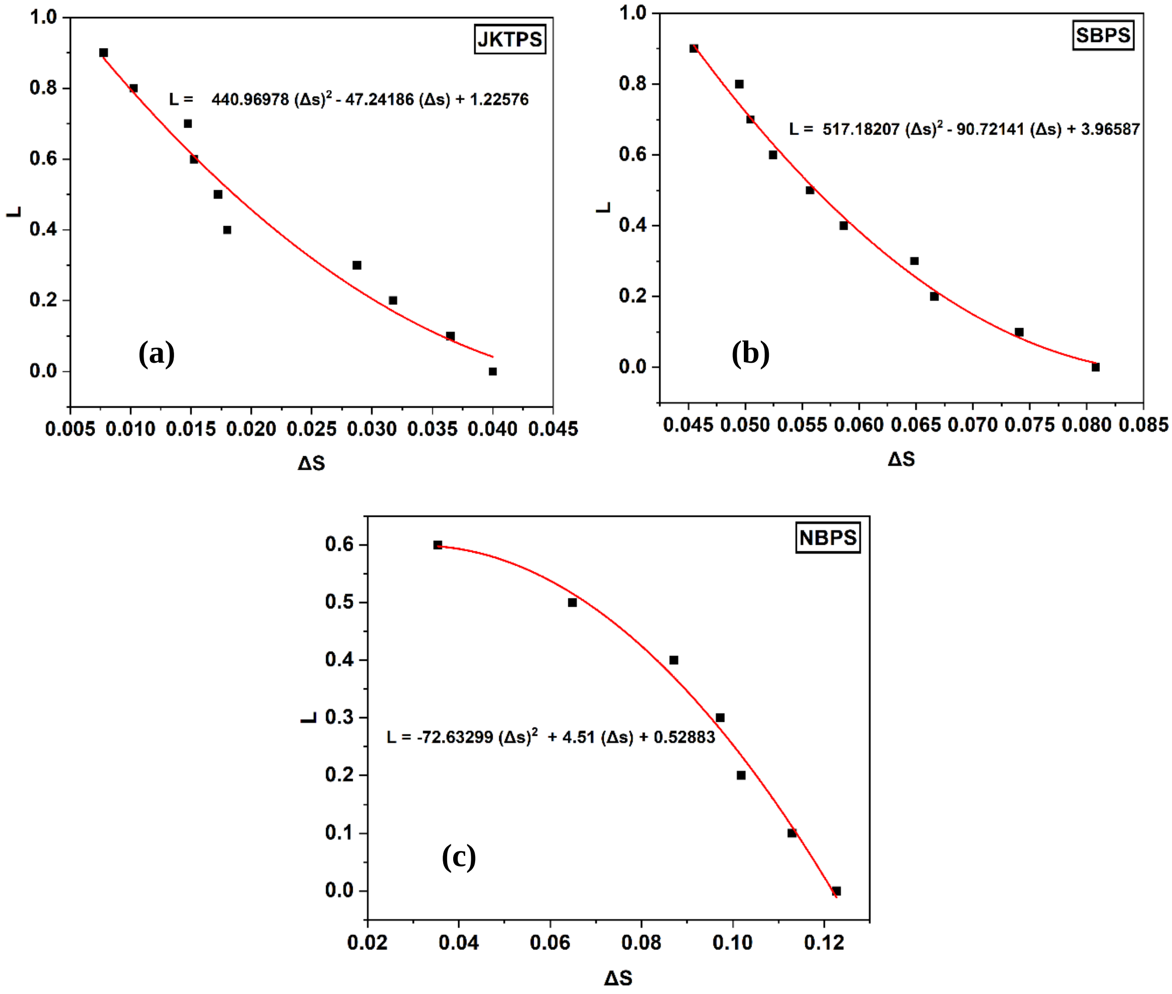

Figure 3. 49 Variation of L vs Δs for a) JKTPS b) SBPS c) NBPS

3.13 Temperature Effects on EMI Technique

Temperature compensation is a fundamental concept in various fields and technologies, and it involves adjusting or correcting measurements or behaviour to account for the influence of temperature variations. PZT materials exhibit high sensitivity to temperature, leading to occasional false damage alarms when employing the EMI technique. To mitigate these false alarms, a temperature compensation technique was integrated when utilizing the EMI method. Within this section, compensation was carried out through a two-step process, involving both horizontal and vertical adjustments. As presented in Figure 3. 50, an observable leftward frequency shift is evident in the electromechanical signature as the temperature increases. This shift can be attributed to the impact of the temperature-dependent dielectric constant ε_{33}, a recognized property of the PZT sensor, on the electrical impedance signature.

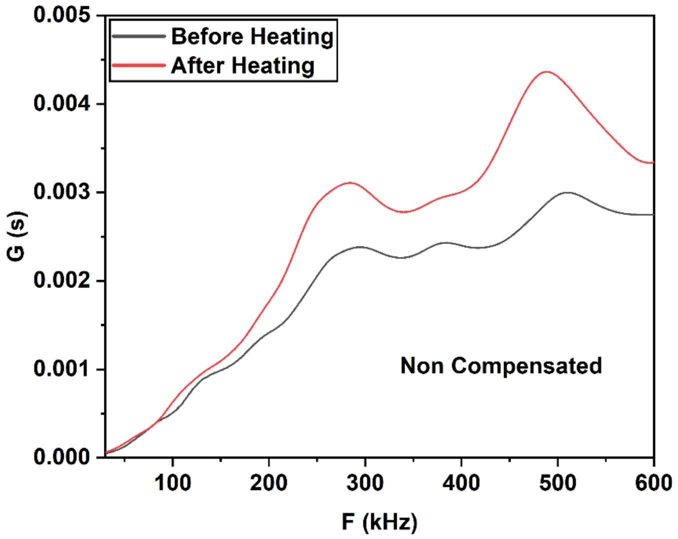

Figure 3. 50 Effect of 50 °C temperature on signature

The signature, as determined by the observation, is a function of the frequency range. Separate compensation algorithms were derived for each frequency band. Admittance signatures were generated through experimental procedures involving the PZT patch on the host structures. The measurements were subsequently visualized, and the signature deviation was partitioned into 25 kHz frequency range intervals.

3.13.1 Horizontal Compensation

After subjecting the concrete cube to heating, it was observed that the signatures consistently shifted to the left across all temperature conditions ranging from 50 to 150 °C. To address these leftward shifts effectively, a horizontal compensation method was implemented. Initially, the signatures were divided into 25 kHz intervals, and a trial-and-error approach was employed to determine the necessary horizontal adjustments. As depicted in Figure 3. 51, the uncompensated signature of a typical JKPTS sensor at 50 °C clearly demonstrates the leftward shift. However, upon the application of the compensation technique using the trial-and-error method, Figure 3. 52 reveals that the peak aligns perfectly with the reference line.

3.13.2 Vertical Compensation

After subjecting the concrete cube to heating, it was observed that the signatures consistently shifted to the upward direction across all temperature conditions ranging from 50 to 150°C. To address these upward shifts effectively, a vertical compensation method was implemented. Initially, the signatures were again divided into 25 kHz intervals same as the horizontal compensation, and a regression analysis approach was employed to determine the necessary vertical adjustments. As depicted in Figure 3. 53, the uncompensated signature of a typical JKPTS sensor at 50 °C clearly demonstrates the upward shift. However, upon the application of the compensation technique, Figure 3. 54 reveals that the peak aligns perfectly with the reference line.

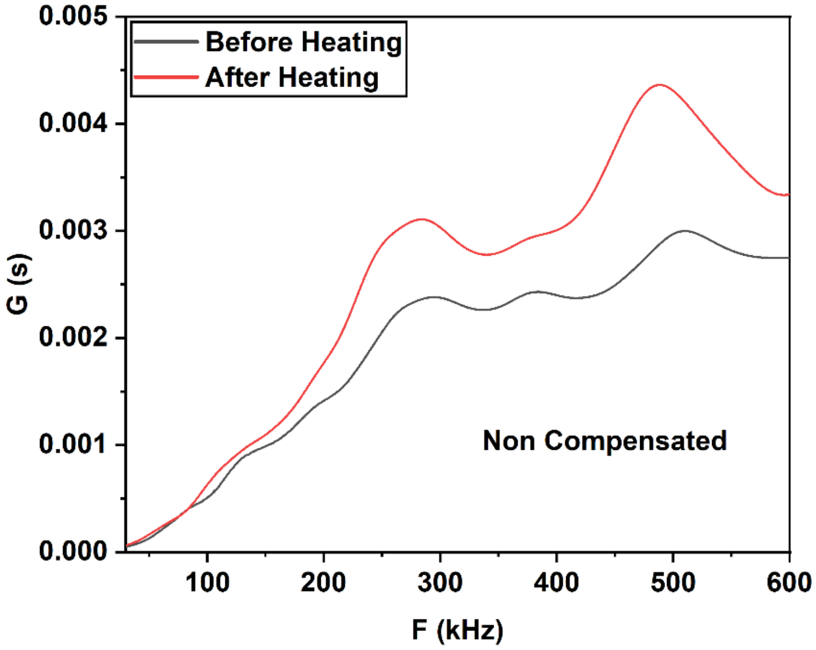

Figure 3. 51 Non-compensated signature at 50 ºC temperature

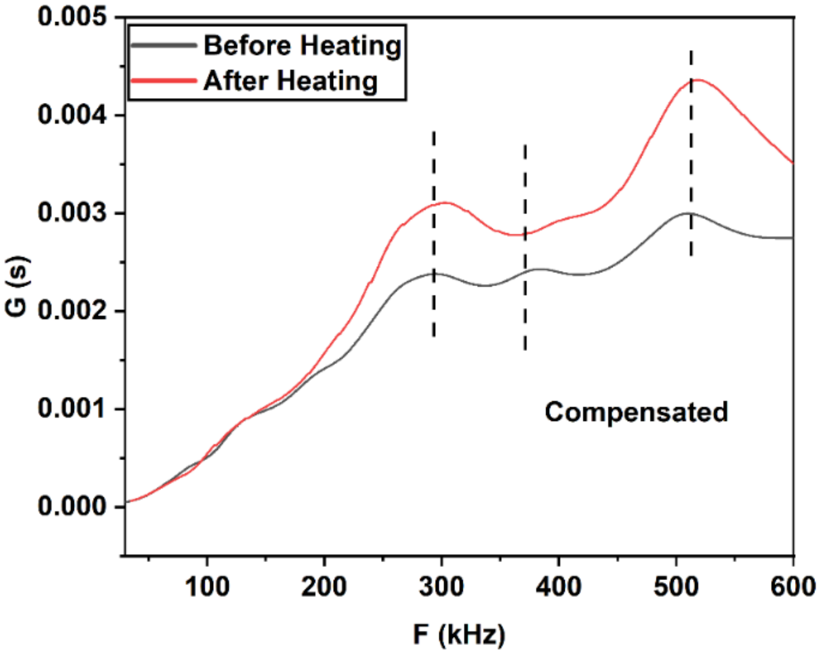

Figure 3. 52 Compensated signature at 50 ºC temperature

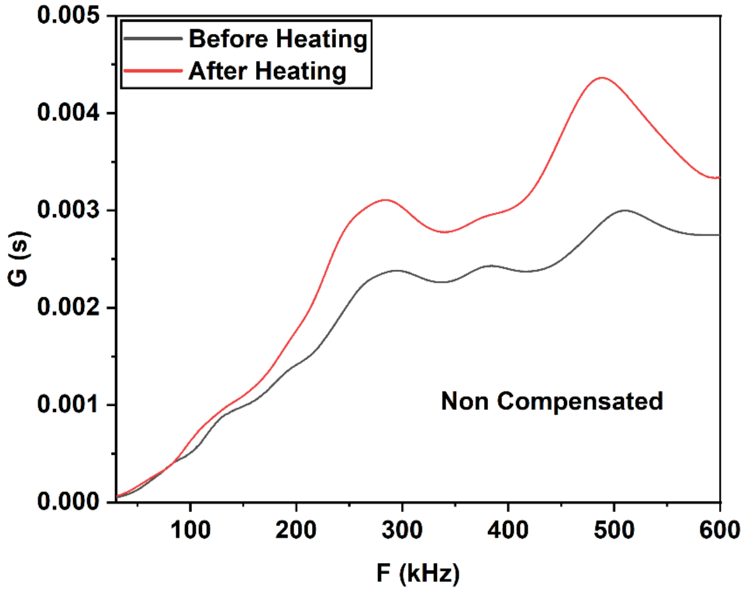

Figure 3. 53 Non-compensated signature at 50 ºC temperature

3.13.3 Combined Compensation

To minimise the effect of temperature, must compare the signature under the same temperature conditions. As discovered in the previous section, after applying vertical compensation, the signature at 50 ºC overlapped with the baseline signature, indicating that no damage was found in the concrete after the increase in 50 ºC temperature, and the same pattern was followed for the 100 ºC and 150 ºC temperature conditions. As a result, for the combined compensation of the temperature correction, we compare the signature at the same temperature condition by using the baseline signature after cooling the sample rather than the ambient temperature.

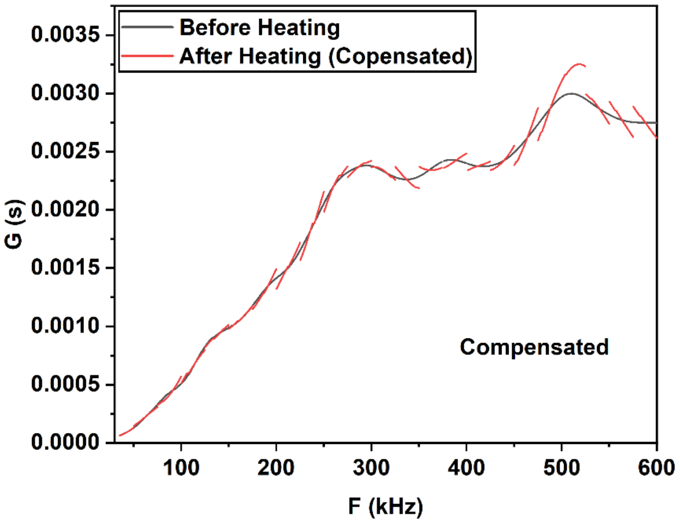

Figure 3. 54 Compensated signature at 50 ºC temperature

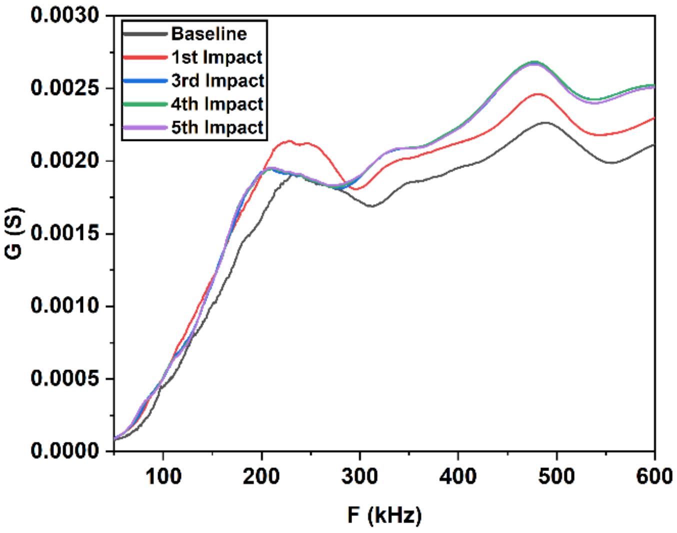

Figure 3. 55 Non-compensated signature at 50 ^{o}C temperature from baseline to failure

Figure 3. 55 displays the uncompensated signature of the JKTPS sensors at a temperature of 50°C, and it is evident that the signature lacks any discernible pattern due to the absence of compensation. However, upon implementing the combined compensation method, Figure 3. 56 illustrates a noteworthy downward pattern in the signatures.

Figure 3. 57 and Figure 3. 58 depict the response of both uncompensated and compensated signatures under various impact loading conditions at a temperature of 100°C and a 3 m impact height for JKTPS sensors. As previously discussed in Figure 3. 28, Figure 3. 57 illustrates uncompensated signatures that lack a clear and consistent pattern. However, Figure 3. 58 demonstrates the impact of compensation, where the signatures now exhibit a distinct pattern and shift consistently in a downward direction.

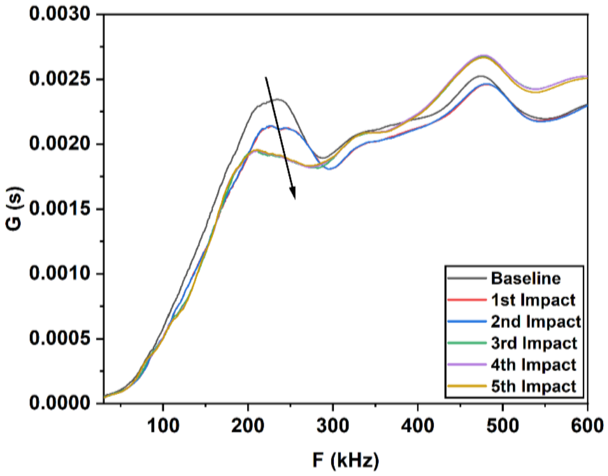

Figure 3. 56 Compensated signature at 50 ^{o}C temperature from baseline to failure

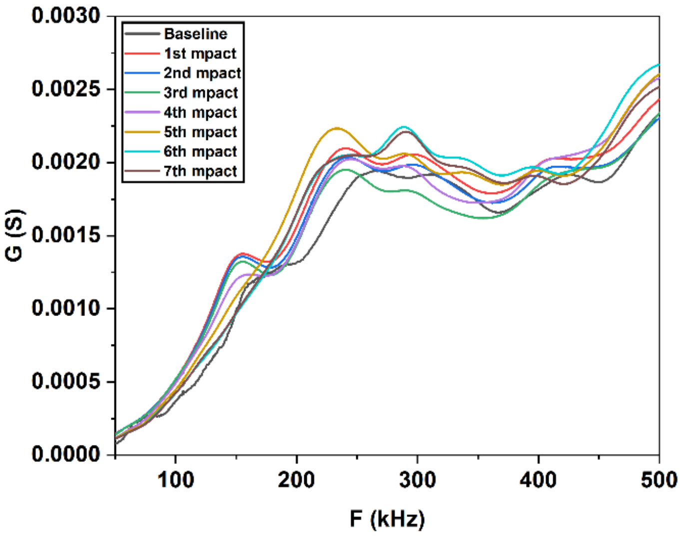

Figure 3. 57 Non-compensated signature at 100 ºC temperature from baseline to failure

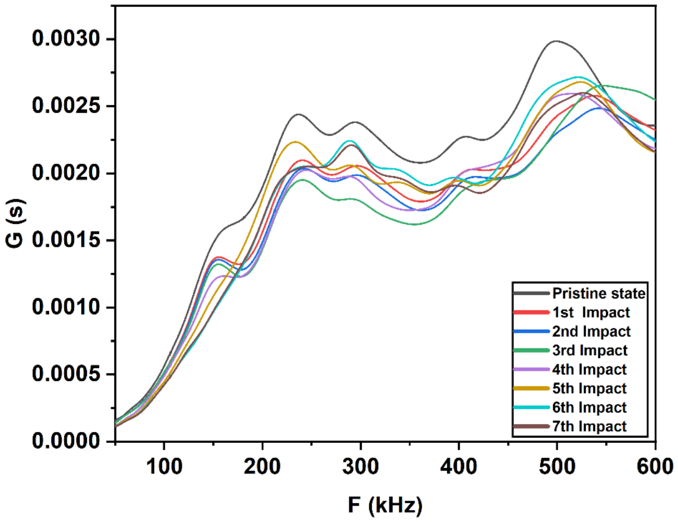

Figure 3. 58 Compensated signature at 100 ºC temperature from baseline to failure

3.13.4 RMSD of the Compensated Signature

The RMSD index after compensation has been obtained as shown in Figure 3. 59. It has been noted that there is an increasing trend in the values of the RMSD index following temperature compensation. If the admittance signatures have not been compensated, there could be a false warning about damage.

3.14 Summary

This study uses the EMI technique to demonstrate the feasibility of three different types of piezo sensor configurations for detecting damage in concrete under the effect of impact loading at varying temperatures. The conclusions discussed here are based on the above-mentioned experimental results.

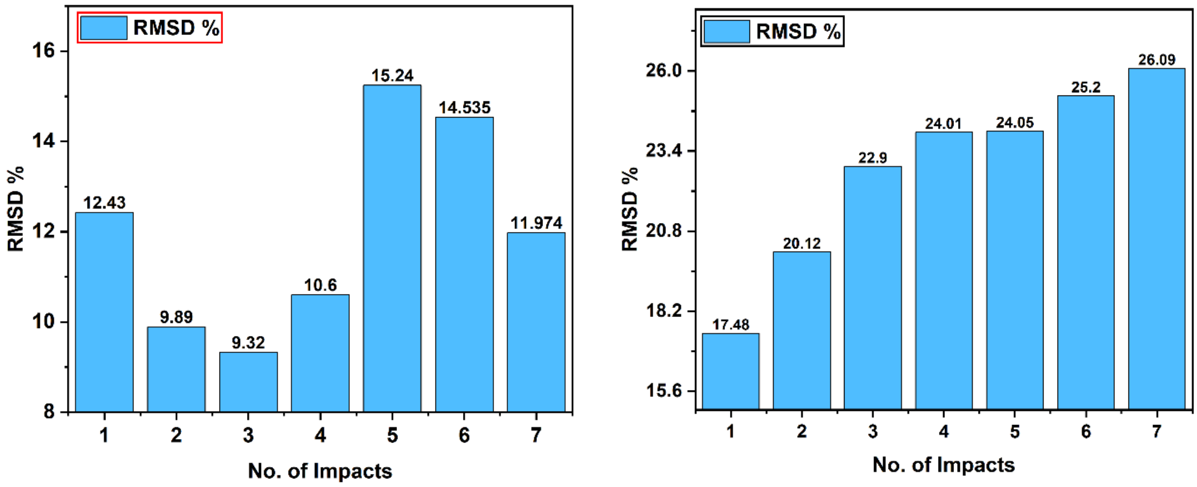

(a) **(b)**

Figure 3. 59 RMSD index before and after compensation a) RMSD at 100 ^{o}C for JKTPS at 3 m impact before compensation b) RMSD at 100 ^{o}C for JKTPS at 3m impact after compensation

Based on the evaluation of the RMSD and MAPD values both are the reliable statistical tool for calculating the incipient and progressive damage in concrete under the effect of impact loading at varying temperatures. Due to its lack of direct contact with the host structure, the NBPS recorded lower RMSD and MAPD values than the SBPS and JKTPS for all temperature cases. Both the RMSD and MAPD indices followed a distinct pattern at higher temperatures of 150 ^{o}C for all sensor configurations, whereas MAPD values followed a more consistent pattern than RMSD values.

The resonant frequency and peak conductance exhibited an inverse relationship with increasing impact load, and this relationship was maintained at higher temperatures. The extracted equivalent stiffness with increasing impact number clearly indicates damage propagation in concrete sample for different sensor configuration (10.42 % loss for JKTPS) and also showed satisfactory agreement between the experimental and equivalent plot of x and y. Esps were used to successfully develop an empirical model for predicting the remaining life of structures. This model was created by analyzing the obtained data under the best-fit curve, and it shows that the remaining life of the structure decreases as the loss of equivalent stiffness increases. All three sensor configurations, JKTPS, SBPS, and NBPS, perform well in predicting damage when impact and temperature are combined. Although piezo sensors have a very high sensing behaviour against temperature, the JKTPS performed well with the fewest false alarms when compared to the SBPS and NBPS.

Chapter 4: EXPERIMENTAL INVESTIGATION ON STRUCTURAL BEAM AND EFFECT OF BOUNDARY CONDITION

4.1 Introduction

Chapter 4 delves into the practical implementation and experimental investigation of the proposed monitoring technique using JKTPS sensors configuration in concrete beam structures which is the best suitable sensors concluded in chapter 3. Building upon the theoretical framework and literature review presented in the previous chapters, this chapter aims to validate the effectiveness and reliability of the electromechanical impedance (EMI) based approach for monitoring concrete structural element properties and its behaviour. In this chapter, the detailed setup of the experimental tests conducted on concrete beam elements, each equipped with JKTPS sensors has been discussed. The specimens were subjected to various impact and temperature loading conditions, simulating real-life scenarios to assess the performance and capabilities of the proposed monitoring system. The experimental investigation includes the detection of potential damage or structural changes of concrete under the individual effect of impact and temperature and also the combined effect of impact and temperature. By using the EMI techniques, signatures obtained from the JKTPS PZT sensors were analysed in the form of conductance and susceptance parameters. These obtained signatures were further analysed by using different parameters such as concrete mechanical properties by using the equivalent based parameters such as mass, stiffness and damping. Additionally, the behaviour of concrete specimens subjected to fixed boundary conditions, considering the combined influence of impacts and temperature has been investigated. The raw signatures from these specimens have been extracted and then proceed to compare these raw signatures with the damage state signatures, represented as conductance and susceptance data. Furthermore, these extracted signature were further analysed for the mass, stiffness and damping parameters of the specimen. The results obtained from the experiments have been critically analysed, and the efficacy of the proposed approach is thoroughly evaluated. Overall, Chapter 4 serves as a crucial component in validating the proposed EMI-based monitoring method and provides valuable insights into the feasibility and potential applications in the real time structural beam element. The outcomes of this experimental investigation will contribute significantly to the advancement of non-destructive evaluation techniques for concrete health monitoring and structural assessment.

4.2 Preparation of Reinforced Concrete Beam Specimen

In this investigative study, 12 concrete Beam of grade M30 (As per IS 456: 2000), 150 x 150 x 700 mm, were cast using the mix design ratio 1:1.78:3.315 (C: FA: CA). The concrete beam specimen were cast using ordinary Portland cement (OPC) of grade 43 with the fine aggregate of grade of Zone 1 (as per Table 4, IS 383, 1970) with the 20 mm maximum nominal size of aggregate, angular in shape and the PCE (Polycarboxylic Ester) based AURAMIX 400 admixture. The detailed composition of concrete mix have shown in Table 4. 1.

Table 4. 1 Detailed composition of concrete mix

Parameters	Units	Quantity
Cement(OPC of grade 43)	Kg/m^3	372.5
Coarse aggregate	Kg/m^3	1235
Fine aggregate	Kg/m^3	665.7
Slump	mm	50
Water cement ratio	-	0.4
Superplasticizer	Kg/m^3	7

The reinforcement layout for the concrete beam included 8 mm diameter bars as the primary reinforcement and 6 mm diameter bar stirrups spaced at 75 mm centre to centre, as illustrated in Figure 4. 1.

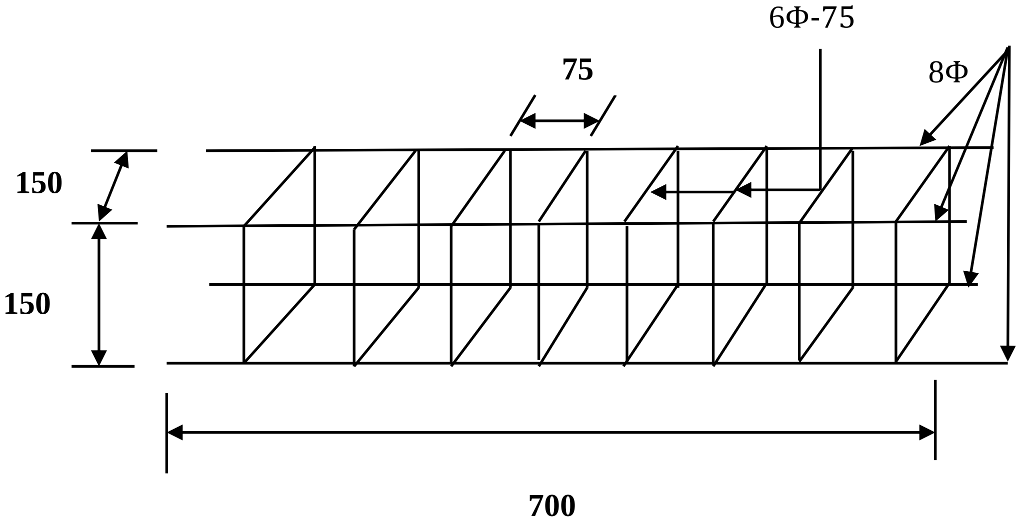

Figure 4. 1 Detailing of the reinforcement

The standard size of moulds were filled in three layer, firstly filled the concrete with the clear cover of 25 mm from the bottom side. Reinforcement are placed, then the half of the beam mould was placed with the concrete and after placing the jacketed sensors (JKTPS) as shown in Figure 4. 2 remaining half portion was again filled with concrete with the proper compaction using vibrating table and proper precautions were taken in pouring the concrete to avoid the damage of the JKTPS type piezo sensors.

Figure 4. 2 Placing of the JKTPS sensors

All the prepared sample were placed for jute bag curing for 28 days and after the curing was completed, all the specimen were tested.

4.3 Experimental Details and Procedure

In the experimental study, the damage was detected in the reference of baseline data, prior to testing the beam, baseline data were collected from the JKTPS sensors from each beam in the form of conductance *(G) vs* frequency *(F)* and susceptance *(S) vs* frequency *(F)* under free-free boundary condition (FFBC). All the signatures have been collected in the frequency ranges of 50 kHz to 600 kHz. PZT typically has an exciting range of 30 to 600 kHz as recommended by (Park et al. 2003)(Sun et al. 1995), as the frequencies higher than the 500 kHz are found to be unfavorable because they make the sensing region of the PZT patch too small. The *G* and *B* signatures are acquired using Keysight precision LCR meter E49800A , which has a frequency range of 20 Hz to 2 MHz (Keysight (Agilent) Technologies 2014). Keysight's VEE Pro software was used to control the frequency step. By applying 1 V of voltage across the terminals of the PZT patch, all signatures were recorded at the 100 Hz frequency step. First, admittance signatures for the beam were obtained as a baseline signature from the JKTPS sensors as shown in Figure 4. 3 and then beam was then subjected to three different temperatures, ranging from 50 °C, 100 °C and 150 °C. Beam were heated in oven for 120 minutes then cooled for 60 minutes at room temperature. Furthermore, cooled beam samples were tested at impact heights of 3 m, and signatures were recorded after each impact up to failure.The complete description of the parameter used in the experimental study is shown in Table 4. 2

Table 4. 2 Description of the parameter used in the experimental study

S.No.	Parameter	Description
1	Type of sensors configuration	Embedded
2	Impact height	3 m
3	Impactor size and type	Steel ball with 13 cm diameter
4	Temperature variation	Ambient, 50^{o}C, 100^{o}C and 150^{o}C
5	Boundary condition	Free (Fixed at base)
6	Instruments	LCR meter, oscilloscope, guided pipe
7	Grade of concrete	M30

Figure 4. 3 Complete setup for calculating the baseline data

The complete methodology used in this study is shown in Figure 4. 4. It begins with the fabrication of the JKTPS sensors their installation on the concrete beam, reinforcement detailing, baseline signature extraction and the application of temperature and impact loading, and subsequent analysis and monitoring of the analysis of the raw signature data using various parameters to identify the damage in the concrete beam.

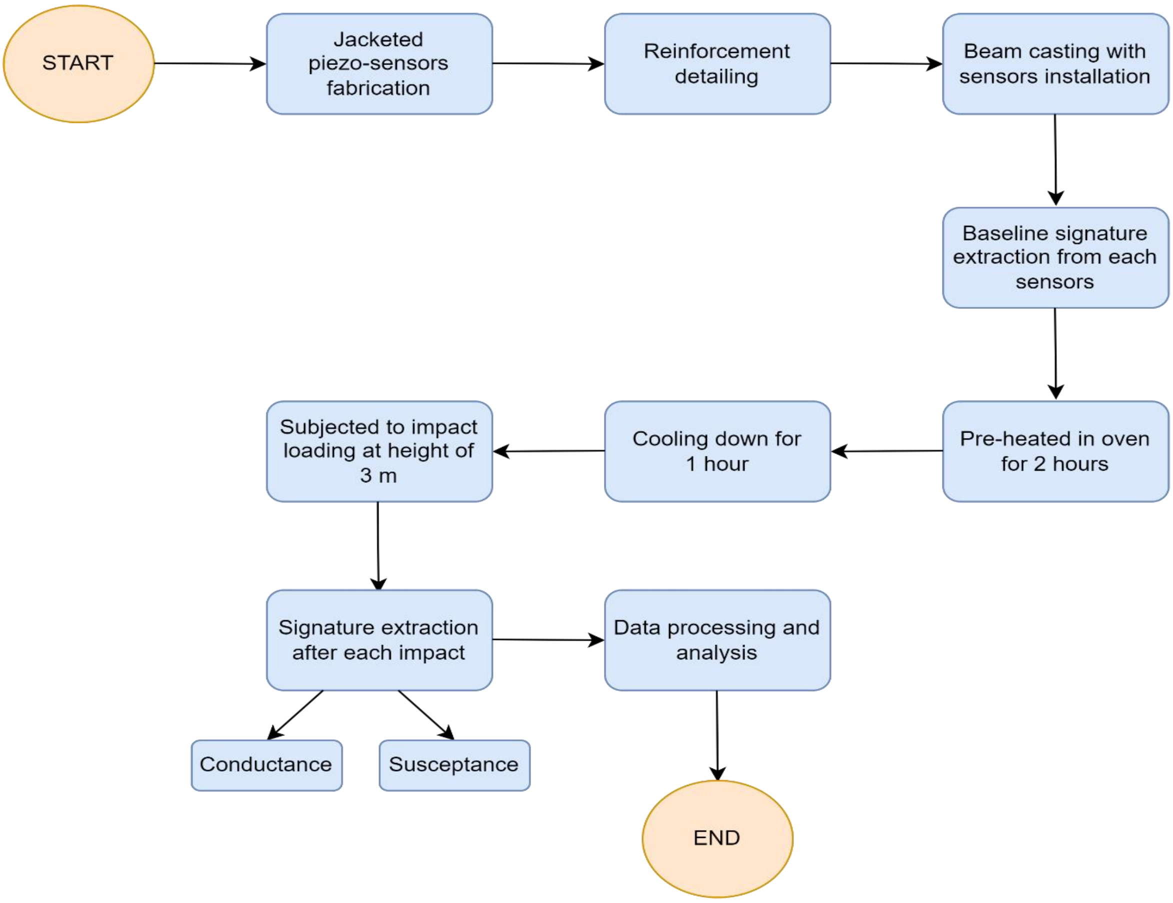

Figure 4. 4 Methodology adopted in the study

4.4 Physical Assessment of Concrete Beam after Each Impact

All of the concrete beams were physically inspected in order to study the initiation and propagation of crack patterns under impact loading at varying temperatures. The initiation and propagation of a crack pattern in atypical concrete beam under 3 m impact height is shown in Figure 4. 5, beams were heated at the temperature of 100 °C. Concrete beam under 3 m height of impact is completely fails after 15th impact, as the number of impact increase the energy absorption capacity of the beam increases which is responsible for the complete failure of the beam at higher impact.

1st impact **5th impact**

10th impact **15th impact**

Figure 4. 5 the initiation and propagation of a crack pattern in concrete beam

4.5 Damage Assessment Using Emi Technique

The admittance signature has been acquired from the JKTPS sensors using an impedance measurement device (LCR meter). The variation of the conductance signature has the main importance in identifying the change in damage state of the structure (change in mass, damping and stiffness). The susceptance signature identified the integrity of the JKTPS sensors; by monitoring the susceptance signature, the sensors' breakage and quality degradation can be identified. Figure 4. 6 (a) and (d) shows the variation in the conductance *(G)* signature versus frequency *(F)* under the 3 m impact height for the temperature variation of ambient to 150°C. Figure 4. 6 (a) depicts the variation in G versus F at ambient temperature; when the baseline signatures were compared to the signatures after each impact, it was found that the signatures shifted downward with the increase in the number of impacts, indicating the propagation of damage in the concrete beam as the number of impacts increased. The variation in G vs F at 50 °C temperature is shown in Figure 4. 6 (b). When compared to the baseline signatures, the signatures was first shifted higher after the first impact and then all of the signatures were shifted lower after additional impact loads. Figure 4. 6 (c) depicts the variation in G versus F at 100 °C temperature; when the baseline signatures were compared to the signatures after each impact, it was found that the signatures was first shifted higher after the first impact and then all of the signatures were shifted lower after additional impact loads, indicating the propagation of damage in the concrete beam as the number of impacts increased. Figure 4. 6 (d) depicts the variation in G versus F at 150 °C temperature; when the baseline signatures were compared to the signatures after each impact, it was found that the signatures was first shifted higher after the first impact and then all of the signatures were shifted lower after additional impact loads as same as the 50 and 100 ^{o}C temperatures.

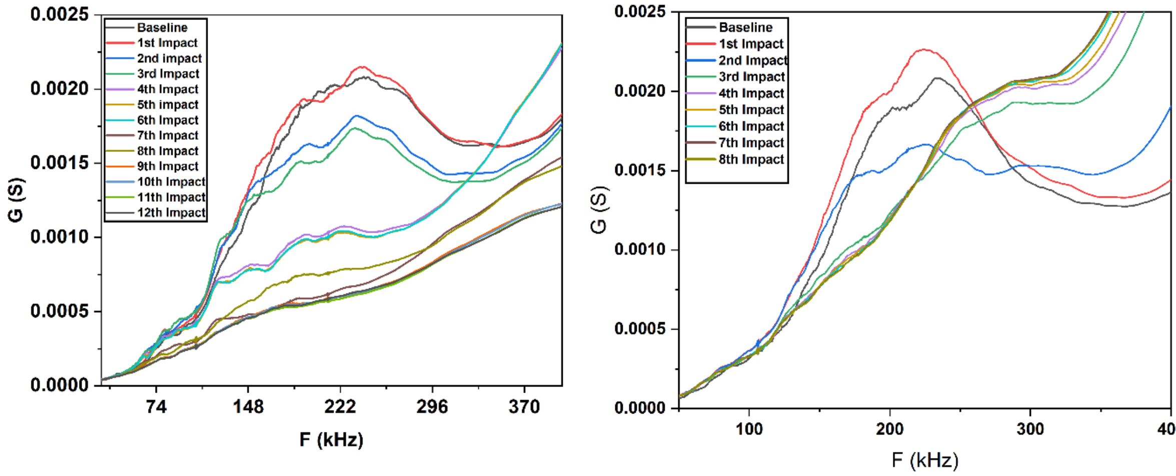

(a) ambient (b) 50 ^{o}C

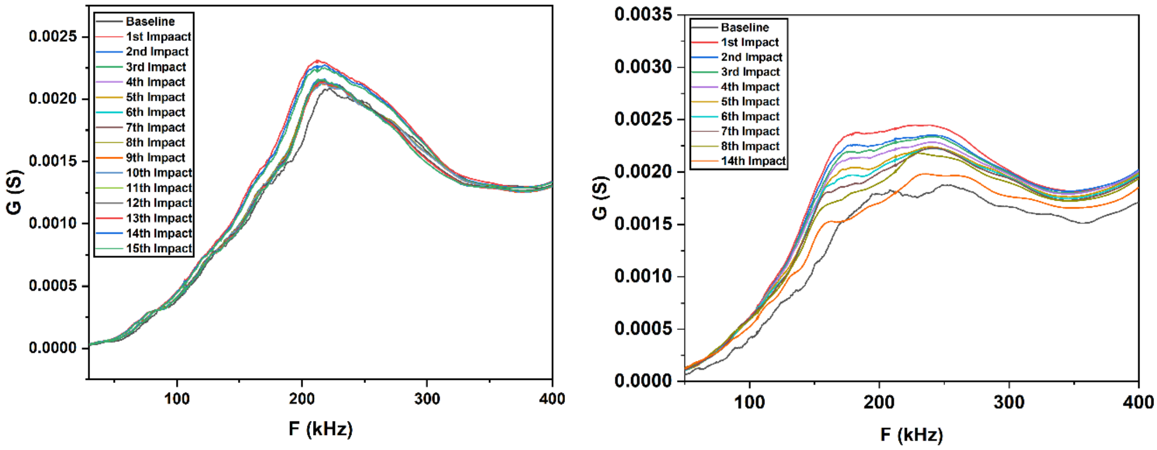

(c) 100 ^{o}C (d) 150 ^{o}C

Figure 4. 6 Variation in the conductance *(G)* signature versus frequency *(F)* under the 3 m impact height for the temperature variation of ambient to 150 ^{o}C a) Ambient b) 50 ^{o}C c) 100 ^{o}C d) 150 ^{o}C

Susceptance *(B) vs* Frequency *(F)* with increasing damage under 3 m impact loading for beam at ambient to 150 ^{o}C as shown in Figure 4. 7 (a) – (d). In comparison to the conductance signature, the suseptance signature shows a flat line with no peak and increasing upward, indicating that the sensors were not broken during the experiment.

Furthermore, baseline signatures were compared to the signatures after each impact, for both the case of beam and cube. A typical example for the comparison of the conductance signature for 150 ^{o}C temperature under 3 m impact height as shown in Figure 4. 8 (a) - (b). For both the beam and cube signatures was first shifted higher after the first impact and then all of the signatures were shifted lower after additional impact loads, as shown in Figure 4. 8 (a) - (b), the shifting of the signature for both the case of cube and beam followed the same pattern.

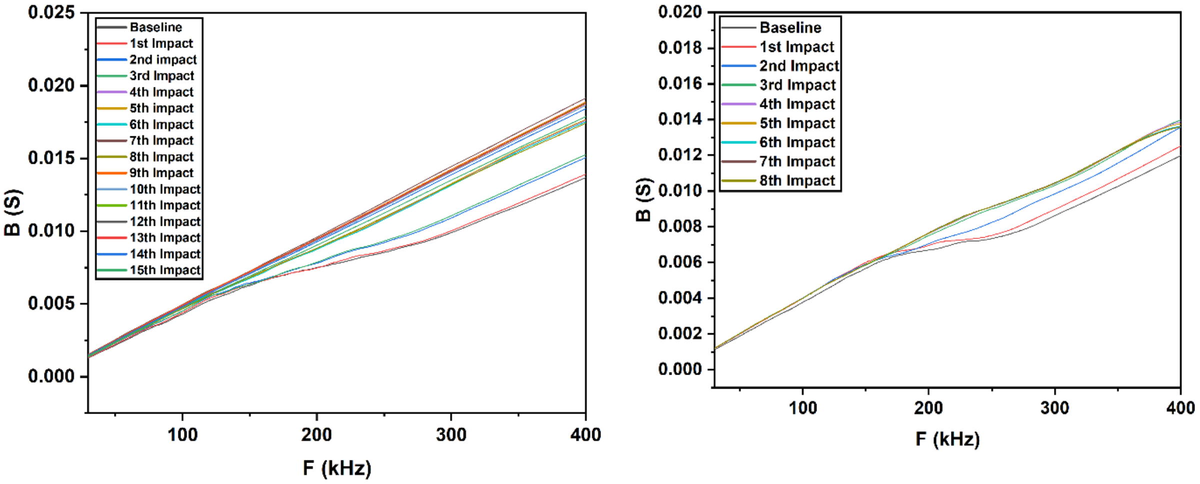

(a) ambient (b) 50°C

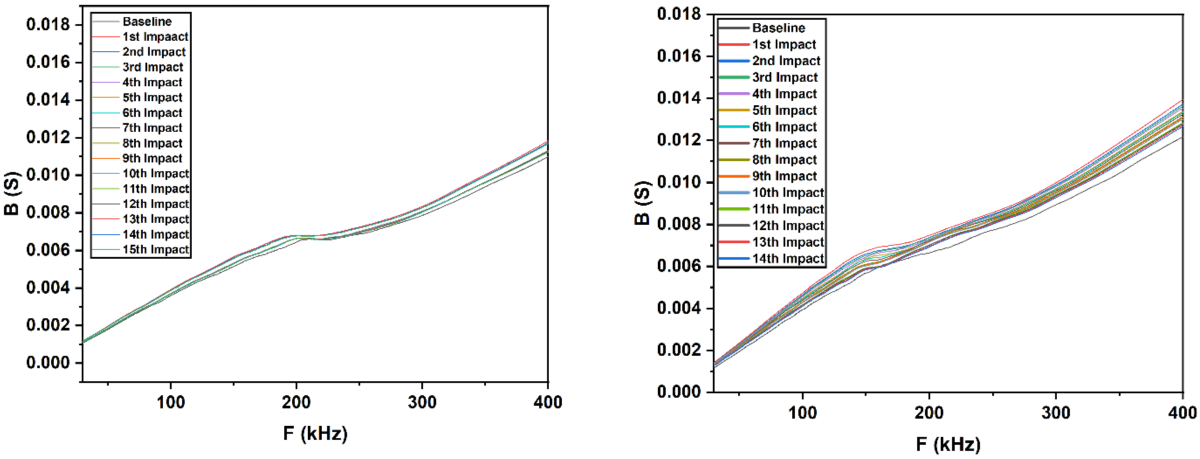

(c) 100 °C (d) 150 °C

Figure 4. 7 Susceptance *(B) vs* Frequency *(F)* with increasing damage under 3 m impact loading for beam at ambient to 150 °C a) Ambient b) 50°C c) 100°C d) 150°C.

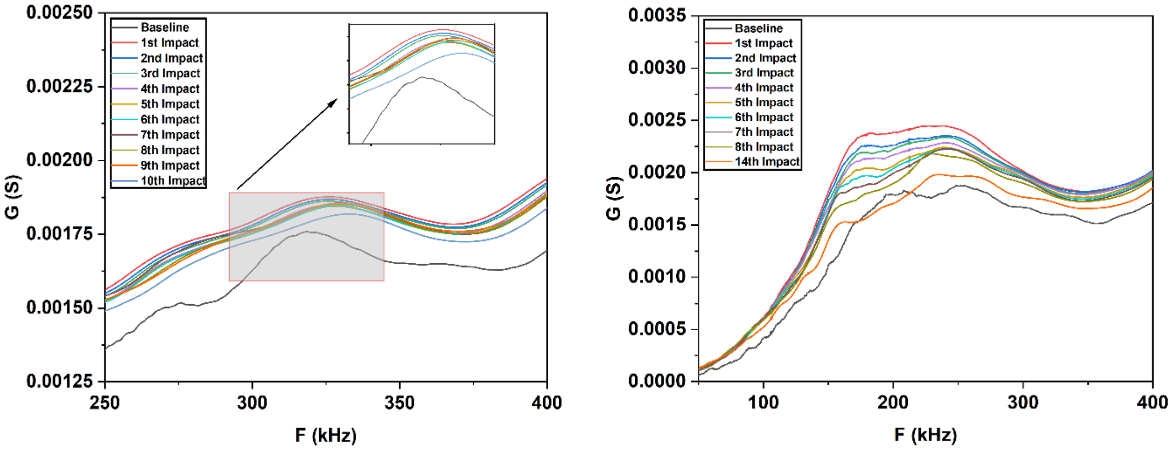

(a) Cube Specimen (b) beam specimen

Figure 4. 8 Conductance signature for 150 °C temperature under 3m impact height a) Cube b) Beam

4.6 Analysis Based On Equivalent Based Parameter

Soh and Bhalla (2005) derive the mechanical impedance (Zs,eff=x+yj) for the monitored structure at a specific frequency (ω=2πf). In this analysis for all cases of impact loading under temperature variation, signatures consisting of G and B plots are retrieved in the frequency range of 50 kHz-500 kHz, plot the graph of experimental plots in between x in the function of *f* and *y* in the function of *f*. Again, the experimental plots of *x* and *y* were compared to the Hixon equivalent system model. Figure 4. 9 and Figure 4. 10 represents the experimental plot of *x* and *y* with the frequency respectively at incremental damage state under the 3 m height of impact for JKTPS for 50 ^{o}C and 150 ^{o}C temperature. After examining the graphs of *x* in function of *f* and *y* in function of *f* through the equivalent plot, a dashpot(c), spring (k), and mass (m) equivalent system in series as depicted in Figure 4. 10 (b) were found to be similar.

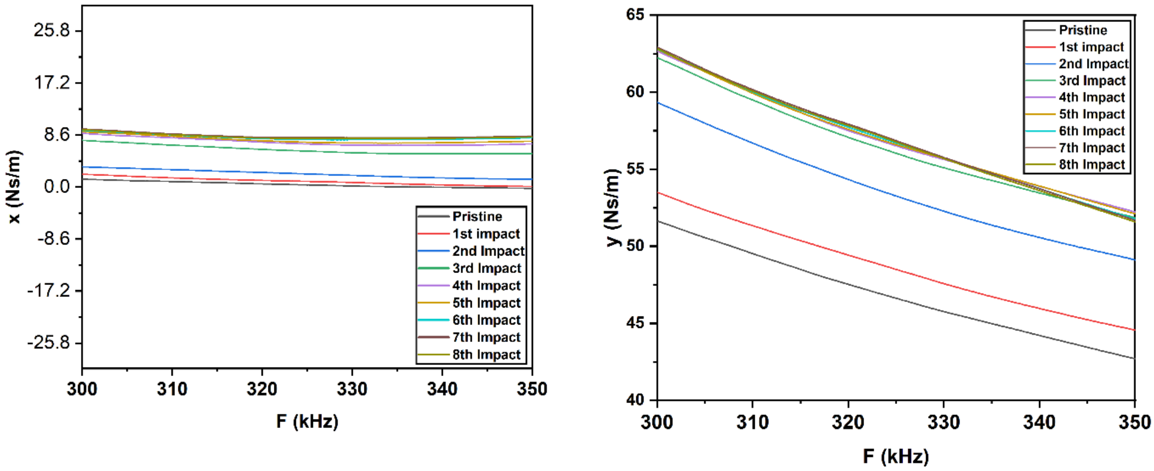

(a) (b)

Figure 4. 9 Experimental plot of x and y with the frequency respectively at incremental damage state under the 3 m height of impact for JKTPS at 50 ^{o}C

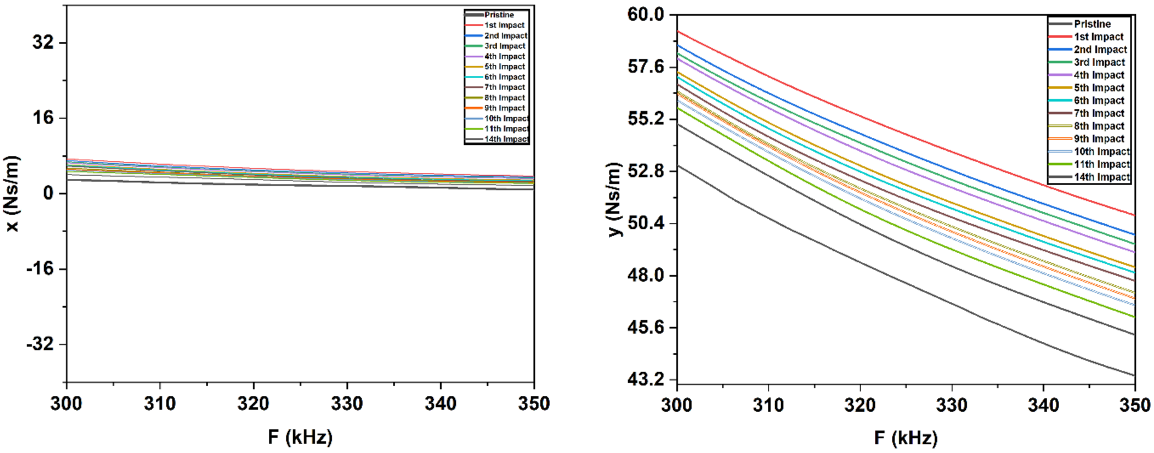

(a) (b)

Figure 4. 10 Experimental plot of x and y with the frequency respectively at incremental damage state under the 3 m height of impact for JKTPS at 150 ^{o}C

Figure 4. 11 illustrates the typical frequency-dependent variations of x and y within the identified series m-c-k system. The ESPs values were obtained using experimental x and y values within the frequency range, which were then entered into the Equations 4.1, 4.2 and 4.3 to calculate the m-c-k values. These absolute values of m-c-k are derived by rearranging the Equations 4.4 and 4.5 with some boundary conditions.

$$m = \frac{({\omega_o}^2-\omega^2)(x^2+y^2)}{\omega{\omega_o}^2 y} \tag{4.1}$$

$$k = \frac{({\omega_o}^2-\omega^2)(x^2+y^2)}{\omega y} \tag{4.2}$$

$$c = \frac{(x^2+y^2)}{x} \tag{4.3}$$

Where $\omega = \omega_o$ at $y = 0$. This Solution is valid for $y>0$ and $|\omega| < \omega_o$ or $y<0$ and $|\omega| > \omega_o$.After determining the average values of the m-c-k, the equivalent values of x and y are calculated using Equations 4.4 and 4.5.

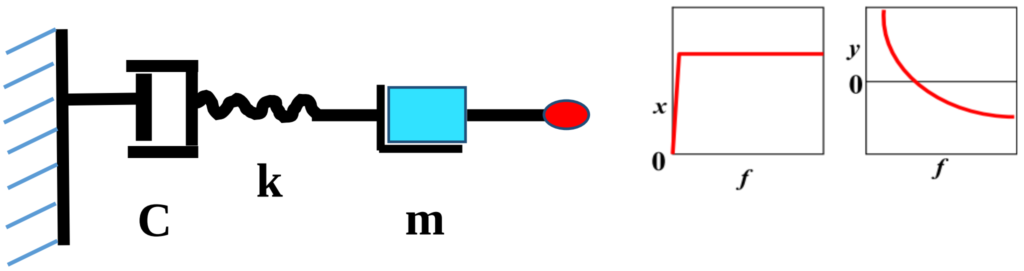

(a) (b)

Figure 4. 11 (a) Equivalent mechanical system consist of spring, mass and damper in series (b) Variations in x and y for the determined series m-c-k system

$$x = \frac{c^{-1}}{c^{-2}+\left(\frac{\omega}{k}-\frac{1}{\omega m}\right)^2} \tag{4.4}$$

$$y = \frac{-\left(\frac{\omega}{k} - \frac{1}{\omega m}\right)^2}{c^{-2} + \left(\frac{\omega}{k} - \frac{1}{\omega m}\right)^2} \qquad \textbf{4.5}$$

After comparing the experimental and analytical impedance plots, as depicted in Figure 4. 11 (b), a similar system, composed of a series arrangement of spring-mass damping (k-m-c) components operating within the frequency range of 210-280 kHz, was selected for assessing the Equivalent stiffness Parameters (ESPs). Figure 4. 12 demonstrates the satisfactory agreement between the experimental and corresponding plots of x and y, obtained for the JKTPS at a temperature of 150 °C.

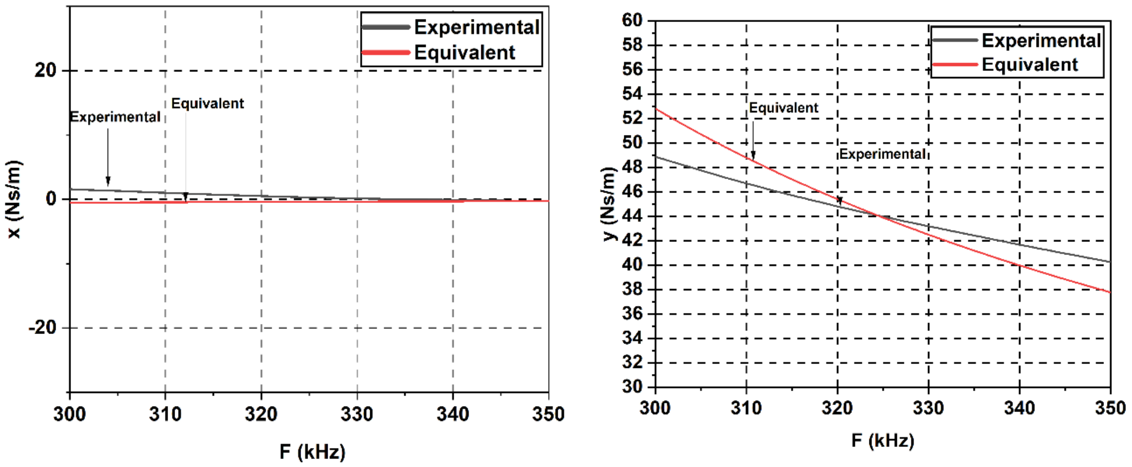

(a) (b)

Figure 4. 12 Experimental and equivalent plots of x and y extracted for the JKTPS at 150 °C temperature.

Figure 4. 13 depicts the variation of the Equivalent stiffness value with the number of impacts for various sensor configurations under 150 °C temperature. Equivalent stiffness values follow the same pattern for JKTPS sensor as the number of impacts increases. Except for pristine to first impact, the equivalent stiffness value decreased as the number of impacts increased up to failure, the decrease of the equivalent stiffness value with the increasing impacts indicates the increase in damage in the sample. The value of the increasing damage was due to the loss of its strength and the value of increasing stiffness for the first impact was due to the PZT's high-temperature sensitivity.

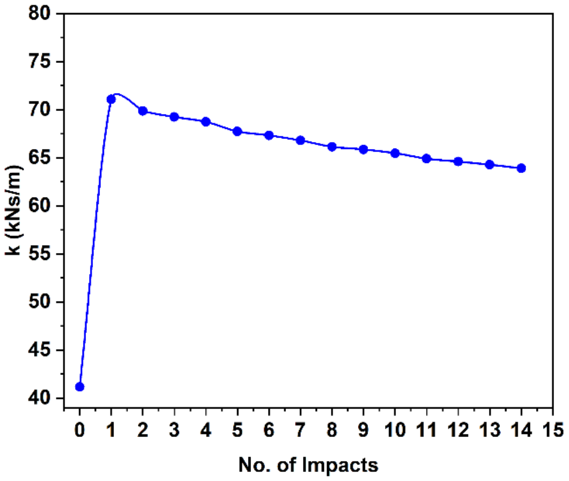

Figure 4. 13 Variation of Equivalent Stiffness at 150 ^{o}C for JKTPS

4.7 Effect of Fixed Boundary Conditions

The examination of fixed boundary conditions is of great significance because these conditions are commonly encountered in the construction of concrete building structures. The majority of concrete structures used in buildings are subject to fixed boundary conditions, where certain parts of the structure are firmly anchored or restrained in place. In contrast, the preceding section of Chapter 3 was dedicated to the discussion of free-free boundary conditions, which are more commonly found in industries like aerospace and maritime, where structures often have greater degrees of freedom to move. Damage detection in concrete cubes was tested again using JKTPS under fixed boundary conditions (FBC) for impact height of 3 m at each temperature condition ranging from ambient to 150 ^{o}C.

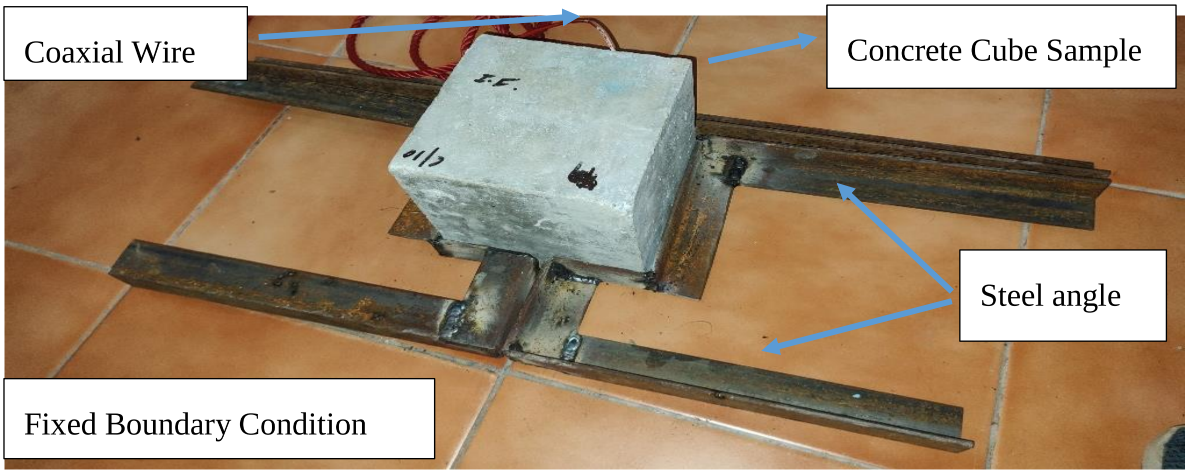

Figure 4. 14 Configuration of the steel angle used for FBC

The JKTPS sensors was adopted for FBC because JKTPS provided accurate results as concluded in Chapter 3 and the same is also concluded by Bansal et al. (2022). Figure 4. 14 presents an illustration of the specific configuration of the steel angle used to fix the concrete cube sample from the each side for applying the FBC. The complete setup for application of impact load under the FBC condition is shown in Figure 4. 15.

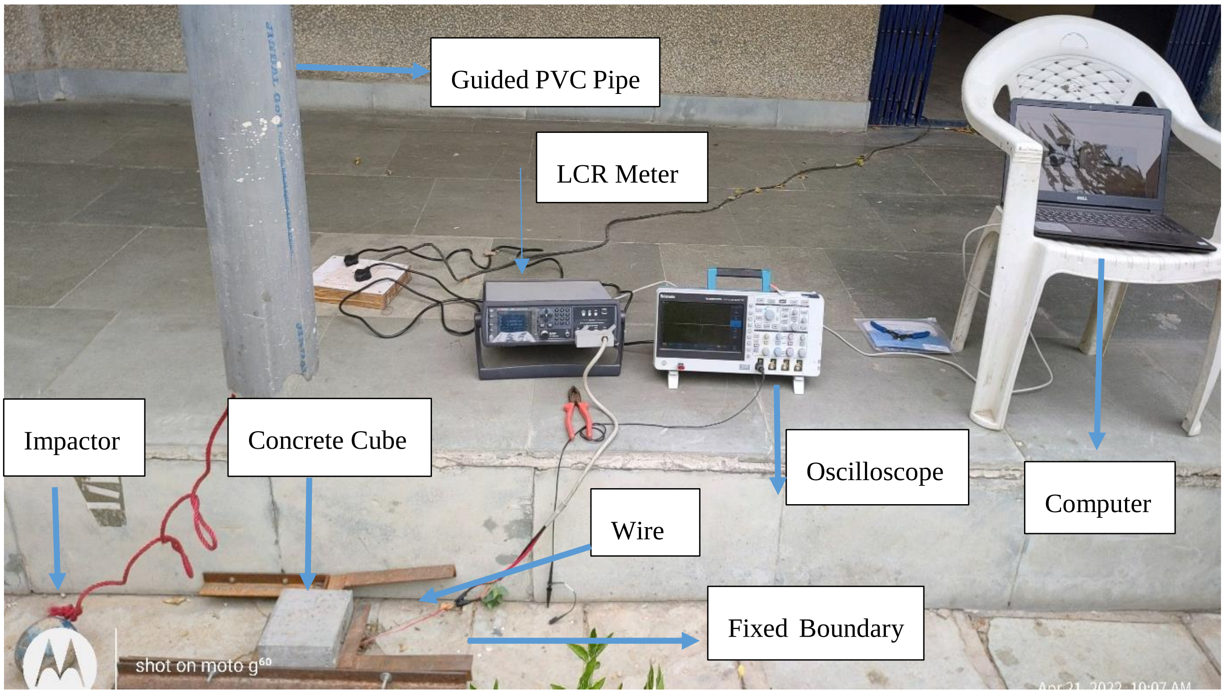

Figure 4. 15 Complete setup for application of impact load under the FBC

4.7.1 Physical Assessment of Concrete Sample for FBC

After each impact at height of 3m, all of the concrete cubes were physically inspected in order to study the initiation and propagation of crack patterns at three different varying temperatures of 50, 100, and 150 ^{o}C. Figure 4. 16 shows the damage behaviour of a typical concrete cube at 100 ^{o}C temperature from the beginning to the end of the failure process.

Cracks were first initiated on the top surface of the concrete cube just after the first impact, and these cracks are easily observed by the necked eye. When compared to the Free-Free boundary condition (FFBC) at 100 ^{o}C, no visible cracks were observed on the top surface of the concrete cube after the first impact, because the FBC conserved more energy than the FFBC. With the increase in the number of impacts, cracks become wider, and crack propagation occurs from the top surface to the side faces as well.

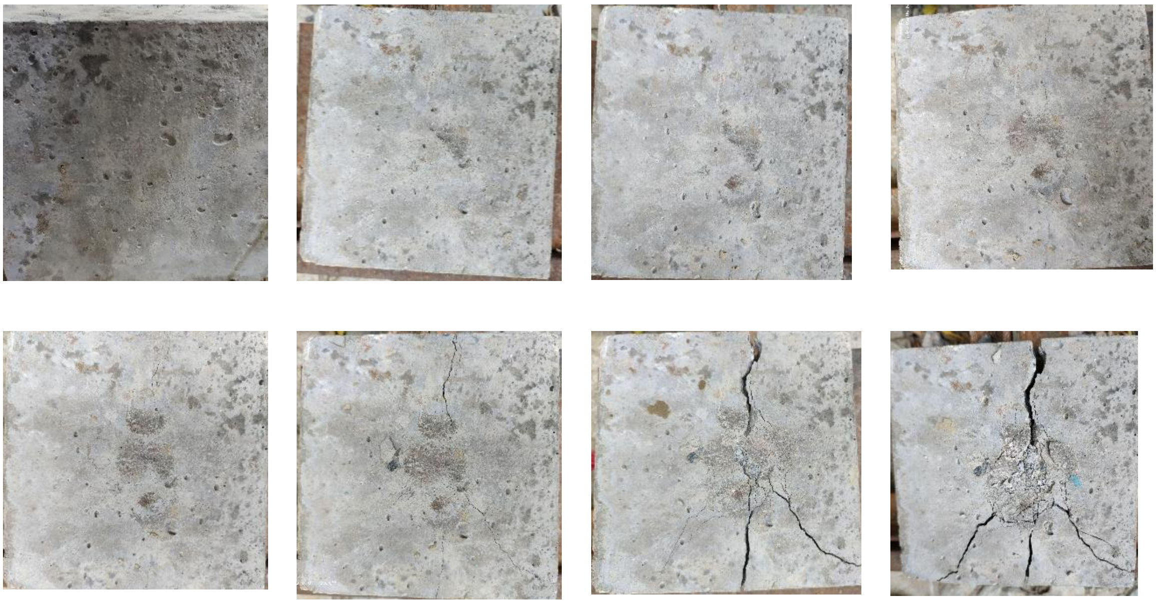

Figure 4. 16 Development of Crack and its progress in cube for 3m impact height at 100 ^{o}C temperature under FBC

4.7.2 Quantification of Signatures Using Voltage Time Histories under Boundary Condition

Absolute peak voltage was calculated for JKTPS sensors at various temperatures and impact heights of 3m up to failure under the FBC. Furthermore, the extracted value of *Vp* was used to analyze damage and calculate strain values for free-free and fixed boundary conditions. Peak voltage (*Vp)* recorded for four typical JKTPS sensors for the FBC and then compare it to the previous record *Vp* with FFBC. Furthermore, the resultant maximum strain value (*Sp*) corresponding to each *Vp* was calculated using Equation 3.3 and comparing the FFBC *Sp* value. Table 4. 3 shows the *Vp* and *Sp* values for JKTPS under FFBC and FBC at various temperatures variations ranging from ambient to 150 ^{o}C. The value of *Vp* is getting more under FBC as compare to the FFBC, this is due to the more confinement of the cube sample in FBC. Due to the cube confinement under the FBC, more energy was absorbed at time of impact resulting in higher strain.

Table 4. 4 shows the typical four-cube configuration for JKTPS along with the number of impacts that can be sustained up until failure while operating at different temperatures for FBC and also the peak voltage value following the first impact. Furthermore, the peak voltage value after the first impact was used for validation in the chapter 5 of numerical modelling section.

Table 4. 3 Strain value for FFBC and FBC for JKTPS at 3m height of impact

Temperature condition	*Vp* value for FFBC (V)	*Sp* value for FFBC x (10^{-6})	*Vp* value for FBC (V)	*Sp* value for FBC x (10^{-6})
ambient	0.10	0.473	4.80	22.60
50°C	3.01	14.20	4.50	21.20
100°C	17.11	80.50	-	-
150°C	2.50	11.80	6.05	28.50

Table 4. 4 Cube configuration with the total number of impact up to failure and value of peak voltage after first impact for FBC

S.No.	Type of Sensors	Impact Height	Temperature	Total number of impact	Cube representation No.	Peak voltage after 1st impact
1	Embedded(JKTPS)	3m	Ambient	8	7/5	1.5
			50°C	10	7/4	0.3
			100°C	7	6/4	-
			150°C	6	6/3	0.5

4.7.3 Extraction of Signatures under FBC

The admittance signatures in the form of conductance (G) and susceptance (B) were extracted from each cubes under the FBC at temperatures of ambient, 50 °C, 100 °C and 150 °C, and the graphs of *G vs f* and *B vs f* are plotted as shown in Figure 4. 17 (a) - (d). Under ambient temperature conditions, the baseline signature for all concrete cubes was obtained from the JKTPS sensors embedded in the cube, and the signatures of the damage state were compared after each impact at different temperatures. Figure 4. 17 (a) shows the *G vs F* variation for the JKTPS sensor in the 30 kHz to 600 kHz frequency range at ambient temperature with increasing damage under the 3 m height of impact loading. From the Figure 4. 17 (a), it is observed that the signatures in the frequency range of 475 to 525 kHz are shifting in the upward direction with the increase in number of impact. It’s clearly shows that the signatures are highly sensitivity towards the damages, as the damage induced in the concrete increase the variation of the signature from the baseline was also increased.

Figure 4. 17 (b)-(d) depicts a graph of *G vs f* for temperatures ranging from 50 to 100 °C, in which the signature shifts upward for the first impact after 2 hours of heating and 1 hour of cooling, and shifts downward for subsequent impacts due to the piezo sensors' high sensitivity

to temperature. All of the signatures extracted using the FBC follow the same pattern as the FFBC as shown in Figure 4. 18.

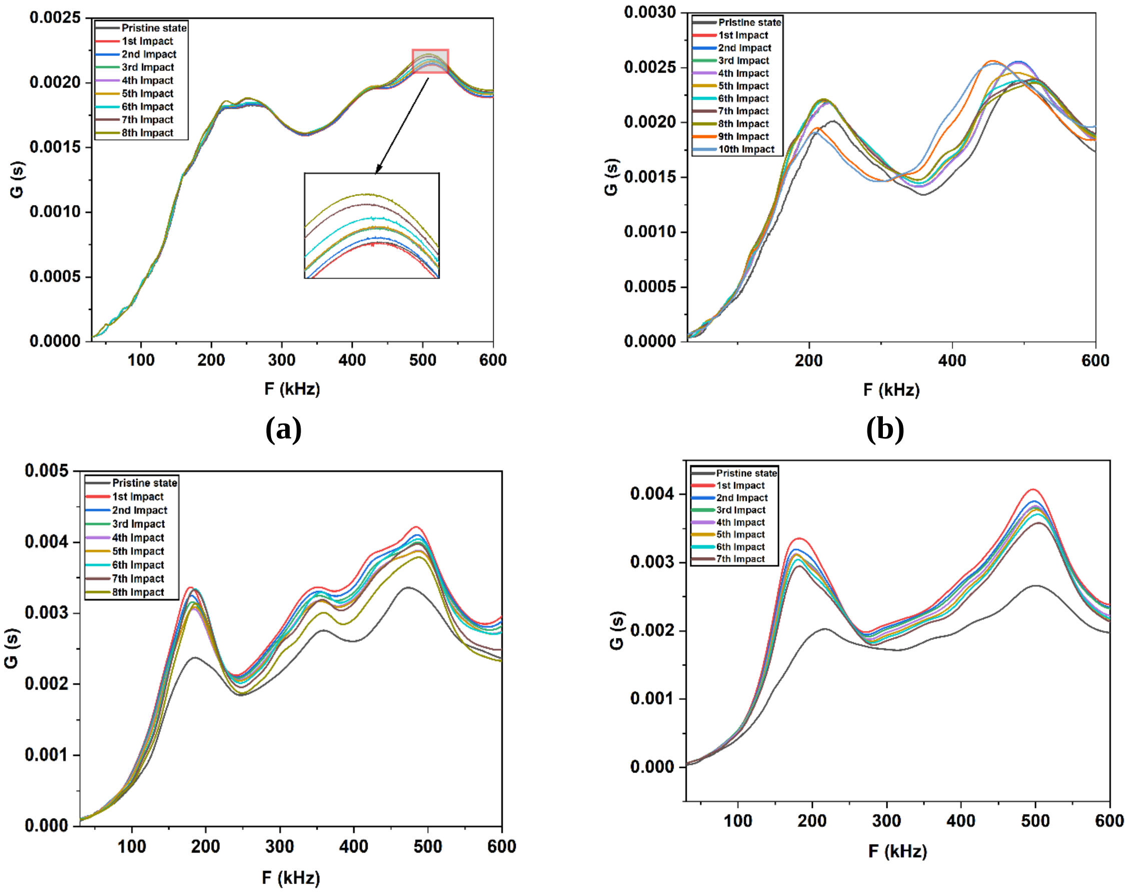

(a) (b)

(c) (d)

Figure 4. 17 Admittance signature for FBC at 3m height of impact under varying temperature a) G vs f for Cube number 7/5 at ambient temperature b) G vs f for Cube number 7/4 at 50 ºC temperature c) G vs f for Cube number 6/4 at 100 ºC temperature d) G vs f for cube number 6/3 at 150 ºC temperature

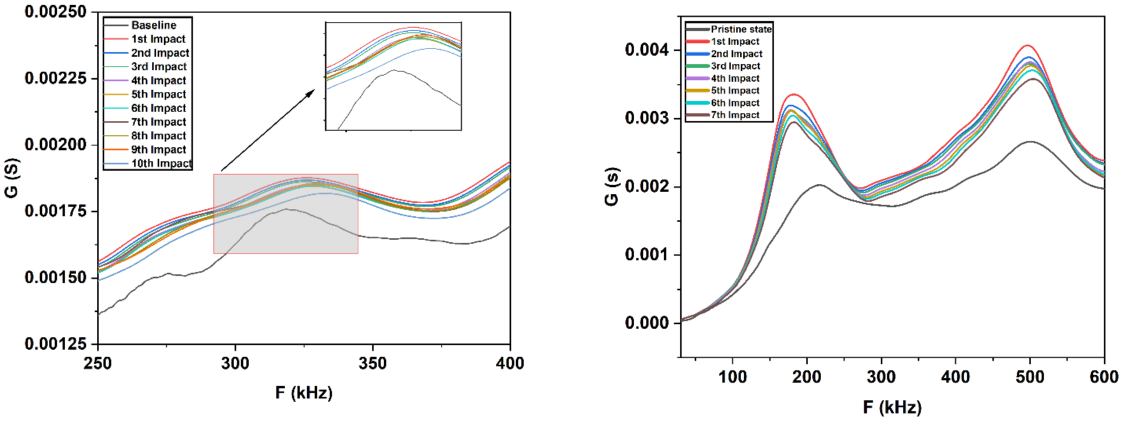

(a) (b)

Figure 4. 18 Compression of Admittance signature for FFBC and FBC at 3m height of impact under varying temperature for JKTPS sensors a) G vs f for Cube at 150 ºC temperature for FFBC b) G vs f for Cube at 150 ºC temperature for FBC

4.8 Summary

Chapter 4 of "Experimental Investigation on Structural Beam and Concrete under Boundary Condition" delves into the empirical study conducted on structural beams and concrete subjected to specific boundary conditions. The primary focus of this chapter is to present the experimental findings and observations related to the behaviour of beam structural member under the combined effect of impact and temperature using JKTPS sensors. A detailed description of the experimental setup used to subject the structural beams under impact and temperature load and concrete specimens to specific boundary conditions was discussed briefly. Discussion of the fixed boundary conditions applied to the specimens and the rationale behind selecting these conditions. An exploration of how the combination of impacts and varying temperatures affects the structural integrity and behaviour of the materials. Explanation of the techniques and methods used to extract relevant data, such as raw signatures from the specimens. An analysis of the raw signatures extracted and their comparison with signatures representing the damage state, which are typically expressed in terms of conductance and susceptance data. Furthermore these extracted conductance and suseptance data was further analysed in terms of structural parameter mass damping and stiffness for the better understanding of the damage condition in the structural element. The suseptance signature patterns clearly demonstrate that the JKTPS are intact, post failure of the beam that clearly shows that the JKTPS could be extremely beneficial not only for detecting initial damage but for damage induced till failure in the beam. The extracted equivalent stiffness with increasing impact number followed a distinct decreasing pattern (stiffness loss up to 15%) that clearly indicates damage propagation in concrete beam and also showed satisfactory agreement between the experimental and equivalent plot of x and y. For boundary condition, the value of *Vp* is getting more under FBC as compare to the FFBC, this is due to the more confinement of the cube sample in FBC. Due to the cube confinement under the FBC, more energy was absorbed at time of impact resulting in higher strain. A summary of the chapter's main findings and their significance in the broader context of the study. The chapter serves as a crucial part of the overall research, providing empirical evidence and insights into how structural elements respond when subjected to controlled boundary conditions involving impacts and temperature variations and found that the concrete cube under the fixed bounder condition getting more damages in comparison to the free boundary condition. The more is the fixity of the concrete cube, the more is the maximum absorption capacity of the concrete cube.

Chapter 5: FINITE ELEMENT ANALYSIS OF CONCRETE CUBE SPECIMEN

5.1 Introduction

Chapter 5 serves as an introduction to the utilization of Finite Element Analysis (FEA) as a crucial tool in our study. FEA provides a comprehensive understanding of how structural elements react to different loads and boundary conditions. This chapter acts as a link between theoretical concepts and hands-on experimentation, as it delineates the computational framework employed for simulating and analysing the intricate behaviour of concrete under various conditions. By utilizing FEA, we acquire valuable insights into stress distribution, deformation characteristics, and the overall performance of the structure. This significantly enhances our grasp of the fundamental principles and practical implications of our research.

5.2 Specimen Property

5.2.1 Geometry and Material Properties

Table 5. 1 shows the material and thermal properties at ambient temperature that were used in the finite element analysis. Steel impactors with a specific gravity of 6839 kg/m^3 were used. Steel impactors were assumed to be liner elastic materials in the FEM analysis, with Young's modulus Es = 210 GPa and Poisson's ratio μ = 0.30.

Table 5. 1 Properties of concrete cube and Impactor

Property	**Concrete Cube**	**Impactor**
Density*(kg/m^3)*	2340	6839
Young’s mod., E (*GPa*)	30.91	210
Compressive strength*(MPa)*	29.7	-
Tensile strength *(MPa)*	2.88	-
Poisson’s ratio	0.2	0.30
Bulk modulus *(MPa)*	17172	166,670
Shear modulus *(MPa)*	12879	76,923

5.2.2 Geometry and Meshing

For the modelling of the concrete cube in this FEM analysis, hexahedral solid elements with used frictional type body interactions were used in the explicit dynamics module between the host structure (concrete cube) and the impactor (spherical ball). In this study, a 15 mm mesh size was used for both the concrete and the impactor, with the element mid nodes dropped at the time of meshing. Figure 5. 1 depicts the finite element model of concrete sample with and without meshing.

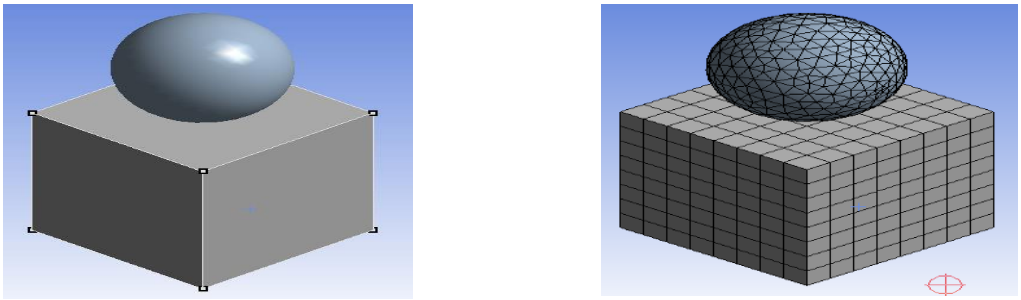

a) Finite element model of concrete sample without meshing

b) Finite element model of concrete sample with meshing

Figure 5. 1 Finite element model of concrete sample a) without meshing b) with meshing

5.2.3 Boundary Condition

In this study, concrete cubes were simulated with the two types of boundary conditions as the experiment, namely free-free boundary condition (FFBC) and fixed boundary condition (FBC)

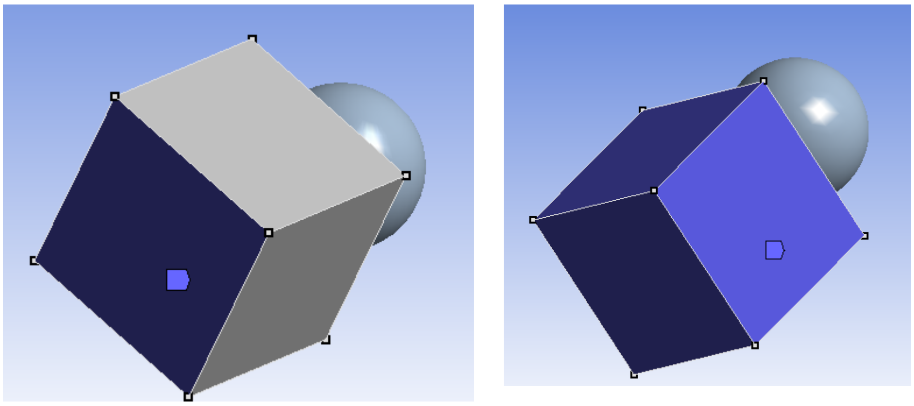

(a) **(b)**

Figure 5. 2 Boundary condition for the concrete sample a) Free-Free Boundary condition b) Fixed Boundary condition

Figure 5. 2 (a) and (b) show the free-free boundary condition and the fixed boundary condition applied to a concrete cube, respectively.

5.2.4 Loading Condition

As mentioned in the chapter 3, concrete cubes that have been experimentally tested were simulated for a single drop of impact under thermomechanical and explicit dynamics loading conditions. In thermomechanical analysis, the initial thermal loading is given in terms of an initial temperature of 22 ^{o}C to be applied to the entire body of a concrete cube. There were two steps of analysis performed in thermomechanical analysis, in the first step, the concrete cube was heated for two hours using convection method and then cooled down for one hour in which linear decrement of ambient temperature occurs as in the experiment. The concrete cube were heated at three different temperature condition of 50, 100 and 150 °C same as in the experiment.

After thermal exposure, concrete cubes were subjected to the spherical steel ball impact loading at the top surface of the concrete cube at center. Impact loading simulation were performed for the two different height of 3 and 3.5 m as same as the experiment. The impact load is generated by free fall dropping of the steel ball of weight 5.45 kg mass from the two different velocity of 7.67 m/s (3 m height) and 8.28 m/s (3.5 m height)

5.3 Result and Discussion

5.3.1 Results and Discussion for Free Boundary Conditions

The results of the thermomechanical and dynamic simulations are shown and discussed in this section. Figure 5. 3 (a) - (d) illustrates the distribution of elastic strain at a 3 m height of impact with temperatures ranging from ambient to 150 °C. Maximum strain values of 0.0074913, 0.0077198, 0.0081335, and 0.0085585 were observed at different variable temperatures of ambient, 50,100, and 150 °C, respectively, and they clearly illustrate that the strain value was temperature-dependent and they goes increasing as increase in temperature

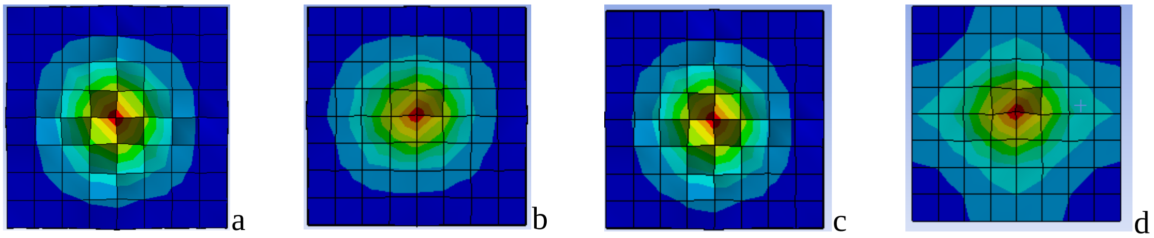

Figure 5. 3 Distribution of elastic strain for 3 m height of impact at varying temperature a) strain for 3 m height at ambient b) strain for 3 m height at 50 °C c) strain for 3m height at 100 °C d) strain for 3 m height at 150 °C

The distribution area of elastic strain became similar from ambient to 100 °C temperature. Figure 5. 3 (d) that shows the distribution of elastic strain at 150 °C temperature, it was observed that the distribution of elastic strain in the larger area for this temperature as compared to the lower temperature. This was because of due to the loss of the stiffiness of the concrete behaviour at higher temperature.

Figure 5. 4 (a)-d) depicts the elastic strain distribution at a 3.5 m impact height with temperatures ranging from ambient to 150 °C. Maximum elastic strain values of 0.0080842, 0.0083539, 0.0088, and 0.0092819 were observed at different variable temperatures of ambient, 50,100, and 150 °C, respectively, and all of these elastic strain values are higher than the previous elastic

strain values of 3 m height of impact, indicating that as impact force increases, the value of elastic strain transfer becomes more important. The elastic strain time history curve of the concrete cube was also obtained for 3 and 3.5 m heights of impact at temperatures ranging from ambient temperature to 150 °C. Figure 5. 5 (a)-(d) depicts the variation of elastic strain time history curve under the height of 3 m impact loading from ambient to 150 °C. From Figure 5. 5 clearly indicate that with the increase in temperature the elastic strain values goes increasing for the fixed height of impact loading (3 m).

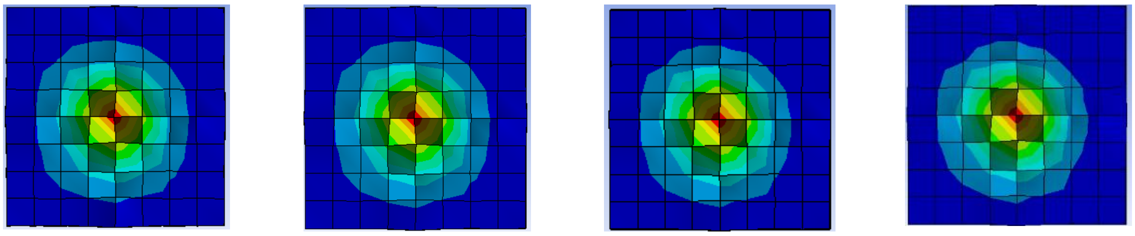

Figure 5. 4 Distribution of elastic strain for 3.5 m height of impact at varying temperature a) strain for 3. 5m height at ambient b) strain for 3.5 m height at 50 °C c) strain for 3.5m height at 100 °C d) strain for 3.5 m height at 150 °C

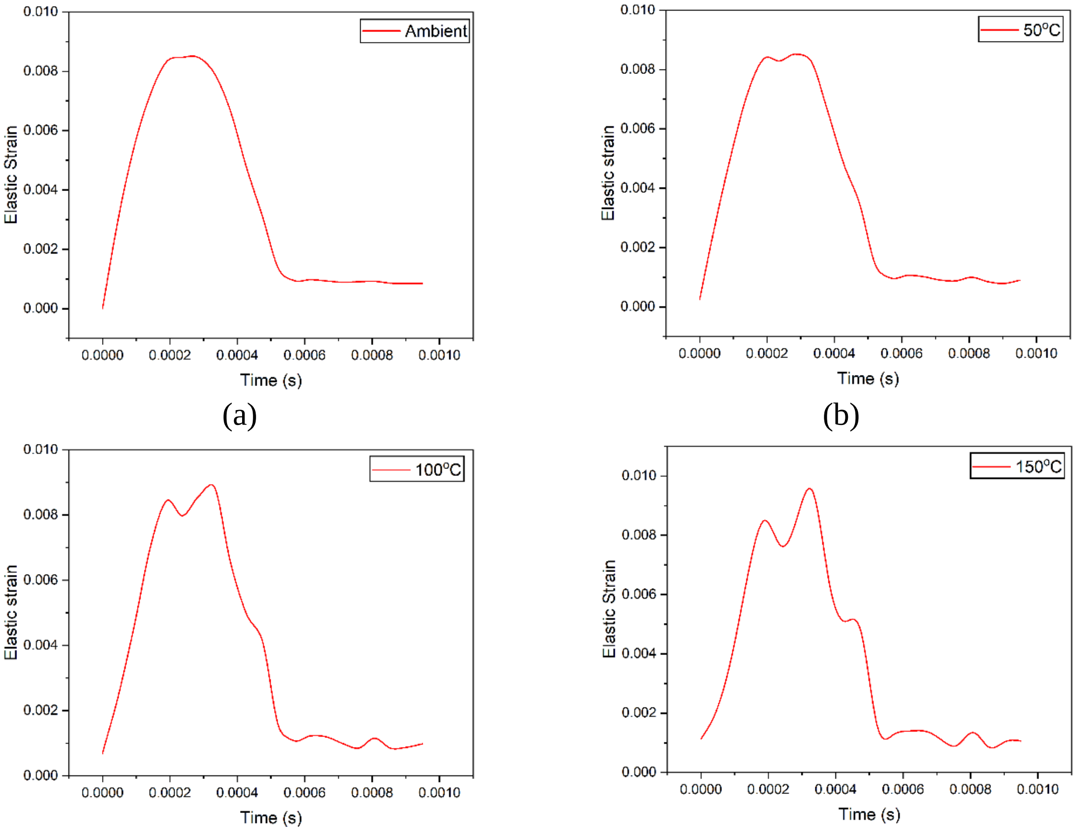

(a)

(b)

(c)

(d)

Figure 5. 5 (a)-(d) Variation of elastic strain time history curve under the height of 3 m impact loading from ambient to 150 °C

5.3.2 Results and Discussion for Fixed Boundary Conditions

The effect of impact loading can have a significant impact on boundary conditions (Anil et al. 2015). FEM analysis was performed for the FBC at 3 m height of impact at temperatures ranging from ambient to 150 °C for this purpose. Figure 5. 6 depicts the variation of elastic strain contours for FFBC and FBC for 3 m impact height at 150 °C. The development of elastic strain contours was in the larger area for FBC than in the FFBC. This is due to the concrete cube's higher absorption capacity under FBC.

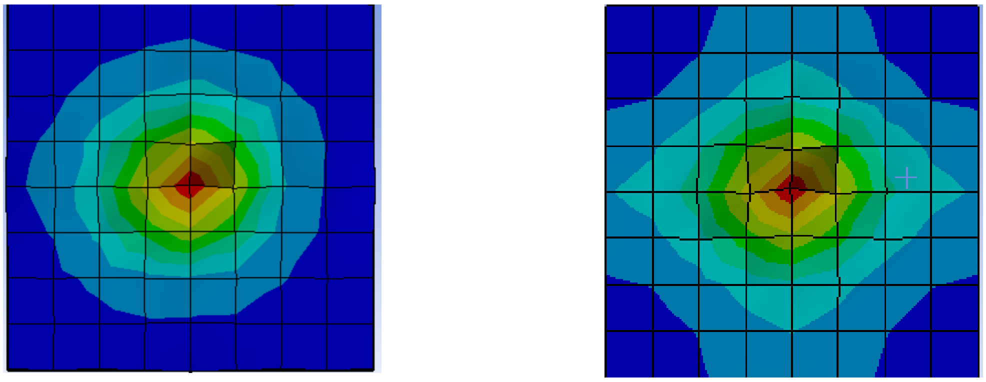

Figure 5. 6 Distribution of elastic strain contours for 3 m height of impact at 150 oC a) Free-Free boundery condition b) Fixed boundary condition

Figure 5. 7 (a)-(d) depicts the variation of elastic strain time history curve under the height of 3 m impact loading from ambient to 150 °C. From Figure 24 clearly indicate that, with the increase in temperature the displacement values goes increasing for the fixed height of impact loading (3 m) as same as for the FFBC. Furthermore for the better understanding, the elastic strain vs time graph were plotted for FFBC and FBC at different temperature condition as shown in Figure 5. 8 (a) - (d). From Figure 5. 8 (a) – (d), it is observed that elastic strain value found to be more for FBC as compared to FFBC for every temperature condition from ambient to 150 °C. This clearly shows that the FBC energy absorption capacity of the cube under impact loading was significantly higher than the FFBC. The maximum elastic strain values at 3 m height of impact at ambient temperature for FFBC and FBC were 0.0074913 and 0.0088604, respectively, representing an 18.27 % higher value.

5.4 Comparison in Free and Fixed Boundary Conditions

5.4.1 Comparison of Numerical Value for Elastic Strain under Free and Fixed Boundary Conditions at Varying Temperatures

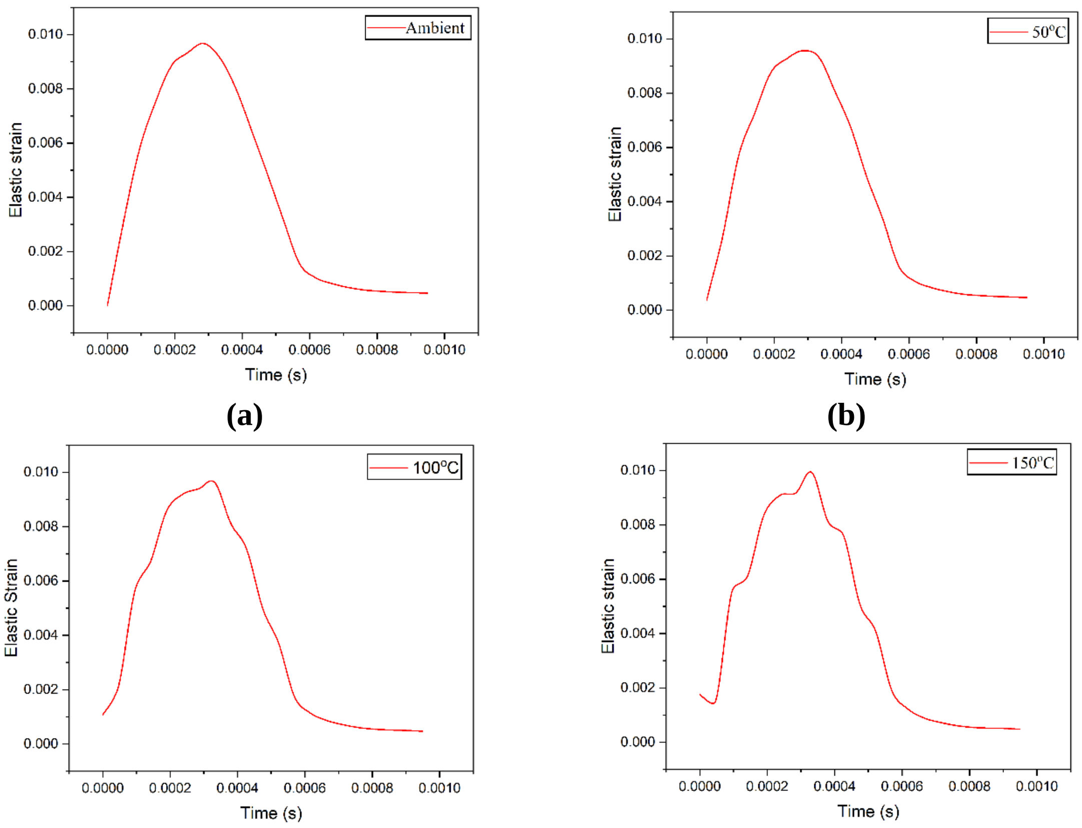

(a) (b)

(c) (d)

Figure 5. 7 Elastic strain time history curve for concrete cube at 3m impact under FBC a) ambient b) 50°C c) 100°C d) 150°C

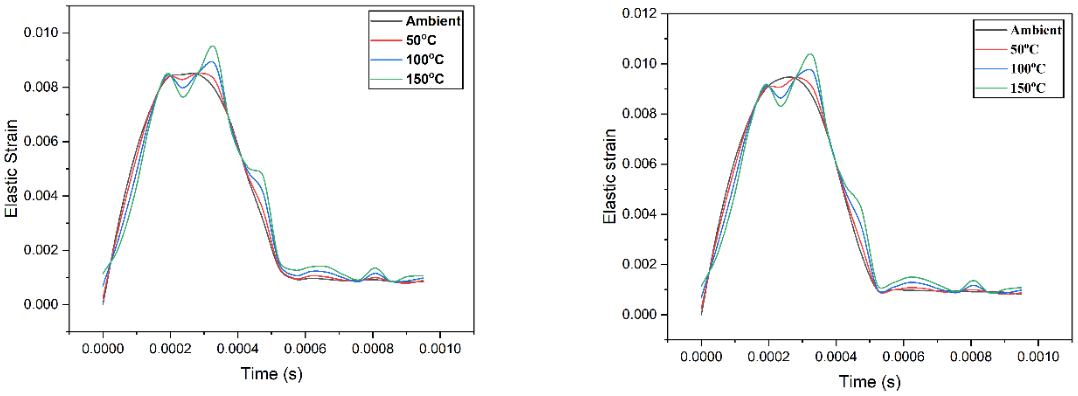

Figure 5. 8 Elastic strain time history curve for concrete cube under different impact height at varying temperature a) For 3 m impact height b) For 3.5 m impact height

From Figure 5. 9 (b) the elastic strain values increase from 0.0077198 to 0.0090553 at 50 °C, representing a 17.29 % increase for FFBC to FBC. For 100 °C the elastic strain values increases from 0.0081335 to 0.0094243, representing a 15.05 % increase and for 150 °C the elastic strain values goes increasing from 0.0085585 to 0.0097919 representing a 14.41 % increase. Table 5. 2 shows all the maximum value of elastic strain for FFBC and FBC for varying temperature.

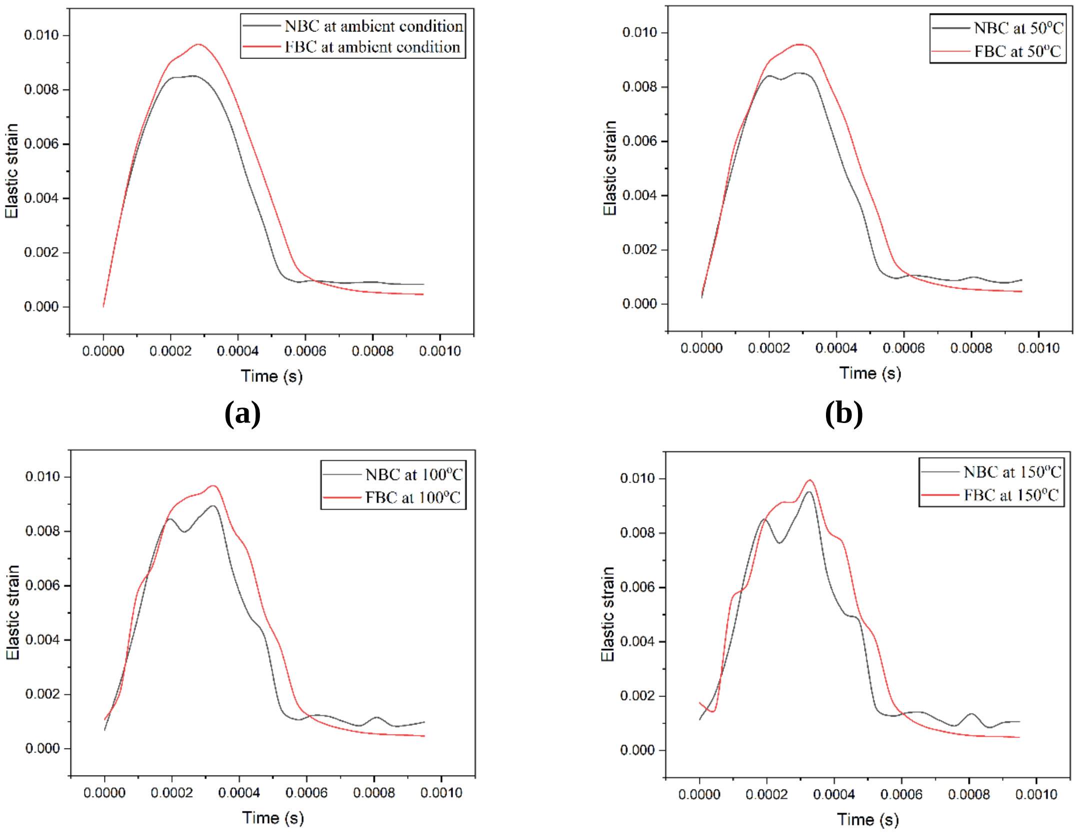

(a) **(b)**

(c) **(d)**

Figure 5. 9 Elastic strain variation with time for FFBC and FBC at varying temperature a) ambient b) 50 °C c) 100 °C d) 150 °C

Table 5. 2 Maximum elastic strain value at 3m height of impact for FFBC and FBC under varying temperature

Height of impact	Boundary condition	Temperature variation	Maximum Elastic strain
3m	Free-Free boundary condition	Ambient	0.0074913
		50 °C	0.0077198
		100 °C	0.0081335
		150 °C	0.0085585
3m	Fixed boundary condition	Ambient	0.0088604
		50 °C	0.0090553
		100 °C	0.0094243
		150 °C	0.0097919

5.4.2 Comparison of Experimental and Numerical Elastic Strain Values Under Free and Fixed Boundary Conditions

Elastic strain value of each concrete cube obtained from experiment and FEM analysis were compared. Typical example of the strain values for both experimental and numerical analysis under FFBC and FBC were shown in Table 5. 3 and Table 5. 4 respectively. The strain value calculated experimentally using voltage data from an oscilloscope gives the strain around the vicinity of the sensors. Furthermore this obtained experimental value of strain from the oscilloscope were compared with the FEM analysis. According to Table 5. 3 and Table 5. 4, the variation in the experimental and numerical values of elastic strain is less than 10 %. The difference in experimental and numerical values were due to inability of providing the exact fixity of the boundary condition in experimental condition as compared to the numerical analysis. Based on the comparison of numerical and experimental results, the FEM analysis was found to be highly consistent with the experimental results, indicating that the proposed modelling methodology is useful for studying the impact resistant behaviour of the concrete cube under varying temperatures. Figure 5. 10 depicts the variation of elastic strain vs temperature for the free-free boundary condition and fixed boundary condition, it is observed that the for the both the condition with the increase in temperature the elastic strain values goes increasing but for the fixed boundary condition more elastic strain value observed in comparison to the free-free boundary condition.

To validate the experimental results and investigate the efficacy of numerical simulation analysis for concrete cube under impact loading at various temperatures, experimental results of the concrete cube were compared with the finite element analysis.

5.5 Summary

This research described numerical simulations of a concrete cube subjected to the combined effects of temperature and impact loading. Furthermore the ANSYS explicit dynamics and transient thermal FEM software was used for the numerical simulation. In terms of elastic strain value, the numerical simulation results based on explicit dynamics and a transient thermal programme agree well with the measured experimental results. This indicates that the methodology proposed in this study was suitable for detecting damages in concrete structures subjected to impact loading at varying temperatures.

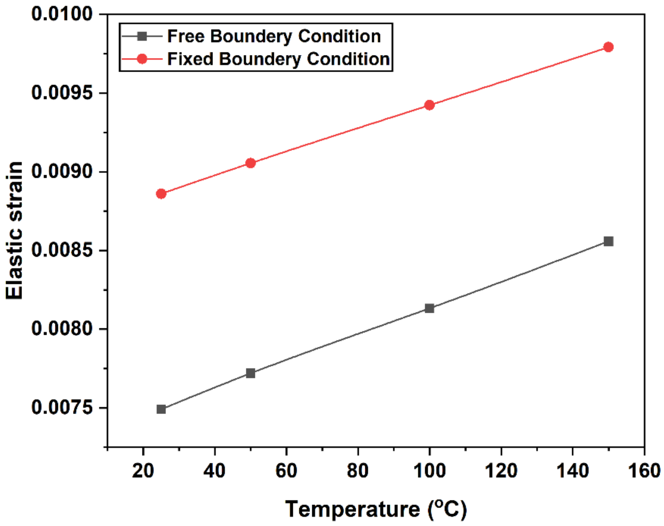

Figure 5. 10 Elastic strain vs temperature graph for FFBC and FBC

Table 5. 3 Experimental and numerical strain values around the vicinity of sensors for FFBC

S.No.	Cube representation no.	Temperature	Height of impact	Boundary condition	Experimental strain value around the vicinity of sensors x (10^{-6})	Numerical strain value around the vicinity of sensors x (10^{-6})
1	J1 (JKTPS)	Ambient	3m	Free-Free	0.473	0.49
2	J2 (JKTPS)	50	3m	Free-Free	6.87	7.05
3	J3 (JKTPS)	100	3m	Free-Free	18.9	21.20
4	J4 (JKTPS)	150	3m	Free-Free	3.27	35.50
5	J1a (JKTPS)	Ambient	3.5m	Free-Free	0.471	0.48
6	J2b (JKTPS)	50	3.5m	Free-Free	63.00	65.50
7	J4d (JKTPS)	150	3.5m	Free-Free	18.70	21.20

Table 5. 4 Experimental and numerical strain values around the vicinity of sensors for FBC

S.No.	Cube representation no.	Temperature	Height of impact	Boundary condition	Experimental strain value around the vicinity of sensors x (10^{-6})	Numerical strain value around the vicinity of sensors x (10^{-6})
1	7/4 (JKTPS)	Ambient	3m	Fixed	22.60	25.60
2	7/5 (JKTPS)	50	3m	Fixed	21.20	24.50
3	6/3 (JKTPS)	150	3m	Fixed	28.50	30.20

Chapter 6: CONCLUSIONS AND RECOMENDATIONS

6.1 Introduction

The aim of this research was to extend the application of the EMI technique for damage detection in concrete under impact loading at varying temperature using piezo sensors, especially utilizing the equivalent structural parameters.

The main innovation in this thesis is that it is the first to do such comprehensive research on damage detection using the EMI technique for the combination of impact and temperature load conditions on concrete and application of the equivalent structural parameters for the combined effect of impact and temperature. In this chapter, conclusions are drawn, and potential avenues for future research that would complement the content presented in this thesis are explored.

6.2 Conclusions and Contributions

The original research contributions of this thesis mainly consist of identification of best suitable sensors configuration for detection of damage in concrete cube and beam under the individual and combined action of impact and temperature by using structural parameter and numerical indices. The principal research conclusions and contributions can be succinctly summarized as follows:-

1. All three sensor configurations, namely jacketed piezo sensors (JKTPS), surface bonded piezo sensors (SBPS), and non-bonded piezo sensors (NBPS), perform well in predicting damage under combined effect of impact and temperature. Despite the fact that piezo sensors have a very high sensing behaviour against temperature, the JKTPS performed well with the fewest false alarms when compared to the SBPS and NBPS
2. The conductance signature followed a distinct pattern for ambient and higher temperature condition that clearly indicate the damage condition in the concrete cube.
3. On the basis of statistical tools such as root mean square deviation (RMSD) and mean absolute percentage deviation (MAPD) value, both are the reliable tools for calculating the incipient and progressive damage in concrete under the effect of impact loading at varying temperature.
4. Both the RMSD and MAPD indices followed a distinct pattern at varying temperatures of 150 ^{o}C for all sensor configurations clearly indicate the damage at varying temperatures
5. The extracted equivalent stiffness with increasing impact number clearly indicates damage propagation in concrete sample for different sensor configuration (10.42 % loss

for JKTPS) and also showed satisfactory agreement between the experimental and equivalent plot of x and y

6. Stiffness loss of 6.68% for JKTPS sensors, 5.742% for SBPS sensors, and 4.21% for NBPS sensors has been observed for the cube at 3 m impact height under ambient temperature.
7. Stiffness loss of 10.42 % for JKTPS sensors, 7.53 % for SBPS sensors, and 6.87 % for NBPS sensors has been observed for the cube at 3 m impact height under 150 ^{o}C temperature.
8. The stiffness loss increases with the rise in temperature from ambient to 150 °C, ranging from 6.87 % for NBPS sensors to 10.42 % for JKTPS sensors. This data illustrates that the stiffness loss escalates by approximately 3 to 4% with the increase in temperature.
9. The conductance signature followed a distinct pattern for ambient and higher temperature condition that clearly indicate the damage condition of the structural element such as beam.
10. The suseptance signature patterns clearly demonstrate that the JKTPS are intact, post failure of the beam that clearly shows that the JKTPS could be extremely beneficial not only for detecting initial damage but for damage induced till failure in the beam.
11. The extracted equivalent stiffness with increasing impact number followed a distinct decreasing pattern (stiffness loss up to 15%) that clearly indicates damage propagation in concrete beam and also showed satisfactory agreement between the experimental and equivalent plot of x and y.
12. For boundary condition, the value of peak voltage (Vp) is getting more under fixed boundary condition (FBC) as compare to the free- free boundary conditions (FFBC), this is due to the more confinement of the cube sample in FBC. This clearly illustrates that more energy was absorbed at the point of impact because to the cube confinement under the FBC, resulting in increased strain.
13. In terms of elastic strain value, the FEM results based on explicit dynamics and a transient thermal programme agree well with the measured experimental results. This indicates that the experimental and numerical methodology proposed in this study was suitable and showed good agreement between them for detecting damages in concrete structures subjected to impact loading at varying temperatures.

6.3 Limitations

Piezo sensors exhibit a high sensitivity to temperature conditions, which can potentially trigger false damage alarms in the structure. To mitigate this issue, it is advisable to consistently employ a temperature compensation technique to prevent such false alarms.

6.4 Future Recommendations

The following tasks are suggested to be pursued for the advancement of this research

1. The current study was conducted using M30 grade concrete; it can be extended to higher concrete grades.
2. The present work was carried out on the structural beam member, the same can be extended to slab member also.
3. The impedance data can be further used for correlating the damage quantification.
4. The present work was carried out for lower degree of temperature; the same can be extended to high degree of temperature.
5. The current study involved numerical modeling using the strain value data. It is suggested to further consider numerical modeling based on the raw signature data as a recommended approach.
6. To enhance the quantification of damage using the EMI technique, the research can be expanded by incorporating clip gauges into the sensors.

The author firmly believes in the substantial potential of advancing the EMI technique employing PZT sensors as a Non-Destructive Evaluation (NDE) method for assessing damage in concrete under the simultaneous influence of impact and temperature. This approach holds promise for delivering more effective assessments compared to conventional techniques.

PUBLICATIONS BASED ON THIS RESEARCH

INTERNATIONAL JOURNALS

1. **Indrajeet Singh**, Nirendra Dev, Shilpa Pal, (2022) “Impedance Based Damage Assessment of Concrete Under the Combined Effect of Impact and Temperature Using Different Piezo Configurations,” Sensors and Actuators: A Physical. 1-16.
2. **Indrajeet Singh**, Nirendra Dev, Shilpa Pal, (2023) “Damage identification in Concrete under impact loading at varying temperatures using voltage relations technique: An experimental and numerical study” Materials research express. pp. 1–26.

BOOK CHAPTER

1. **Indrajeet Singh**, Nirendra Dev, Shilpa Pal, Talakokula Visalakshi, (2022) “Finite Element Analysis of Impact Load on Reinforced Concrete” Lecture Notes in Civil Engineering, 28 October, pp. 265–274.

INTERNATIONAL CONFERENCE

1. Indrajeet Singh, Nirendra Dev, Shilpa Pal, Talakokula Visalakshi , (2020) “A review paper on different low cast variations of EMI technique”, presented in CRSIDE 2020, ASCE India section, March 2-4, 2020, Kolkata, India.
2. Indrajeet Singh, Nirendra Dev, Shilpa Pal, Talakokula Visalakshi, (2021) “Finite Element Analysis of Impact Load on Reinforced Concrete”, presented in 6th International Conference on “Emerging Technologies and Applications for Green Infrastructure CIGOS 2021, October 28-29, Vietnam.
3. Indrajeet Singh, Nirendra Dev, Shilpa Pal, (2020) “A review on monitoring of structures using low cost variants of EMI Techniques”, presented in International Conference on Advances in Sustainability of Materials and Environment (ICASME’23), May 25-26, 2023,Tamil Nadu , India.

REFERENCES

1. Abbas, S., F. Li, Z. Abbas, T. Ur Rehman Abbasi, X. Tu, and R. A. Pasha. 2021. “Experimental study of effect of temperature variations on the impedance signature of pzt sensors for fatigue crack detection.” *Sound Vib.,* 55 (1): 1–18. https://doi.org/10.32604/SV.2021.013754.
2. Aktan, A. E., and and C. J. T. F. N. Catbas, K. A. Grimmelsman. 2000. “ISSUES IN INFRASTRUCTURE HEALTH MONITORING FOR MANAGEMENT.” *J. Eng. Mech,* 126 (July): 711–724.
3. Al-ameri, R. A., S. R. Abid, G. Murali, S. H. Ali, and M. Özakça. 2021. “Residual repeated impact strength of concrete exposed to elevated temperatures.” *Crystals,* 11 (8): 1–21. https://doi.org/10.3390/cryst11080941.
4. Al, Y., Y. Temsah, O. Baalbaki, A. Jahami, and M. Darwiche. 2020. “Experimental investigation on the effect of impact loading on behavior of post- tensioned concrete slabs.” *J. Build. Eng.,* 31 (September 2019): 101207. Elsevier Ltd. https://doi.org/10.1016/j.jobe.2020.101207.
5. Anil, Ö., E. Kantar, and M. C. Yilmaz. 2015. “Low velocity impact behavior of RC slabs with different support types.” *Constr. Build. Mater.,* 93: 1078–1088. https://doi.org/10.1016/j.conbuildmat.2015.05.039.
6. Annamdas, V. G. M., and P. Rizzo. 2010. “Monitoring concrete by means of embedded sensors and electromechanical impedance technique.” *Sensors Smart Struct. Technol. Civil, Mech. Aerosp. Syst. 2010,* 7647: 76471Z. https://doi.org/10.1117/12.847687.
7. Annamdas, V. G. M., Y. Yang, and C. K. Soh. 2010. “Impedance based Concrete Monitoring using Embedded PZT Sensors.” *Int. J. Comput. Civ. Struct. Eng.,* 1 (3): 414–424. https://doi.org/10.6088/ijcser.00202010033.
8. Bansal, T., V. Talakokula, and K. Mathiyazhagan. 2022. “Equivalent structural parameters based non-destructive prediction of sustainable concrete strength using machine learning models via piezo sensor.” *Meas. J. Int. Meas. Confed.,* 187 (September 2021): 110202. Elsevier Ltd. https://doi.org/10.1016/j.measurement.2021.110202.
9. Baptista, F. G., D. E. Budoya, V. A. D. de Almeida, and J. A. C. Ulson. 2014. “An experimental study on the effect of temperature on piezoelectric sensors for impedance-based structural health monitoring.” *Sensors (Switzerland),* 14 (1): 1208–1227. https://doi.org/10.3390/s140101208.
10. Baral, S., P. Negi, S. Adhikari, and S. Bhalla. 2023. “Temperature Compensation for

Reusable Piezo Configuration for Condition Monitoring of Metallic Structures: EMI Approach." *Sensors*, 23 (3). https://doi.org/10.3390/s23031587.

11. Bentur, A., S. Mindess, and N. Banthia. 1986. "The behaviour of concrete under impact loading: Experimental procedures and method of analysis." *Mater. Struct.*, 19 (5): 371–378. https://doi.org/10.1007/BF02472127.
12. Berg, S., P. G. Bergan, and I. Holand. 1973. "Nonlinear Finite Element Analysis of Reinforced Concrete Plates." 2 (6): 403–417.
13. Bhalla, S. 2001. "Smart System Based Automated Health Monitoring of Structures." *Thesis*, (June 2000): 1–217.
14. Bhalla, S. 2004. "Structural Health Monitoring By Piezo-Impedance Transducers." 17 (65): 1–49. https://doi.org/10.1061/(ASCE)0893-1321(2004)17.
15. Bhalla, S., A. S. K. Naidu, and C. K. Soh. 2003. "Influence of structure-actuator interactions and temperature on piezoelectric mechatronic signatures for NDE." *Smart Mater. Struct. Syst.*, 5062: 263. https://doi.org/10.1117/12.514762.
16. Bhalla, S., P. A. Vittal, and M. Veljkovic. 2012. "Piezo-impedance transducers for residual fatigue life assessment of bolted steel joints." *Struct. Heal. Monit.*, 11 (6): 733–750. https://doi.org/10.1177/1475921712458708.
17. Bhuvaneshwari, P., and K. S. R. Mohan. 2020. "Strengthening of Fire-Damaged Reinforced Concrete Short Columns Using GFPPECC Composites." *Arab. J. Sci. Eng.*, 45 (10): 8619–8632. Springer Berlin Heidelberg. https://doi.org/10.1007/s13369-020-04795-x.
18. Bright Singh, S., and M. Murugan. 2021. "Performance of carbon fibre-reinforced pervious concrete (CFRPC) subjected to static, cyclic and impact loads." *Int. J. Pavement Eng.*, 0 (0): 1–16. Taylor & Francis. https://doi.org/10.1080/10298436.2021.1883017.
19. Dixit, A., and S. Bhalla. 2018. "Prognosis of fatigue and impact induced damage in concrete using embedded piezo-transducers." *Sensors Actuators, A Phys.*, 274: 116–131. Elsevier B.V. https://doi.org/10.1016/j.sna.2018.03.005.
20. Eibl, J. 1987. "Soft and hard impact." *Proc. First Int. Conf. Concr. Hazard Prot. Edinburgh*.
21. Esteban, J. 1996. "by wf face Ones tl." *PhD. Diss.* Institute and State University,Virginia Polyt, Blacksburg, VA.
22. Fan, S., S. Zhao, B. Qi, and Q. Kong. 2018. "Damage evaluation of concrete column under impact load using a piezoelectric-based EMI technique." *Sensors (Switzerland)*, 18

(5). https://doi.org/10.3390/s18051591.

23. Ganesan, P., and S. Venkata Sai Kumar. 2019. “FE modelling of low velocity impact on RC and prestressed RC slabs.” *Struct. Eng. Mech.*, 71 (5): 515–524. https://doi.org/10.12989/sem.2019.71.5.515.
24. Haq, M., S. Bhalla, and T. Naqvi. 2020. “Fatigue damage monitoring of reinforced concrete frames using wavelet transform energy of PZT-based admittance signals.” *Meas. J. Int. Meas. Confed.*, 164: 108033. Elsevier Ltd. https://doi.org/10.1016/j.measurement.2020.108033.
25. Hawileh, R. A., and M. Z. Naser. 2012. “Thermal-stress analysis of RC beams reinforced with GFRP bars.” *Compos. Part B Eng.*, 43 (5): 2135–2142. Elsevier Ltd. https://doi.org/10.1016/j.compositesb.2012.03.004.
26. Ikeda, T. 1990. *Fundamentals of Piezoelectricity*. Oxford University Press.
27. Jacky Mazars, A. M. 2013. *Dynamic Behavior of Concrete and Seismic Engineering*.
28. Jiao, Y., H. Liu, X. Wang, Y. Zhang, G. Luo, and Y. Gong. 2014. “Temperature effect on mechanical properties and damage identification of concrete structure.” *Adv. Mater. Sci. Eng.*, 2014. https://doi.org/10.1155/2014/191360.
29. Jin, L., H. Hao, R. Zhang, and X. Du. 2018a. “Determination of the effect of elevated temperatures on dynamic compressive properties of heterogeneous concrete: A meso-scale numerical study.” *Constr. Build. Mater.*, 188: 685–694. Elsevier Ltd. https://doi.org/10.1016/j.conbuildmat.2018.08.090.
30. Jin, L., R. Zhang, G. Dou, and X. Du. 2018b. “Fire resistance of steel fi ber reinforced concrete beams after low-velocity impact loading.” *Fire Saf. J.*, 98 (November 2017): 24–37. Elsevier Ltd. https://doi.org/10.1016/j.firesaf.2018.04.003.
31. Jin, L., R. Zhang, G. Dou, J. Xu, and X. Du. 2018c. “Experimental and numerical study of reinforced concrete beams with steel fibers subjected to impact loading.” *Int. J. Damage Mech.*, 27 (7): 1058–1083. https://doi.org/10.1177/1056789517721616.
32. Jothi Saravanan, T., K. Balamonica, C. Bharathi Priya, N. Gopalakrishnan, and S. G. N. Murthy. 2017. “Piezoelectric EMI–Based Monitoring of Early Strength Gain in Concrete and Damage Detection in Structural Components.” *J. Infrastruct. Syst.*, 23 (4): 04017029. https://doi.org/10.1061/(asce)is.1943-555x.0000386.
33. Jothi Saravanan, T., and S. Singh Chauhan. 2022a. “Study on pre-damage diagnosis and analysis of adhesively bonded smart PZT sensors using EMI technique.” *Meas. J. Int. Meas. Confed.*, 188 (June 2021): 110411. Elsevier Ltd.

https://doi.org/10.1016/j.measurement.2021.110411.

34. Jothi Saravanan, T., and S. Singh Chauhan. 2022b. “Study on pre-damage diagnosis and analysis of adhesively bonded smart PZT sensors using EMI technique.” *Meas. J. Int. Meas. Confed.*, 188 (November 2021): 110411. Elsevier Ltd. https://doi.org/10.1016/j.measurement.2021.110411.
35. Kennedy, R. P. 1976. “A review of procedures for the analysis and design of concrete structures to resist missile impact effects.” *Nucl. Eng. Des.*, 37 (2): 183–203. https://doi.org/10.1016/0029-5493(76)90015-7.
36. Kessler, S. S., S. M. Spearing, M. J. Atalla, C. E. S. Cesnik, and C. Soutis. 2002. “Damage detection in composite materials using frequency response methods.” *Compos. Part BEngineering*, 33 (1): 87–95. https://doi.org/10.1016/S1359-8368(01)00050-6.
37. Keysight (Agilent) Technologies. 2014. “E4980A Precision LCR Meter 20 Hz to 2 MHz.” 1–38. https://doi.org/https://www.keysight.com/in/en/assets/7018-01355/data-sheets/5989-4435.pdf.
38. Khan, M. S., J. Prasad, and H. Abbas. 2013. “Effect of High Temperature on High-Volume Fly Ash Concrete.” *Arab. J. Sci. Eng.*, 38 (6): 1369–1378. https://doi.org/10.1007/s13369-013-0606-1.
39. Kim, H., X. Liu, E. Ahn, M. Shin, S. W. Shin, and S. H. Sim. 2019. “Performance assessment method for crack repair in concrete using PZT-based electromechanical impedance technique.” *NDT E Int.*, 104 (November 2018): 90–97. Elsevier Ltd. https://doi.org/10.1016/j.ndteint.2019.04.004.
40. Kodur, V. K. R. 2018. “Innovative strategies for enhancing fire performance of high-strength concrete structures.” *Adv. Struct. Eng.*, 21 (11): 1723–1732. https://doi.org/10.1177/1369433218754335.
41. Kong, Q., S. Hou, Q. Ji, Y. L. Mo, and G. Song. 2013. “Very early age concrete hydration characterization monitoring using piezoceramic based smart aggregates.” *Smart Mater. Struct.*, 22 (8). https://doi.org/10.1088/0964-1726/22/8/085025.
42. Krishnanunni, A. V, N. Kaur, S. Bhalla, and N. Singh. 2023. “Efficacy of singly curved thin piezo transducers for structural health monitoring and energy harvesting for RC structures Efficacy of singly curved thin piezo transducers for structural health monitoring and energy harvesting for RC structures.” *Energy Reports*, 9 (February): 2506–2524. Elsevier Ltd. https://doi.org/10.1016/j.egyr.2023.01.084.
43. Kumar, A., V. S. Chauhan, R. Kumar, and K. Prasad. 2018. “Electromagnetic radiation

detection in 0-3 cement-PZT composite under impact loading." *Integr. Ferroelectr.*, 192 (1): 67–79. Taylor & Francis. https://doi.org/10.1080/10584587.2018.1521671.

44. Lan, C., S. Zhuang, S. Han, J. Wang, and W. Li. 2023. "Monitoring of soil water content using spherical smart aggregates based on electromechanical impedance (EMI) technique." *Smart Mater. Struct.*, 32 (7). https://doi.org/10.1088/1361-665X/acd506.
45. Liu, P., W. Wang, Y. Chen, X. Feng, and L. Miao. 2017. "Concrete damage diagnosis using electromechanical impedance technique." *Constr. Build. Mater.*, 136: 450–455. Elsevier Ltd. https://doi.org/10.1016/j.conbuildmat.2016.12.173.
46. Liu, Y., Z. Li, B. Jin, and J. Huo. 2018. "Experimental investigation on dynamic behavior of concrete after exposure to elevated temperatures." *Eur. J. Environ. Civ. Eng.*, 0 (0): 1–17. Taylor & Francis. https://doi.org/10.1080/19648189.2018.1500310.
47. Loganaganandan, M., G. Murali, and M. Parasuraman. 2020. "Experimental Study on GFRP Strips Strengthened New Two Stage Concrete Slabs under Falling Mass Collisions." https://doi.org/10.1007/s12205-020-0331-8.
48. Maurya, K. K., A. Rawat, and R. Shanker. 2023. "Developments in the Built Environment Performance evaluation concept for crack healing in bacterial concrete structure using electro mechanical impedance technique with PZT patch." *Dev. Built Environ.*, 15 (July): 100196. Elsevier Ltd. https://doi.org/10.1016/j.dibe.2023.100196.
49. Mina, A. L., M. F. Petrou, and K. G. Trezos. 2021. "Resistance of an optimized ultra-high performance fiber reinforced concrete to projectile impact." *Buildings*, 11 (2): 1–18. https://doi.org/10.3390/buildings11020063.
50. Na, S., and H. K. Lee. 2013. "Steel wire electromechanical impedance method using a piezoelectric material for composite structures with complex surfaces." 98: 79–84. https://doi.org/10.1016/j.compstruct.2012.10.046.
51. Na, S., R. Tawie, and H. Lee. 2012. "Electromechanical impedance method of fiber-reinforced plastic adhesive joints in corrosive environment using a reusable piezoelectric device." *J. ofIntelligent Mater. Syst. Struct.*, 23 (7): 737–747. https://doi.org/10.1177/1045389X12440754.
52. Nam, J.-W., and A. Hak-Chul Shin. 2012. "Damage Assessment of Concrete in Thermal and Dynamic Loadings." *J. Civ. Eng. Res.*, 2 (6): 49–56. https://doi.org/10.5923/j.jce.20120206.01.
53. Narayanan, A., A. Kocherla, and K. V. L. Subramaniam. 2018. "Understanding the coupled electromechanical response of a PZT patch attached to concrete: Influence of

substrate size." *Meas. J. Int. Meas. Confed.*, 124 (March): 505–514. https://doi.org/10.1016/j.measurement.2018.04.055.

54. Naskar, S., and S. Bhalla. 2016. "Metal-wire-based twin one-dimensional orthogonal array configuration of PZT patches for damage assessment of two-dimensional structures." *J. Intell. Mater. Syst. Struct.*, 27 (11): 1440–1460. https://doi.org/10.1177/1045389X15592480.
55. Negi, P., T. Chakraborty, N. Kaur, and S. Bhalla. 2018. "Investigations on effectiveness of embedded PZT patches at varying orientations for monitoring concrete hydration using EMI technique." *Constr. Build. Mater.*, 169: 489–498. Elsevier Ltd. https://doi.org/10.1016/j.conbuildmat.2018.03.006.
56. Negi, P., R. Chhabra, N. Kaur, and S. Bhalla. 2019. "Health monitoring of reinforced concrete structures under impact using multiple piezo-based configurations." *Constr. Build. Mater.*, 222: 371–389. Elsevier Ltd. https://doi.org/10.1016/j.conbuildmat.2019.06.100.
57. Ožbolt, J., L. Lacković, and D. Ruta. 2020. "Impact analysis of thermally pre-damaged reinforced concrete frames." *Materials (Basel).*, 13 (23): 1–23. https://doi.org/10.3390/ma13235349.
58. Ožbolt, J., D. Ruta, and B. İrhan. 2019. "Impact analysis of thermally pre-damaged reinforced concrete slabs: Verification of the 3D FE model." *Int. J. Impact Eng.*, 133 (April). https://doi.org/10.1016/j.ijimpeng.2019.103343.
59. Park, G. Kabeya, K. Cudeny, H.H. Inman, D. J. et al. 1999. "Impedance-Based Structural Health Monitoring for temprature Varying Application." *JSME Int. J.*, 42 (2): 249–258.
60. Park, G., H. Sohn, C. R. Farrar, and D. J. Inman. 2003. "Overview of piezoelectric impedance-based health monitoring and path forward." *Shock Vib. Dig.*, 35 (6): 451–463. https://doi.org/10.1177/05831024030356001.
61. Peairs, D. M., G. Park, and D. J. Inman. 2004. "Improving accessibility of the impedance-based structural health monitoring method." *J. Intell. Mater. Syst. Struct.*, 15 (2): 129–140. https://doi.org/10.1177/1045389x04039914.
62. Pham, T., and H. Hao. 2016. "Effect of the Plastic Hinge and Boundary Conditions on the Impact Behavior of Effect of the Plastic Hinge and Boundary Conditions on the Impact Behavior of Reinforced Concrete Beams." *Int. J. Impact Eng.*, (December). https://doi.org/10.1016/j.ijimpeng.2016.12.005.
63. Providakis, C. P., E. V. Liarakos, and E. Kampianakis. 2013. "Nondestructive Wireless

Monitoring of Early-Age Concrete Strength Gain Using an Innovative Electromechanical Impedance Sensing System." *Smart Mater. Res.,* 2013: 1–10. https://doi.org/10.1155/2013/932568.

64. Rafi, M. M., A. Nadjai, and F. Ali. 2008. "Finite element modeling of carbon fiber-reinforced polymer reinforced concrete beams under elevated temperatures." *ACI Struct. J.,* 105 (6): 701–710. https://doi.org/10.14359/20098.
65. Rogers, C. A. 1988. "SMART MATERIALS, STRUCTURES and MATHEMATICAL ISSUES." *U. S. Army Res. Off. Work. SMART,* (September 15-16): 1–12.
66. S. Bhalla, S. Moharana, V. Talakokula, N. K. 2017. "Piezoelectric Materials Applications in SHM, Energy Harvesting & Biomechanics." *Athena Acad. Wiley, London,* 44 (May).
67. Saravanan, T. J., K. Balamonica, C. B. Priya, A. L. Reddy, and N. Gopalakrishnan. 2015. "Comparative performance of various smart aggregates during strength gain and damage states of concrete." *Smart Mater. Struct.,* 24 (8): 85016. IOP Publishing. https://doi.org/10.1088/0964-1726/24/8/085016.
68. Sepehry, N., M. Shamshirsaz, and F. Abdollahi. 2011. "Temperature variation effect compensation in impedance-based structural health monitoring using neural networks." *J. Intell. Mater. Syst. Struct.,* 22 (17): 1975–1982. https://doi.org/10.1177/1045389X11421814.
69. Shankar, R. 2010. "An Integrated Approach for Health Monitoring of Structures." Indian Institute of Technology, Delhi.
70. Sharma, S. K., A. K. Sivarathri, V. S. Chauhan, and M. Sinapius. 2018. "Effect of Low Temperature on Electromagnetic Radiation from Soft PZT SP-5A Under Impact Loading." *J. Electron. Mater.,* 47 (10): 5930–5938. https://doi.org/10.1007/s11664-018-6464-6.
71. Shin, S. W., and T. K. Oh. 2009. "Application of electro-mechanical impedance sensing technique for online monitoring of strength development in concrete using smart PZT patches." *Constr. Build. Mater.,* 23 (2): 1185–1188. Elsevier Ltd. https://doi.org/10.1016/j.conbuildmat.2008.02.017.
72. Shin, S. W., A. R. Qureshi, J. Y. Lee, and C. B. Yun. 2008. "Piezoelectric sensor based nondestructive active monitoring of strength gain in concrete." *Smart Mater. Struct.,* 17 (5). https://doi.org/10.1088/0964-1726/17/5/055002.
73. Soh, C. K., and S. Bhalla. 2005. "Calibration of piezo-impedance transducers for strength prediction and damage assessment of concrete." *Smart Mater. Struct.,* 14 (4): 671–684.

https://doi.org/10.1088/0964-1726/14/4/026.

74. Soleimani, S. M., N. Banthia, and S. Mindess. 2007. “Behavior of RC beams under impact loading: Some new findings.” *Proc. 6th Int. Conf. Fract. Mech. Concr. Concr. Struct.*, 2 (Figure 1): 867–874.
75. Song, H., H. Cai, H. Cheng, and Z. Yao. 2018. “Physical model testing and numerical simulation for temperature distribution of mass concrete freezing shaft lining in deep alluvium.” *AIP Adv.*, 8 (7). https://doi.org/10.1063/1.5043454.
76. Su, Y. F., G. Han, A. Amran, T. Nantung, and N. Lu. 2019. “Instantaneous monitoring the early age properties of cementitious materials using PZT-based electromechanical impedance (EMI) technique.” *Constr. Build. Mater.*, 225: 340–347. https://doi.org/10.1016/j.conbuildmat.2019.07.164.
77. Sun, F. P., Z. A. Chaudhry, C. A. Rogers, M. Majmundar, and L. Chen. 1995. “Automated Real-Time Structure Health Monitoring via Signature Pattern Recognition”, Proceedings of SPIE, 2443: 236-247.” *Proc. SPIE - Int. Soc. Opt. Eng.*, 2443: 236–247.
78. Tawie, R., and H. K. Lee. 2010. “Monitoring the strength development in concrete by EMI sensing technique.” *Constr. Build. Mater.*, 24 (9): 1746–1753. Elsevier Ltd. https://doi.org/10.1016/j.conbuildmat.2010.02.014.
79. Tawie, R., and H. K. Lee. 2011. “Characterization of cement-based materials using a reusable piezoelectric impedance-based sensor.” *Smart Mater. Struct.*, 20. https://doi.org/10.1088/0964-1726/20/8/085023.
80. Wang, D., and H. Zhu. 2011. “Monitoring of the strength gain of concrete using embedded PZT impedance transducer.” *Constr. Build. Mater.*, 25 (9): 3703–3708. Elsevier Ltd. https://doi.org/10.1016/j.conbuildmat.2011.04.020.
81. Wang, Y., G. Yuan, Z. Huang, J. Lyv, Z. Q. Li, and T. yan Wang. 2016. “Experimental study on the fire behaviour of reinforced concrete slabs under combined uni-axial in-plane and out-of-plane loads.” *Eng. Struct.*, 128: 316–332. Elsevier Ltd. https://doi.org/10.1016/j.engstruct.2016.09.054.
82. Xia, Y., H. Hao, G. Zanardo, and A. Deeks. 2006. “Long term vibration monitoring of an RC slab: Temperature and humidity effect.” *Eng. Struct.*, 28 (3): 441–452. https://doi.org/10.1016/j.engstruct.2005.09.001.
83. Xu, B., G. Song, and Y. L. Mo. 2017. “Embedded piezoelectric lead-zirconate-titanate-based dynamic internal normal stress sensor for concrete under impact.” *J. Intell. Mater. Syst. Struct.*, 28 (19): 2659–2674. https://doi.org/10.1177/1045389X17698238.

84. Xu, J., J. Dong, H. Li, C. Zhang, and S. C. Ho. 2019. “Looseness monitoring of bolted spherical joint connection using electro-mechanical impedance technique and BP neural networks.” *Sensors (Switzerland),* 19 (8). https://doi.org/10.3390/s19081906.
85. Yang, Y., B. S. Divsholi, and C. K. Soh. 2010. “A reusable PZT transducer for monitoring initial hydration and structural health of concrete.” *Sensors,* 10 (5): 5193–5208. https://doi.org/10.3390/s100505193.
86. Yoo, S. J., T. F. Yuan, S. H. Hong, and Y. S. Yoon. 2020. “Effect of strengthening methods on two-way slab under low-velocity impact loading.” *Materials (Basel).,* 13 (24): 1–16. https://doi.org/10.3390/ma13245603.
87. Zuo, C., X. Feng, and J. Zhou. 2013. “A three-dimensional model of the effective electromechanical impedance for an embedded PZT transducer.” *Math. Probl. Eng.,* 2013 (December). https://doi.org/10.1155/2013/218026.